Adsorption and Reaction Microcalorimetry on Nickel and Platinum Single Crystal Surfaces

Charles Wartnaby

Churchill College

University of Cambridge

This thesis is submitted in accordance with the requirements of the University of Cambridge for the degree of Doctor of Philosophy.

Department of Chemistry June 1995

Declaration

This dissertation is the result of my own work, none of which has been submitted for another degree at any university, and includes nothing which is the outcome of work done in collaboration. In Chapter 6, existing data which are the work of N. Al-Sarraf and J.T. Stuckless are included alongside my own results, as detailed in that chapter.

Publications

Calorimetric Measurement of Catalytic Surface Reaction Heat – CO Oxidation on Pt{110}, C.E. Wartnaby, A. Stuck, Y.Y. Yeo and D.A. King, J. Chem. Phys. (Letters to the Editor) **102** (1995) 1855.

Microcalorimetric Study of Ethylene on Pt{110}-(1 ∞ 2), A. Stuck, C.E. Wartnaby, Y.Y. Yeo and D.A. King, Phys. Rev. Lett. **74** (1995) 578.

Adsorption Heats and Sticking Probabilities for CO on Potassium-Predosed Ni{110}, C.E. Wartnaby, J.T. Stuckless and D.A. King, Surf. Review and Lett. **1** (1994) 689.

Pyroelectric Single-Crystal Adsorption Microcalorimetry at Low Temperatures – Oxygen on Ni{100}, St.-J.B. Dixon-Warren, M. Kovar, C.E. Wartnaby and D.A. King, Surf. Sci. **309A** (1994) 16.

Oxygen Chemisorption and Oxide Film Growth on Ni{100}, {110} and {111}: Sticking Probabilities and Microcalorimetric Adsorption Heats, C.E. Wartnaby, J.T. Stuckless, N. Al-Sarraf and D.A. King, to be published.

Calorimetric Heats of Adsorption for CO, NO and Oxygen on Pt{110}, C.E. Wartnaby, A. Stuck, Y.Y. Yeo and D.A. King, to be published.

Calorimetric Measurement of the Engergy Difference between Two Solid Surface Phases, Y.Y. Yeo, C.E. Wartnaby and D.A. King, Science (in press).

An Improved Single Crystal Adsorption Calorimeter, A. Stuck, C.E. Wartnaby, Y.Y. Yeo, J.T. Stuckless, N. Al-Sarraf and D.A. King, Surf. Sci. (submitted).

Calorimetric Heats of Adsorption for CO on Nickel Single-Crystal Surfaces, J.T. Stuckless, N. Al-Sarraf, C. Wartnaby and D.A. King, J. Chem. Phys. **99** (1993) 2202.

Adsorption Microcalorimetry and Sticking Probabilities on Metal Single-Crystal Surfaces, N. Al-Sarraf, J.T. Stuckless, C.E. Wartnaby and D.A. King, Surf. Sci. **283** (1993) 427.

Adsorption and Reaction Microcalorimetry on Nickel and Platinum Single Crystal Surfaces

Abstract

The unique Cambridge single crystal adsorption microcalorimeter has been applied to a range of systems of catalytic interest to extract fundamental thermodynamic data. Coverage-dependent adsorption heats and sticking probabilities have been obtained with CO, NO, oxygen and ethylene adsorbates and Pt{110}, Ni{100}, Ni{110} and K/Ni{110} substrates.

The initial adsorption heats for CO, NO, and O_2 on Pt{110} are 183, 160 and 335 kJ mol^{-1} respectively. Catalytic heat of *reaction* data for CO + O_2 on Pt{110}, the first obtained on a single crystal surface, suggest that "hot" adatoms are involved in producing thermally excited CO_2 product molecules.

The first measurement of the heat of adsorption of a hydrocarbon on a single crystal surface has been made for ethylene on Pt{110}. The initial value of 200 kJ mol^{-1}, together with coverage dependent values, yield an average Pt–C binding energy of 231 kJ mol^{-1}.

A detailed comparison of new data for oxygen adsorption on Ni{100} and Ni{110} with existing data for Ni{111} is presented, with initial adsorption heats of 550, 475 and 440 kJ (mol O_2)$^{-1}$ respectively, while the corresponding sticking data suggest that the oxide film created is four atomic layers thick in each case.

Novel temperature-dependent data have been successfully collected using a pyroelectric detector for oxygen on Ni{100} at 100, 300 and 410 K with a Monte Carlo simulation of the highest-temperature data yielding a strong second-nearest neighbour interaction energy of +30 ± 5 kJ mol^{-1}.

The adsorption of CO on K-predosed Ni{110} was found to differ markedly from previous data collected on Ni{100} for potassium coverages up to 0.35 ML, with the adsorption heat promoted by only ~ 30 kJ mol^{-1} compared to ~ 180 kJ mol^{-1} for the {100} surface, a difference ascribed to the missing row reconstruction of Ni{110}.

Acknowledgements

Firstly I must thank my supervisor Prof. Dave King, who provided the initial idea for the machine and who talked me into taking on the project, and gave me continual encouragement to try out new ideas.

I would like to thank Todd Stuckless and Nadia Al-Sarraf for introducing me to the calorimeter and helping me through my first two years in the group, Todd in particular for first automating much of the procedure. Subsequently the pyroelectric calorimetry was made possible only through the efforts of St.John Dixon-Warren and Milan Kovar, whom I would also like to thank for his great hospitality in Prague, while Alexander Stuck made a grand job of building various electronic devices to enhance the machine. I was also glad to meet Jacques Chevallier, who manufactured our ultrathin crystals, and Chris Borroni-Bird, who first built the calorimeter, during the course of my PhD.

Huge support from the mechanical and electronic workshops, by Ron, Don, Mick and Stuart, and Joss, Wayne, Ian, John, Pat and David, both kept the machine running and sprouting wonderful new bits and pieces during my time.

I owe much to all the members of the group who lent help and advice and from whom I borrowed apparatus, notably from the SIRCL lab (Wendy Brown and Rakesh Sharma), the beams lab (Andrew Hopkinson, Jo Bradley, Alex Pasteur and Tejmel Ali), the LEED lab (Peijun Hu, Colin Barnes, Leigh Mapledoram, Marcel Bessent and Adrian Wander) and the RAIRS lab (Pete Gardner, Helen Dastoor and Wee-Sun Sim). I am also very pleased to have passed the helm onto Yee Yen Yeo, who has immediately produced excellent data and I hope will continue to do so.

Finally I thank Clare for bearing with me in my efforts, and for selflessly turning out to the pub with the rest of the group on innumerable occasions.

Contents

Chapter One

Introduction

1 Overview

The heat change associated with a chemical reaction is one of the fundamental thermodynamic quantities of interest in characterising and ultimately understanding the process. The reaction of gases with metal surfaces is no exception, and a great deal of work has been done extracting energetic data relating to adsorption and desorption.

Desorption energies are frequently estimated from thermal desorption spectroscopy, in which the desorption rate is monitored as a function of temperature and remaining coverage, and the desorption activation energy is then extracted assuming some kinetic rate law. More rigorously, adsorption enthalpies can be extracted from isosteric measurments in which the temperature and pressure required to maintain a particular equilibrium coverage are plotted and then a Clausius-Clapeyron type analysis is applied. In both cases, however, the heat parameter can be extracted only in conditions where the gas is desorbing significantly. This precludes the measurement of the adsorption heat for any gas adsorbing irreversibly, for example where the adsorbate decomposes or dissolves into the bulk before desorbing, and also implies that the heat can be measured for desorbing species only for the phase that they occupy at the desorption temperature, while energetic data for lower-temperature phases remain unavailable.

By measuring heat changes calorimetrically, however, there are no such limitations in the choice of system; irreversible adsorption energies can be measured as easily as reversible ones. However, the heat liberated by the adsorption of a small fraction of a monolayer of gas produces only a tiny temperature change in the crystals of usual thickness, and a highly specialised set of apparatus is required to quantitatively measure that small amount of heat. The calorimeter used here, and described in

detail in the following chapter, is the first and currently only instrument capable of measuring accurate adsorption heats on single crystal surfaces, and has already proved its worth in measuring adsorption heats for oxygen and CO on nickel[1-7].

In this thesis the following results are presented: further measurements on nickel, including novel temperature-dependent data for the prototypical chemisorption system, oxygen on Ni{100}; the first heat measurements of a surface *reaction*, the catalytic oxidation of CO on Pt, a system of great industrial importance; and the first adsorption heat data for hydrocarbon adsorption on a single crystal, here Pt{110}. For further discussion of the motivation behind each study, refer to the chapter in question.

2 The Calorimetric Adsorption Heat

A detailed comparison of the heat measured using our microcalorimeter with that obtained from isosteric or desorption measurements has been published previously[3], but a brief summary is given here for reference.

The ideal *differential adsorption heat*, q_d, is the (conventionally positive) change in internal energy between the adsorbed and gaseous states, equivalent to measuring the heat evolved by adsorption following a path in which no work is done. In general however, some work is done in compressing the gas, giving rise to a second term q_c, the heat of compression:

$$q_c = -p\frac{dV_g}{dn_a}$$

and the heat measured in a calorimeter is the sum of the two terms, $q_d + q_c$. The compression term is of the order of RT and depends on the system constraints such as whether the adsorption takes place under adiabatic or isothermal conditions. In our adsorption calorimeter, the volume of the adsorbate is negligible compared with that of the gas phase initial state and $q_c \spadesuit RT$. The heat measured in this experiment therefore, $q_{\mu cal}$, is given by

$$q_{\mu cal} = q_d + RT.$$

The *isosteric* adsorption heat q_{st} is obtained from coverage measurements at constant temperature and pressure, where again q_c ♠ RT, and so such measurements are directly comparable with our adsorption heat $q_{\mu cal}$. The value of q_{st} for some coverage is obtained from the slope of ln p versus $1/T$, which is linear if the adsorption heat is independent of temperature:

$$q_{st} = -R \left(\frac{\delta(\ln p)}{\delta(1/T)} \right)_\theta$$

an expression obtained in the same way as that for the heat of vaporisation of a liquid or solid in equilibrium with the gas phase, following a Clausius-Clapeyron analysis.

Thermal desorption experiments, however, do yield a slightly different energy parameter. Here an Arrhenius expression describes the desorption rate r_d for xth order kinetics:

$$r_d = \nu\theta^x \exp(-E_d / RT)$$

where in general both the frequency factor ν and desorption activation energy E_d are functions of coverage θ. To relate this activation energy E_d to q_{st}, we consider the situation at equilibrium where the adsorption rate from the gas at pressure p with a sticking probability σ exactly balances the desorption rate r_d:

$$\nu\theta^x \exp(-E_d / RT) = \frac{p\,\sigma}{(2\pi mkT)^{1/2}}$$

This equation relates p and T, so from it we can extract

$$\left(\frac{\delta(\ln p)}{\delta(1/T)} \right)_\theta + q_{st} = E_d - T\frac{\delta E_d}{\delta T} + \frac{RT}{2} - R\,\frac{\delta \ln(\nu/\sigma)}{\delta(1/T)}$$

where the partial derivatives on the RHS are taken at constant coverage also. If the desorption activation energy, frequency factor and sticking probability are *all* independent of temperature, then we have

$$E_d = q_{st} - \frac{1}{2} RT.$$

In practical terms, at 300 K the value of RT is only 2.5 kJ mol^{-1}, two orders of magnitude smaller than the typical adsorption heats we measure and smaller than our error bars. We can therefore neglect the small differences between the slightly differing values of $q_{\mu cal}$, q_{st}, E_d (and $-\Delta H$) in comparing our results to other data, and loosely equate all with the differential or partial molar energy difference between the gas and adsorbed phases.

3 Previous Adsorption Calorimetry Measurements

Adsorption calorimetry has been done before using polycrystalline samples in the form of metal wires and films, and there has been one previous attempt with a single-crystal sample[8]. In the latter case a pair of thermistors were embedded in a Pt{111} crystal, one to measure temperature changes and the other to provide a known heat input for calibration. However, a near-saturation dose of 0.4 ML of CO was required to obtain a reasonable signal, which the authors calculated as corresponding to an adsorption heat of 40 ± 10 kcal mol^{-1}. This value is though in superb agreement with the integral heat at 0.4 ML calculated from our high coverage-resolution measurements[9] for the same system, of 39 kcal mol^{-1}.

A thorough calorimetric study of oxygen adsorption on a range of polycrystalline transition metal films was reported by Brennan *et al*[10], and is referenced elsewhere in this thesis. In that study a Beeck type calorimeter was used; it consisted of a thin cylindrical glass tube with a platinum resistance thermometer wrapped uniformly around the outside, and a filament running axially from which the metal under study could be evaporated onto the internal surface. The calorimeter operated in near-adiabatic mode, with the space outside the tube evacuated during

measurements to minimise heat losses. Approximate coverages were obtained by measuring inert gas isotherms to obtain the microscopic sample area. Initial heats of adsorption of 69 and 117 kcal mol^{-1} (289 and 490 kJ mol^{-1}) were extracted for platinum and nickel respectively; the figure for nickel falls amongst our results for the three low-index planes (see Chapter 6), while that for platinum is perhaps unsurprisingly lower than the value of 335 kJ mol^{-1} found here for the open Pt{110} (see Chapter 3), although a heat of ~ 350 kJ mol^{-1} has also been found[9][11] for the Pt{111} and Pt{100}-(1 ∞ 1) surfaces in our laboratory.

Both of these previous studies provide reasonably consistent results with our data, but the single-crystal study suffers from poor coverage resolution, while the polycrystalline results are necessarily for a surface of ill-defined structure. The present instrument offers far superior sensitivity, and hence coverage resolution, without sacrificing the well-defined single crystal surface, with the bonus of simultaneously measured sticking probabilitie and an absolutely calibrated coverage scale.

References

[1]C.E. Borroni-Bird and D.A. King, Rev. Sci. Instrum. **62** (1991) 2177.

[2]C.E. Borroni-Bird, N. Al-Sarraf, S. Andersson and D.A. King, Chem. Phys. Lett. **183** (1991) 516.

[3]J.T. Stuckless, N. Al-Sarraf, C. Wartnaby and D.A. King, J. Chem. Phys. **99** (1993), 2202.

[4]N. Al-Sarraf, J.T. Stuckless, C.E. Wartnaby and D.A. King, **283** (1993) 427.

[5]N. Al-Sarraf, J.T. Stuckless and D.A. King, Nature **360** (1992) 243.

[6]C.E. Borroni-Bird, PhD Thesis, University of Cambridge 1991.

[7]N. Al-Sarraf, PhD Thesis, University of Cambridge 1993.

[8]D.A. Kyser and R.I. Masel, J. Vac. Sci. Technol. A **4** (1986) 1431.

[9]Y.Y. Yeo, A. Stuck and D.A. King, unpublished work.

[10]D. Brennan, D.O. Hayward and B.M.W. Trapnell, Proc. Roy. Soc. A **256** (1960) 81.

[11]Y.Y. Yeo , C.E. Wartnaby and D.A. King, Science (in press).

Chapter Two

Experimental

1 Introduction

The microcalorimetry technique has been described before in detail in the literature[1][2][3][4][5] but has undergone various improvements in the course of the experiments described in this thesis, which are described below.

The essence of the experiment is shown in Figure 1. A pulse of molecules are directed at the front face of the crystal using a molecular beam; in general, some proportion of those molecules will adsorb at the surface and so liberate some adsorption heat in the surface region. As the crystal is ultrathin (~ 2000 Å), heat conduction between the front and back faces is rapid and the heat capacity of the volume between the front and back faces is small, so that a significant bulk temperature rise occurs. However, the thinness of the crystal also renders heat conduction to the crystal support ring very inefficient, so the subsequent cooling of the crystal back to ambient temperature will occur largely by radiation. A thin coating of amorphous carbon on the back face of the crystal, with a large emissivity, ensures that most of the excess radiation will occur from the back face, and a broad spectral range of the infrared light emitted from that face is collected. In this way the temperature rise of the crystal due to the gas adsorption is monitored remotely.

That portion of the gas pulse that does not adsorb must instead reflect back into the gas phase, producing a partial pressure rise in the experimental chamber. This is measured using a mass spectrometer, and so the relative adsorbed amount or sticking probability can be inferred. With appropriate absolute calibrations of the measured heat and adsorbed amount, which are described below, the molar adsorption heat can be calculated. Furthermore as more gas pulses are directed at the crystal both the adsorption heat and sticking probability can be plotted as a function of accumulated coverage.

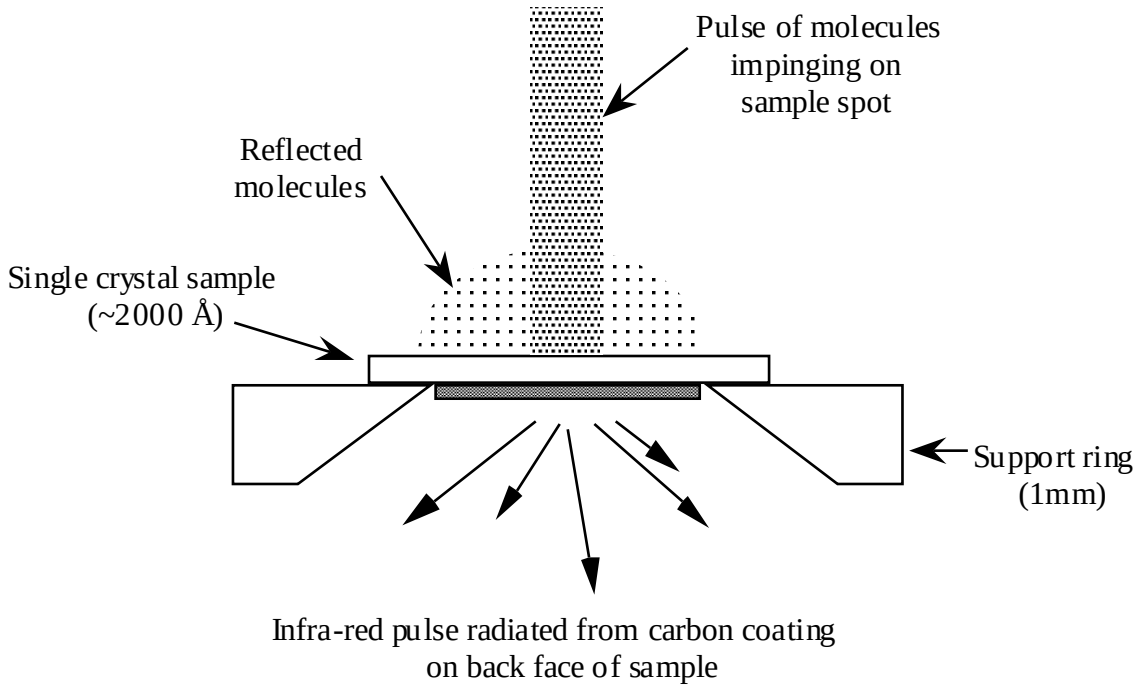

Figure 1. A schematic depicting the principles of the microcalorimetry experiment.

2 Ultrahigh Vacuum Chamber

The microcalorimeter UHV chamber depicted in Figure 2 consists of two sections: one for crystal cleaning and analysis, and one in which the calorimetry experiment itself is performed. The sample is mounted on a horizontal long-travel manipulator which is used to transport it between the two sections and align it appropriately for the various processes involved in crystal preparation.

The preparation chamber is equipped with an ion gun for Ar^+ sputtering, a focused lamp for heating, an electron gun and cylindrical mirror analyser (CMA) for Auger spectroscopy, and low energy electron diffraction (LEED) optics. The experimental chamber contains a slot to precisely align the sample with the molecular beam axis, behind which is fixed the stationary part of the gold parabola (see below). Between the crystal position and the final collimating hole of the molecular beam system the gold flag can be translated in and out under computer control using a solenoid, and the accumulation tube used for molecular beam calibration can be translated in manually when required. For those experiments involving potassium deposition,

the alkali metal getter source was mounted such that it too faced the crystal in the experimental position.

The whole chamber is pumped by an oil diffusion pump baffled from the chamber by a liquid nitrogen cooled cold trap. A water-cooled titanium sublimation pump provides further pumping capacity. The chamber is stainless steel throughout and reaches a base pressure of $5 \infty 10^{-11}$ mbar in the experimental section.

3 Ultrathin Single Crystals

3.1 Production and Mounting

The microcalorimetry experiment is made feasible only by the use of ultrathin single crystals, which have a very high surface area to heat capacity ratio and so undergo a measurable temperature rise when a small quantity of heat is absorbed by the metal surface due to the adsorption of some gas.

Each single crystal film of ~ 2000 Å thickness and ~ 1 cm^2 area was grown[6] epitaxially by evaporation onto the corresponding polished crystal plane of a radiation-hardened NaCl single crystal, previously annealed to ~ 800 K, at growth rates of 10-20 Å s^{-1} and at a substrate temperature of 600-700 K. The NaCl was subsequently dissolved away in water to leave the metal crystal, supported by surface tension, floating on the water. The support ring, made of the same metal as the crystal, was etched in a hot acid mixture to remove any surface oxide, rinsed clean in distilled water, and then used to lift the crystal off the water. Finally gentle pressure was applied to expel the water between crystal and ring and pull the thin film taut and flat, resulting in a permanent cold weld giving good mechanical support and electrical contact.

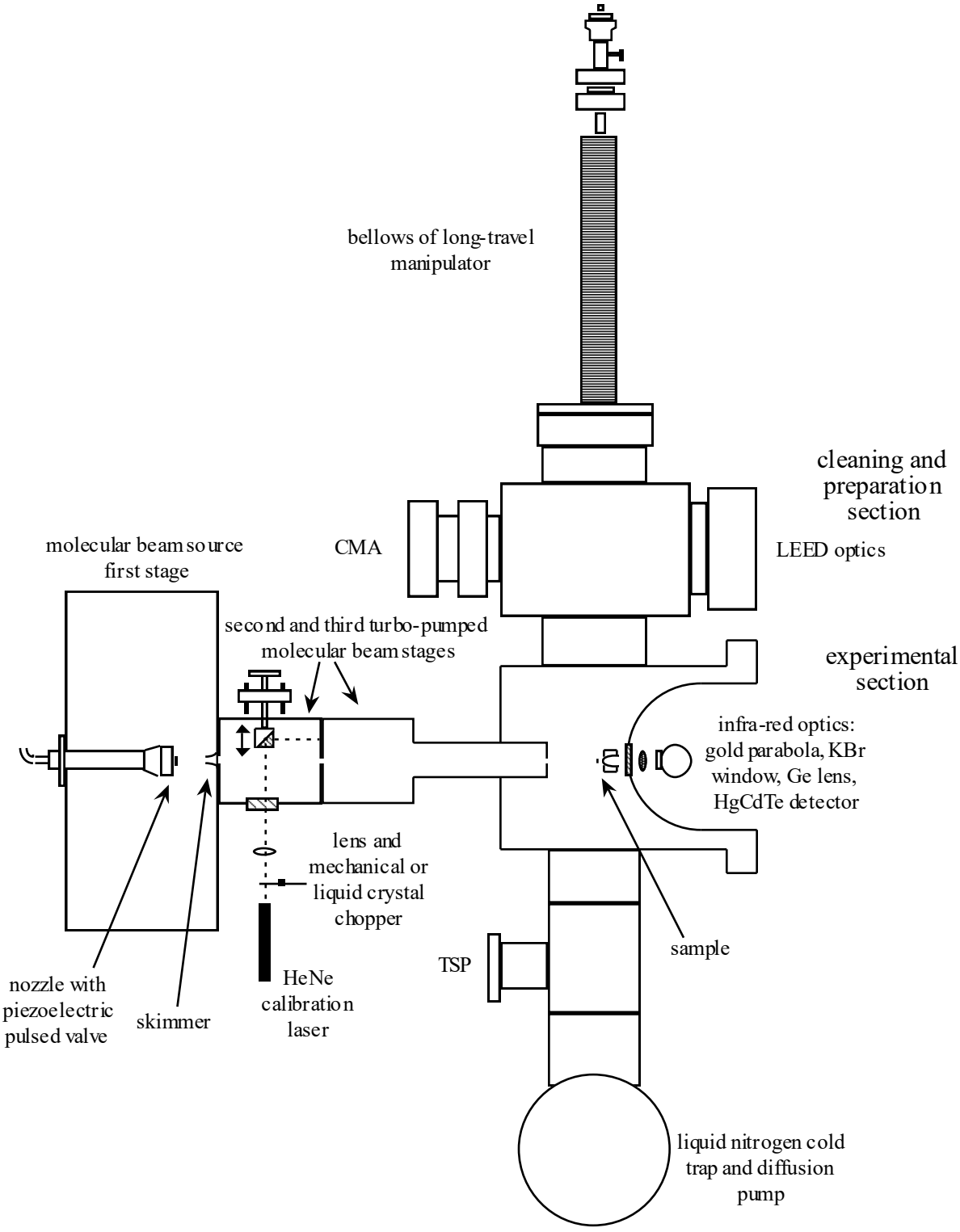

Figure 2. Plan view of the ultrahigh vacuum chamber showing layout of molecular beam system.

3.2 Cleaning Procedure

The Pt{110} and the Ni{100} and {110} crystals studied in this series of experiments were all cleaned using broadly the same procedure. The ultrathin crystals were supplied substantially free of bulk impurities, and so the extensive cycles of sputtering and annealing required to initially clean conventional metal crystals were not required. Instead only a brief cleaning cycle was performed immediately before each calorimetry experiment to prepare the surface of the crystal. Gentle (1 μA cm^{-2}) sputtering using a diffuse 500 eV Ar^+ ion beam removed oxygen and most carbon in a treatment of 10 min. On the nickel surfaces, some oxygen treatment prior to sputtering was required to remove all of the carbon contamination: a large exposure of oxygen was administered using the molecular beam and then the crystal was annealed to allow oxidation of carbon adatoms. After sputtering, the crystal was annealed by radiative heating using the lamp to restore surface order. Finally the crystal cleanliness was assessed by CMA Auger spectroscopy, and further cycles of sputtering and annealing were applied until no detectable contamination remained.

LEED was used to assess the quality of the resulting surface from time to time. In the case of Ni{100} and {110} surfaces, sharp (1 ∞ 1) patterns were obtained. Pt{110} spontaneously reconstructs to give a (1 ∞ 2) missing-row structure at room temperature, and annealing temperatures in excess of 1000 K are required[7] to obtain excellent order, while our annealing is limited to an estimated 600 K. Here our LEED patterns showed a (1 ∞ 2) with streaking indicating some contribution from other (1 ∞ n) periodicities, as shown in Chapter 5.

4 Infrared Heat Detection

4.1 Description of Optics

The infrared optics are designed to maximise the proportion of the blackbody light emitted by the crystal that is absorbed by the detector. The carbon deposit on the back face of the crystal should have a large emissivity (~ 0.95 typical for soot) compared with the front face (~ 0.05)[8], ensuring that most light is emitted by the

back face and reducing the cooling time constant to ~ 100 ms from ~ 1 s for an uncoated crystal, greatly increasing the detectability of the signal. The light emitted is directed onto the detector using three elements: a two-part gold parabola to give an approximately parallel beam through the second element, a KBr window separating vacuum from atmosphere, and finally a Ge lens to focus the beam down on to the detector.

4.2 Mercury Cadmium Telluride Detector and Electronics

The infrared light was collected using a liquid nitrogen cooled mercury cadmium telluride (MCT) photoconductive detector with a preamplifier configured to give a voltage signal proportional to the rate of change of the total intensity measured. The detector was sensitive to light between 2 and 15 μm in wavelength, encompassing some 56% of the power spectrum expected from a blackbody emitter at 300 K.

The weak voltage signal from the preamplifier was further amplified with a gain of 40 dB using a Brookdeal type 452 a/c amplifier operating with an acceptance window of 1 Hz to 1 kHz. The resulting signal of up to ± 3 V was then digitised and stored by the experimental computer.

5 Laser Calibration

5.1 Principle of Calorimeter Calibration

The thin film crystal sample became somewhat thinner following each cleaning cycle, giving a progressively decreasing heat capacity and hence increasing sensitivity. In order to quantify the heat signals obtained during adsorption experiments the calorimeter therefore had to be recalibrated each time. This was done by dosing a known quantity of heat into the crystal by firing a HeNe laser beam pulse at it, mimicking both the spatial and temporal distribution of the gas pulses, to produce reference heat signals.

In order to calculate the absolute amount of heat dosed into the crystal during each laser pulse, the following procedure was followed: the steady laser power was

measured outside the KBr window using an absolutely calibrated photodiode. The laser power incident on the crystal was then found by dividing that value by the transmission of the KBr window at the HeNe wavelength of 633 nm, which was measured from time to time. The absorbed power was then deduced knowing the reflectivity of the crystal at 633 nm, which was also measured. This value for the absorbed power was then multiplied by the pulse width to give the energy absorbed during each pulse. The measured infrared signal was found to be linear in laser power, although the power was chosen to give infrared signals of similar magnitude to those obtained at the start of a real experiment.

5.2 Description of Laser Optics

The laser calibration system was improved between the experiments on nickel and those on platinum. The basic optical system was largely unchanged, however. A 1 mW HeNe laser mounted normal to the molecular beam axis was passed through a biconvex lens to give a slight divergence, imitating the molecular beam. The diverging beam entered the second stage of the molecular beam through a glass window and was reflected down the molecular beam axis onto the crystal using a prism which was translated into place during calibrations. The laser beam was thus cropped by the same two collimating holes that the molecular beam was limited by spatially, to give the same spot profile on the crystal.

For the experiments on nickel, the laser was modulated by a mechanical rotating disc chopper to give one 50 ms pulse per 1 s rotation. The laser power was measured after sufficient signals (~ 10) had been obtained to achieve good statistics and assumed to have remained constant throughout the calibration. However, the chopper was inconveniently unstable, and for the experiments on Pt was replaced by a liquid crystal device which could be slaved to the same signal source as used to control the molecular beam pulses, ensuring that the same pulse width was achieved. Furthermore, in order to eliminate the effect of any possible drift in either the laser beam power or transmission of the liquid crystal shutter, the laser beam

was sampled before entering the UHV system using a beamsplitter and second photodiode mounted after the lens.

5.3 Electronics and Data Analysis

The infrared signal was collected and treated in exactly the same way as during adsorption experiments; the voltage output from the a/c amplifier was digitised at 500 Hz by an analogue-to-digital converter and stored on hard disk. In subsequent analysis a simple smoothing algorithm was applied to eliminate high-frequency noise and the peak-to-peak height of the signal measured. Following the introduction of the liquid crystal shutter and second (normalising) photodiode, the signal from the latter was acquired at 10 kHz simultaneously with the infrared signal, the higher frequency sampling ensuring that the pulse shape could be resolved. This intensity-time profile revealed that the liquid crystal shutter achieved a rise time of ~ 3 ms in opening and a fall time of < 1 ms in closing. The integral of this signal was calculated to correct for the small deviation from an ideal rectangular signal and each infrared signal was normalised to that integral to correct for any drift in laser pulse strength; in practice very little drift was actually observed, with a typical standard deviation between pulses of < 1%. After a set of infrared signals had been collected the sample was moved out of the laser beam path and the laser power was measured using the calibrated photodiode with the liquid crystal shutter open and then closed, while the signal from the normalising photodiode was acquired by the computer; the signal from the latter photodiode could thus be related to the absolute laser power used during the calibration.

6 Molecular Beam Dosing and Calibration

6.1 Advantages of Pulsed Molecular Beam Dosing

A pulsed molecular beam was used as the gas source to satisfy several criteria. Firstly, admitting the adsorbate in short pulses in time creates rapid changes of temperature which can be distinguished above slower temperature drifts using the

a/c coupled detector, which responds to the rate of change of signal intensity. In the mass spectrometer signals, using short pulses ensured that the background pressure level could be subtracted from the beam peak for each signal eliminating a potential source of drift, and the duty cycle of 50 ms on and 2 or 2.5 s off allowed the gold flag to be moved in and out of the beam path without interrupting dosing in an ill-defined manner. Spatially the molecular beam profile was very well defined and confined to the sample spot, ensuring a large (and accurately measured) exposure only onto the crystal.

6.2 Description of Molecular Beam System

The molecular beam system used in this apparatus consisted of three differentially pumped stages over a relatively long path length of ~ 1 m, giving a well-defined "top hat" profile at the expense of having a limited maximum flux. The pulse profile is crucial, however, as we assume that the exposure (and hence coverage) is constant across the sample spot and zero outside it. An inhomogeneous profile would lead to a blurring of resolution and uncertainty in magnitude of our calculated coverages; a simple geometrical calculation[4] suggested that the expected radius of the penumbra is 1.08 mm and that of the umbra 1.05 mm assuming perfect alignment, in excellent agreement with an optical determination of 1.025 mm average for the real beam. The source is a 0.3 mm diameter nozzle, to which gas at ~ 2 atm is admitted in 50 ms pulses using a piezoelectrically operated valve, mounted some 20 mm from the 0.76 mm entrance hole of a nickel skimmer leading to the second stage. The gas undergoes a supersonic expansion into the first stage, which has a volume of 40 l and which is pumped by an unbaffled Edwards 1000 l s^{-1} oil diffusion pump; this combination of a large volume and high pumping speed minimises the pressure rise induced in the first volume. The flux of the molecular beam is limited by background gas in the first stage scattering molecules initially on trajectories which would pass through the skimmer, and so minimising the pressure there maximises the beam flux.

The second and third stages are pumped by Leybold-Heraeus turbomolecular pumps of 350 and 150 l s^{-1} pumping speeds respectively. A 2 mm collimating hole separates the second stage from the third, with a tube of 2 mm internal diameter and 30 mm length separating the third stage from the experimental chamber. The tube replaced a previous simple orifice and was introduced to reduce the diffusion of out-of-beam gas from the molecular beam system to the UHV system.

6.3 Calibration of Beam Flux

To be able to calculate a molar adsorption heat it is clearly necessary to know absolutely the amount of gas adsorbed as well as the quantity of heat evolved. In the microcalorimetry experiment we must therefore measure both the number of molecules in each molecular beam pulse and the sticking probability. Knowing the sticking probability for each pulse and the sample area, we can then also calculate the accumulated coverage on the crystal.

The molecular beam flux is measured using an accumulation tube[9] consisting of a thin pipe, through which the molecular beam is directed without scattering, leading into an otherwise enclosed volume with a pressure gauge. The pipe has an internal diameter of 3 mm, so capturing the entire beam, and is 30 mm in length. The beam is pulsed into the volume until a steady-state situation is achieved whereupon the average molecular fluxes into and out of the tube are identical. The inward flux is the molecular beam strength we wish to measure, while the outward flux is given by the product of the pressure inside the tube and the conductance of the thin pipe, which can be calculated knowing its length and diameter, assuming random kinetic gas behaviour[10]:

$$C = \frac{a'\,\nu A}{4} \qquad (1)$$

with

$$\nu = \sqrt{\frac{8kT}{\pi m}} \qquad (2)$$

A is the cross-sectional area of the pipe, and the value of a' depends on the aspect ratio of the pipe; for a length : diameter ratio of 10, it takes a value of 0.1135. For CO at 300 K this gives a conductance C for our pipe of 0.955 l s^{-1}. Knowing this conductance the problem is then reduced to measuring the average absolute pressure within the tube.

The pressure measurement in the accumulation tube during the nickel experiments was made using a thoriated iridium filament ionisation gauge, which was calibrated against another, absolutely calibrated, ionisation gauge. However, while the measurement worked well for N_2, the more reactive gases actually used experimentally such as CO and O_2 gave anomalously low readings even accounting for the differing sensitivity of the gauge to these gases due to their different ionisation cross-sections. This was probably due to the gauge having a significant pumping effect in the relatively small volume. The molecular beam was therefore measured only for nitrogen and the same intensity assumed for CO, with that for oxygen being smaller in proportion to the square root of the relative mass ratio.

Prior to the experiments on Pt{110}, however, a new accumulation tube was installed incorporating a spinning rotor gauge[11] (SRG), which gives an excellent pressure measurement even for reactive gases which is known to be stable within ~ 2% over a period of years[12] and which is calibrated absolutely[13]. The device consists of a 4.5 mm magnetised chromium-steel ball which is suspended magnetically and spun up to a rotational frequency of ~ 400 Hz using an induction motor. The motor is then switched off and the deceleration rate monitored; the deceleration rate is directly proportional to the pressure of gas acting on the ball once a constant term describing eddy current losses has been subtracted. The device has low sensitivity in the desired 10^{-7} mbar pressure range, however, and so an average over many readings over a period of several hours had to be taken to achieve good statistics, during which time the molecular beam pulsing was switched on and off so that the pressure due only to the beam could be determined above any background. The procedure was fully automated with the computer controlling the molecular beam and SRG,

storing the pressure readings and calculating the beam flux. The updated accumulation tube incorporated the further improvements of being mounted on an xyz and two tilt manipulator and having a transparent window opposite the thin pipe, to allow rapid and accurate visual alignment with the molecular beam axis using the calibration laser.

7 Sticking Measurement – Mass Spectrometer and Signal Processing

To determine the adsorbed amount of gas at each pulse, we multiply the number of molecules in each gas pulse, as determined above, by the sticking probability for that particular pulse. The sticking probability is deduced *via* the King and Wells[14] technique by monitoring the portion of the gas that reflects from the crystal using an ion-counting quadrapole mass spectrometer mounted out of line-of-sight of the sample. A zero sticking probability reference signal is obtained by inserting a gold flag just in front of the sample, using a computer-controlled solenoid.

Greater sensitivity and hence higher quality sticking probability data were obtained for the experiments on Pt compared with those on Ni by constructing new electronics to allow the mass spectrometer to be triggered directly by the computer and report back the measured mass intensities digitally; previously an analogue system was employed in which the maximum allowable count rate was limited by pulse pile-up in pulse stretching and integrating electronics. The count rate was also substantially increased by the installation of a new channeltron detector element to replace the former "Venetian blind" detector. The new system allowed sticking probabilities as low as 0.02 to be measured reliably, and additionally allowed the monitoring of different masses during a run so that, for example, the CO_2 produced by the reaction of CO with O-predosed Pt{110} could be measured in the same experiment as the CO sticking probability (see Chapter 4).

8 Data Analysis

For gases with high sticking probabilities such as CO and ethylene on Pt{110}, and O_2 on Ni{100}, the infrared signals were of sufficiently high signal to noise (up to

~ 100) for initial chemisorption that an adsorption heat and sticking probability could be extracted for every pulse of gas fired at the sample. However, at higher coverages, or where the initial sticking probability was low (such as for O_2 on CO-predosed Pt{110}, or CO on Ni{110} with large precoverages of potassium) signal averaging was required to extract reproducible data from the noise. Where several infrared signals were averaged together in this way, the corresponding mass spectrometer signals were also averaged so that a representative sticking probability could be calculated for the averaged heat. The computer program used to extract the sticking probabilities and infrared peak-to-peak heights from the raw data was written such that each signal was considered in turn, the signal to noise ratio measured and further signals averaged in as necessary until a preset signal to noise ratio was achieved. By increasing or decreasing this preset level some degree of trade-off between high coverage resolution and larger signal scatter or low coverage resolution and smaller signal scatter could be selected.

Where the data from several experiments was averaged together, the sticking probability and infrared signals (normalised according to the laser and beam flux calibrations) were averaged separately and then the average molar heat data were obtained by dividing the average infrared signals by the average sticking probabilities.

References

[1]C.E. Borroni-Bird and D.A. King, Rev. Sci. Instrum. **62** (1991) 2177.

[2]C.E. Borroni-Bird, N. Al-Sarraf, S. Andersson and D.A. King, Chem. Phys. Lett. **183** (1991) 516.

[3]C.E. Borroni-Bird, PhD thesis, University of Liverpool (1991).

[4]N. Al-Sarraf, PhD thesis, University of Cambridge (1993).

[5]J.T. Stuckless, N. Al-Sarraf, C. Wartnaby and D.A. King, J. Chem. Phys. **99** (1993) 2202.

[6]Ultrathin single crystals supplied by Jacques Chevallier, Institute of Physics and Astronomy, Aarhus University, Denmark. See for example K. Mortensen, F. Besenbacher, I. Stensgaard and C. Klink, Surf. Sci. **211** (1989) 813; F. Besenbacher, I. Stensgaard And K. Mortensen, Surf. Sci. **191** (1987) 288.

[7]T. Gritsch, D. Coulman, R.J. Behm and G. Ertl, Surf. Sci. **257** (1991) 297.

[8]*CRC Handbook of Chemistry and Physics*, 73rd ed. (CRC Press Inc., 1992).

[9]M. Zen, in *Atomic and Molecular Beam Methods*, edited by G. Scoles (Oxford University, New York, 1988), Vol. 1, Chap. 10.

[10]J.F. O'Hanlon, *A User's Guide to Vacuum Technology* (Wiley, 1980).

[11]J.K. Fremerey, J. Vac. Sci. Technol. A **3** (1985) 1715.

[12]S. Dittmann, B.E. Lindenau and C.R. Tilford, J. Vac. Sci. Technol. A **7** (1989) 3356.

[13]Calibrated to German national standard of Institut Berlin der Physikalisch-Technisce Bundesanstalt.

[14]D.A. King and M.G. Wells, Proc. Roy. Soc. Ser. A **339** (1974) 245.

Chapter Three

CO, NO and Oxygen on Pt{110}

Abstract

The reactions of CO, NO and oxygen on platinum surfaces have received a great deal of research attention, because of both their industrial importance in the three-way automobile catalytic converter and the academic interest surrounding the kinetic oscillations observed under some conditions. Crucial parameters in many of the kinetic models of these systems are the coverage-dependent heats of adsorption of the reacting species, which have hitherto been unavailable experimentally with the exception of isosteric data for CO, which are necessarily compiled over a wide range of temperature. Here the results of microcalorimetric measurements of the heat of adsorption of CO, NO and oxygen as a function of coverage on Pt{110} are presented. The initial adsorption heats are 183, 160, and 335 kJ mol^{-1} respectively.

1 Introduction

1.1 The Automobile Catalyst

The three functions of the Pt/Rh automobile catalyst are the oxidation of CO to CO_2, the reduction of NO_x to N_2 and the oxidation of unburnt hydrocarbons to CO_2 and H_2O. In the following chapter the oxidation of CO will be addressed, while prototypical hydrocarbon adsorption, in the form of ethylene, is discussed in Chapter 5. In this chapter we deal with the (separate) adsorption of CO, oxygen and NO on Pt{110} at room temperature, extracting the energetic and kinetic information for these fundamental adsorption processes from the calorimetry experiment.

A review of the surface science studies which have contributed to an understanding of the reactions which occur over the three-way catalyst has been presented by Kummer[1].

1.2 Kinetic Oscillations

The industrial and economic importance of Pt as a component of the automobile catalyst provides part of the motivation for this study. A second element is the academic interest that has arisen due to the observation of oscillatory reaction rates in chemical processes occurring on low-index Pt planes. Oscillatory kinetics in the oxidation of CO on platinum at low pressures were first reported in 1982[2] by Ertl, Norton and Rustig for Pt{100}. Since then a great deal of work has been performed in the surface science community; Imbihl[3] has recently presented a detailed review of oscillatory reactions on Pt and Pd including CO oxidation and NO reduction by CO, H_2, or NH_3, with some 300 references.

Although the many mathematical models of the reaction kinetics have been reasonably successful in imitating the experimentally observed behaviour, the coverage dependence of the adsorption energies of the reacting species has frequently been neglected. For example, Imbihl, Cox and Ertl[4] presented a model for the oscillations on Pt{100} but mentioned the unknown repulsions between adsorbates as being a limitation of the model. Engstrom and Weinberg[5] demonstrated the importance of coverage dependence of energetic data in the CO oxidation kinetics on Pt{110}, finding a variation in the reaction activation energy varying between 22 and 8 kcal mol^{-1} depending on oxygen coverage. Similarly Campbell *et al*[6] found a variation between 24 and 12 kcal mol^{-1} on Pt{111} in a molecular beam study.

2 CO on Pt{110}

2.1 Review of Previous Studies

In the case of CO on Pt{110} reliable coverage-dependent heat of adsorption data are available from a nuclear microanalysis (NMA) study by Jackman *et al*[7]. By measuring absolute equilibrium CO coverages as a function of temperature and pressure, isosteres could be constructed using temperatures between 450 and 600 K and pressures ranging from $3 \infty 10^{-5}$ to $3 \infty 10^{-3}$ Pa. The heats they obtained are

shown together with our calorimetric data in Figure 1 (presented in the following section), and the level of agreement is discussed below. Prior to this work a single point on the adsorption heat curve was found by Comrie and Lambert[8], who extracted an isostere for one particular coverage by observing the pressure-temperature dependence of the position of a phase transition visible in LEED. They obtained a value of 133 ± 4 kJ mol^{-1} for the (1 ∞ 1) to (2 ∞ 1)p1g1 transition for which Jackman *et al* estimate a coverage of 0.78 ± 0.05 ML, close to the room-temperature saturation coverage of 0.88 ML. Two non-isosteric estimates for the desorption activation energy of CO were in close agreement: Engstrom and Weinberg[9] found a desorption rate constant of $3 \infty 10^{14}$ exp(–36 ± 1.5 kcal mol^{-1} / *RT*) s^{-1} using a surface temperature modulation technique while Fair and Madix[10] obtained $6 \infty 10^{14}$ exp(–35.3 kcal mol^{-1} / *RT*) s^{-1} at low coverage, with a repulsive interaction parameter ω = 1.5 + 2.5θ kcal mol^{-1}, using a modulated molecular beam method. The low-coverage value of 36 kcal mol^{-1} is equivalent to an initial adsorption heat of 150 kJ mol^{-1}.

Aside from energetic data, a thorough study of the room-temperature phase diagram using HREELS, RAIRS, TDS, LEED and angle-resolved ultraviolet photoemission spectroscopy (ARUPS) was performed by Bare, Hofmann and King[11][12]. Three phases were found as a function of coverage during room-temperature adsorption. Below 0.2 ML, isolated CO species on the reconstructed (1 ∞ 2) surface coexist with nucleating islands of CO on (1 ∞ 1) "deconstructed" areas. Between 0.2 and 0.5 ML island growth of the (1 ∞ 1) phase occurs, and above 0.5 ML island growth saturates and the (1 ∞ 1) becomes disordered (in LEED) as more CO are packed in to the adlayer. The ARUPS results indicated that the CO adsorbed on (1 ∞ 1) areas was tilted by an estimated 26° from normal, but the isolated species on the (1 ∞ 2) upright. The transition to the (2 ∞ 1)p1g1 structure at 0.8 ML used by Comrie and Lambert could only be obtained by annealing, explained by the presence of defects from the (1 ∞ 2) ∅ (1 ∞ 1) transition at room temperature blocking long range order. Further insight into the (1 ∞ 2) ∅ (1 ∞ 1) transition was provided by an STM study[13] which demonstrated that (1 ∞ 1) island nucleation,

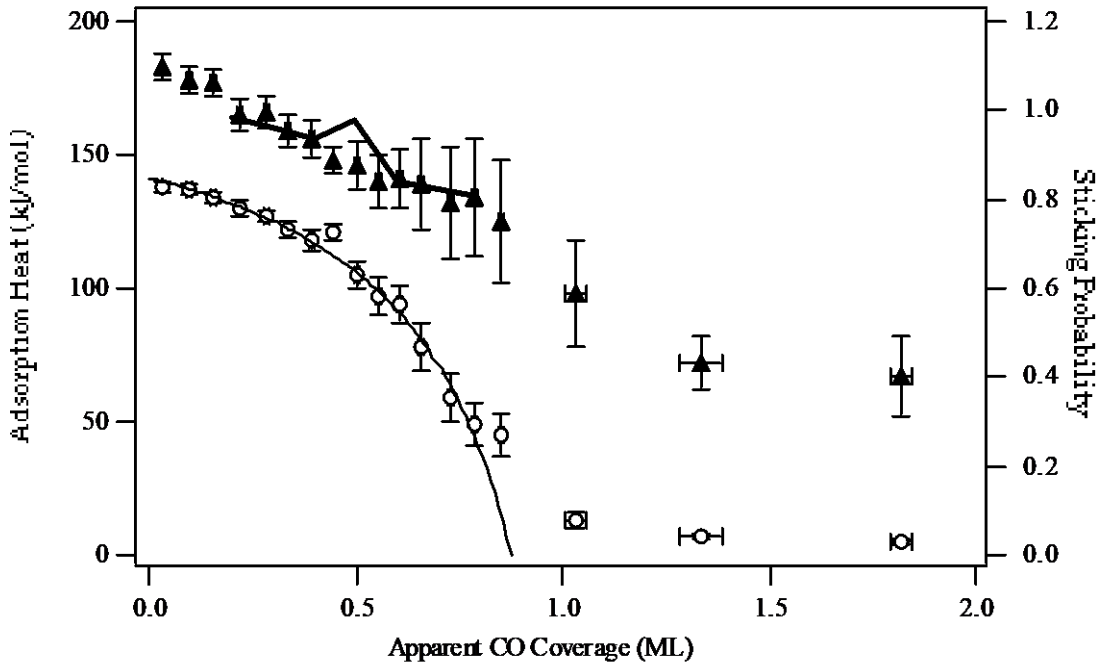

Figure 1. Adsorption heat (filled triangles) and sticking probability (open circles) for CO on Pt{110} at 300 K. The bold solid line running through the heat data show the isosteric results of ref [7], while the line through the sticking data shows a fit to the Kisliuk expression describing precursor-mediated adsorption.

beginning after 0.8 L exposure, is homogeneous and slow at room temperature, with the island location uncorrelated with steps and formation taking several minutes to complete. This implies that when considering our results, the adsorption heat may correspond to that of CO on the surface prior to the reconstruction. With increasing CO coverage, more islands tend to form rather than existing islands growing. At 350 K, by contrast, the additional mobility of Pt atoms encourages island growth and heterogeneous nucleation becomes significant.

2.2 Calorimetric Adsorption Heat Data for CO on Pt{110}

The microcalorimetric results are shown in Figure 1. The initial heat of adsorption at 300 K is 183 ± 7 kJ mol^{-1}, declining monotonically to 146 at 0.5 ML and 125 kJ mol^{-1} at the expected[7] saturation coverage of 0.88 ML. Our coverage scale extends indefinitely beyond the true saturation coverage, because the adsorption heat eventually drops sufficiently that desorption between pulses exactly compensates

for the adsorption during pulses, for which we (correctly) measure a finite sticking probability (see sectio 2.4 below). In this steady-state regime, each dose of gas adsorbs with a heat of 70 kJ mol^{-1}. The error bars indicate the standard error between experimental runs and not the expected absolute error.

Comparing the data with the phase diagram of Hofmann, Bare and King[11],[12] we see a downwards step in the heat curve of ~ 12 kJ mol^{-1} at 0.2 ML, from which point onwards CO adsorption should be followed by reconstruction to (1 ∞ 1). As the STM results[13] indicate that the reconstruction reaches completion on a longer timescale than our heat measurement, this may indicate that reconstruction occurs here because the heat of adsorption on the (1 ∞ 2) surface drops quickly rather than indicating a lower heat of adsorption on the reconstructed surface. Although there is no steepening of the curve at 0.5 ML, where infilling of the completed (1 ∞ 1) adlayer should begin, there is a progressive decline in adsorption heat above 0.2 ML.

The isosteric data of Jackman *et al*[7] are shown on the figure for comparison, and with the exception of the point at 0.5 ML are in near-perfect agreement with the calorimetric data, despite their expected error bars of ± 15 kJ mol^{-1}. This remarkable degree of agreement between our data and that obtained by a quite different technique suggest that our absolute calibrations (of molecular beam intensity, laser power, and crystal reflectivity) are accurate. Although the 0.5 ML point is still within the expected error limits, we should note that this coverage marks the completion of the (1 ∞ 1) phase and the beginning of further infilling of the adlayer, which we would expect to be associated with strong adsorbate repulsions. The isosteric data are measured at 450 to 600 K, at which temperatures a well-ordered adlayer would be expected with the CO in the most favourable thermodynamic arrangement; the calorimetric data are measured at 300 K, where poor order is expected, with some CO entering the less favourable adsorption sites before 0.5 ML is reached. A lower average adsorption heat is thus reasonable at this coverage for the calorimetric data. However, the increase in binding energy between 0.4 and 0.5 ML seen in the isosteric data seems in any case improbable and may simply be noise, as the

fluctuation is smaller than the error bars given by the authors. For coverages below 0.5 ML the isosteric measurements will certainly be for CO adsorbing onto (1 ∞ 1), while as mentioned above, our measurements might represent the adsorption heat onto the (1 ∞ 2) with reconstruction occurring slowly. As the two datasets agree well, either the adsorption heat for the two cases is coincidentally the same or the reconstruction is largely complete on a timescale of ~ 50 ms.

2.3 Sticking Probability Data

The sticking probability curve exhibits precursor-mediated behaviour which is well fitted up to 0.75 ML by the Kisliuk expression[14]:

$$\frac{S}{S_0} = \left(1 + \frac{\theta / \theta_S}{1 - \theta / \theta_S} K\right)^{-1} \qquad (1)$$

Here the sticking probability S is given in terms of the instantaneous coverage θ, the saturation coverage θ_S, the initial sticking S_0 and a parameter K which describes the degree of mobility of the precursor; small values correspond to a highly mobile precursor while K=1 corresponds to an immobile precursor and hence simple Langmuir kinetics. The least-squares fit to these data gives K=0.25 and an initial sticking probability s of 0.83. The model neglects adsorbate interactions (other than site-blocking) and adlayer ordering.

The saturation coverage obtained by extrapolating the fit curve to zero sticking is 0.88 ML, indistinguishable from the nuclear microanalysis results[7]. It is interesting to note that the phase changes at 0.2 and 0.5 ML produce no discernible perturbation of the CO uptake.

2.4 Analysis of Steady-State Data

In principle further information can be extracted from the steady-state data acquired once adsorption is complete. In this regime the quantity of gas desorbing between molecular beam pulses exactly balances that adsorbing during the pulses, giving no

net accumulation on the crystal. The sticking probability measured during the pulse multiplied by the number of molecules in the pulse gives that number of molecules which adsorb and then desorb during the 2.5 s between pulses, while the adsorption heat can be equated with the desorption activation energy assuming non-activated adsorption. With this knowledge of the absolute desorption rate and activation energy the pre-exponential factor ν can be obtained assuming that a simple first-order Arrhenius expression describes the kinetics.

In the steady-state regime the sticking probability, s = 0.0365 ± 0.001 and the adsorption heat q = 69 ± 7 kJ mol^{-1}. The average number of molecules in the molecular beam pulse, N = (2.55 ± 0.04) ∞ 10^{12} and the sample area is 0.033 cm^2. The saturation coverage of CO, θ_s is taken to be 0.88 ML[7] and 1 ML + 9.22 ∞ 10^{14} molec cm^{-2}. We assume that the adlayer is reasonably homogeneous and so the coverage θ in the desorption rate expression is the total surface coverage θ_s .

$$\frac{d\theta}{dt} = \theta \nu e^{-q/RT} \qquad (2)$$

$$\nu = 2.5 \infty 10^{(9 \pm 1.2)}\ s^{-1}$$

This value is unreasonably small compared to accepted values of the order of 10^{14} s^{-1}, similar to a vibrational frequency. Two assumptions used to obtain this figure are first, that the kinetics follow a first-order Arrhenius rate law, and second that the adlayer is homogeneous. Considering the latter first, if only part of the adlayer contributed to the pool available for desorption, and we set up an equilibrium only with this part, then we should use a smaller value of θ and so arrive at a larger value of ν. However, the "special" phase would have to be less abundant by five orders of magnitude or so than the total coverage, which would be considerably less than the 10^{-3} ML added during each pulse. Furthermore the literature work detailed in Section 2.1 suggests a continuous compression of the (1 ∞ 1) adlayer to form a p1g1 phase complete at 1 ML, with all CO similar.

The other assumption was of simple first-order kinetics. The sticking curve of Figure 1 clearly shows that adsorption proceeds via a mobile intermediate, which will also be a possible intermediate species during *desorption*, providing a reaction channel back to the chemisorbed state. The kinetic consequences of this are explored by King[15], who finds that the desorption rate is reduced by a factor *F*, given by the following expression, containing a Kisliuk-type term:

$$F = f_d + f_m \left\{ 1 - \left(1 + f_d / f_a\right)^{-1} \left[1 + K \frac{\theta}{1-\theta} \right]^{-1} \right\} \quad (3)$$

where f_d, f_m and f_a are the probabilities of a precursor-state molecule above an empty site desorbing, migrating to a neighbouring site, and chemisorbing respectively, and *K* is identical to the Kisliuk constant in Equation (1), containing similar probabilities (except for chemisorption) for a molecule above a filled site; θ is the fractional coverage relative to saturation. As demonstrated in ref. [15], inserting this factor *F* into Equation (2) gives increasingly broad thermal desorption peaks shifting to increasingly higher temperature as the mobility of the adlayer increases, using a fixed desorption energy and frequency factor. Where the energy and desorption rate are known, we would conclude the frequency factor was much smaller than expected fitting a thermal desorption spectrum using Equation (2) without taking Equation (3) into account. It is noted[15] that this is of particular significance in a closely related system to that considered here, CO/Pt{111}, with a relatively large value of $(1+f_d/f_a)^{-1}$ (proportional to the initial sticking probability of 0.6), coupled with a small value of *K* (~ 0.1), to give small values of *F*. Here the initial sticking probability is higher still at 0.83 though K too is higher (corresponding to a less mobile precursor) at 0.25. Unfortunately the magnitudes of f_d and f_m cannot be extracted from our data and so we cannot deduce *F*, but in any case it can only serve to reduce the value of the frequency factor we extract from Equation (2).

As we have achieved equilibrium, the Gibbs free energy change for adsorption should be zero. Knowing the enthalpy change ΔH (= –q, where q is the calorimetric adsorption heat) we can then infer the entropy change ΔS:

$$\Delta G = \Delta H - T\Delta S = 0 \qquad (4)$$

$$\Delta S = \Delta H / T \qquad (5)$$

The standard entropy of CO (at 1 atm and 298 K) is 198 J K mol^{-1}, and assuming perfect gas behaviour then we can calculate S at our effective average pressure of ~ 10^{-5} Pa for the gaseous starting material:

$$S = S^0 - R \ln (p / p^0) \qquad (6)$$

giving typical values of $S_{(g)}$ = 400 J K mol^{-1}. Knowing this and the entropy change of adsorption, ΔS, we can then quote a value for the differential entropy of the adsorbed species by combining equations (5) and (6):

$$S_{(a)} = S^0 - R \ln (p / p^0) - q / T \qquad (7)$$

This yields $S_{(a)}$ = (170 ± 25) J K mol^{-1}, compared to typical values for CO on Ni single crystal planes[16] of just 50 to 70 J K mol^{-1}. This relatively high differential entropy for the adsorbed state will give rise to a "genuinely" low desorption frequency factor according to transition state theory, as discussed in Section 4.3 of Chapter 8 for CO with a range of K precoverages on Ni{110}.

3 Oxygen on Pt{110}

3.1 Review of Previous Studies

The interaction of oxygen with the Pt{110} surface has not been the subject of many studies and no consistent estimate of the binding energy has been achieved. Wilf and Dawson[17] studied oxygen adsorption on Pt{110} using LEED, Auger and TDS. They found a single desorption peak appearing at 860 K at low coverages, shifting

down to 775 K at high coverages, which they fitted using a desorption energy of 133 or 123 kJ mol^{-1} fitting the peak to first or second-order kinetics respectively. However, Campbell *et al*[18] obtained an activation energy ranging from 51 to 42 kcal mol^{-1} (213 to 176 kJ mol^{-1}) for oxygen desorption from the less reactive Pt{111} surface using TDS, while Norton *et al*[19] obtain 160 kJ mol^{-1} for oxygen on Pt{100}. Coulston *et al*[20] predicted an adsorption heat of ~ 230 kJ mol^{-1} for oxygen coverages greater than 0.2 ML on Pt, although they seem to be quoting double the 230 kJ mol^{-1} found for oxygen/Pt{100} from TDS by Derry and Ross[33]. This compares with an estimate of 85 ± 5 kcal mol^{-1} (355 ± 21 kJ mol^{-1}) for oxygen on Rh{111} by Root and Schmidt[21] by TDS. Ray[22] performed molecular orbital calculations giving binding energies for oxygen on Pt{111} of 4.15, 3.08 and 3.01 eV for the atop, bridge and three-fold sites respectively (400-290 kJ mol^{-1}). Brennan *et al*[23] made calorimetric measurements of the heat of adsorption of oxygen on a range of polycrystalline transition metal films, finding an initial heat of 295 kJ mol^{-1} in the case of Pt.

Separately from energetic data, Ducros and Merrill[24] found an initial sticking probability of approximately 0.4 at room temperature for oxygen on Pt{110}. Freyer *et al*[25] performed a quantitative XPS and work-function study, from which they found a saturation coverage for room temperature adsorption onto the (1 ∞ 2) reconstructed surface of 0.35 ML with an initial sticking probability of 0.3; they ascribed a glitch in the work function curve at 0.2 ML to a change from adsorption on row sites to adsorption instead onto facet sites. Two adsorption sites were suggested also by Schmidt, Stuhlmann and Ibach[26] in an EELS study in which they found two Pt-O stretch peaks, at 480 and 330 cm^{-1}, the latter appearing only after ~ 3 L exposure.

3.2 Calorimetric Data for Oxygen on Pt{110}

The averaged results of 8 experiments are shown in Figure 2, where again the error bars indicate the standard error ($\sigma/\sqrt{N}$) between runs. The initial adsorption heat is

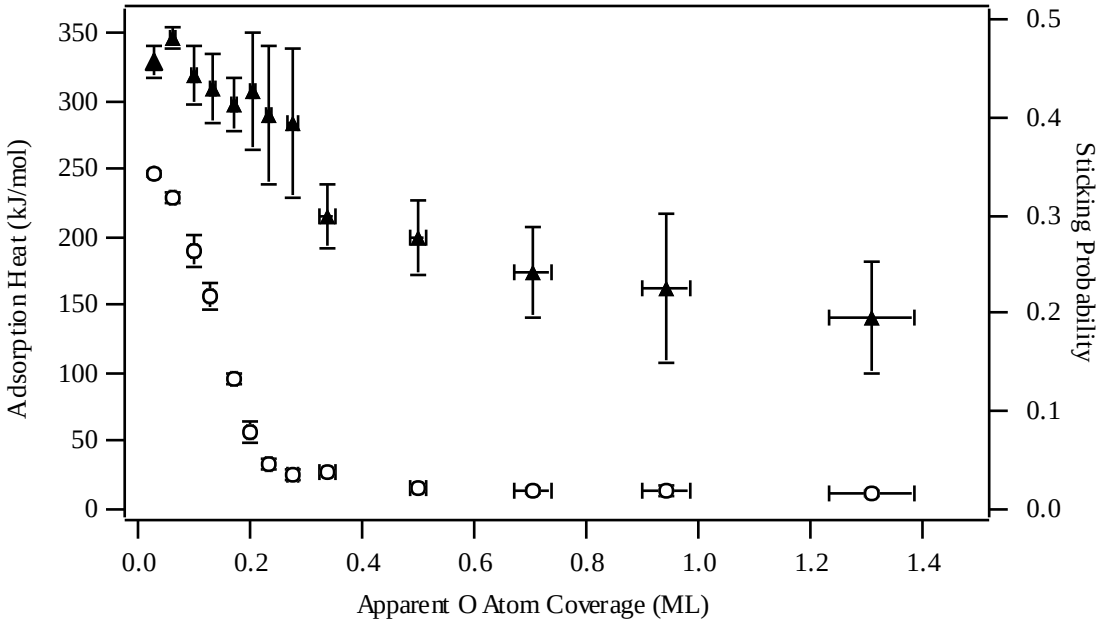

Figure 2. Adsorption heat (filled triangles) and sticking probability (open circles) for oxygen on initially clean Pt{110} at 300 K.

332 ± 10 kJ mol^{-1}, declining rapidly with coverage to only 215 ± 24 kJ mol^{-1} at 0.35 ML and leveling out at a steady-state value of 153 ± 50 kJ mol^{-1}. The large error bars on the latter values are due to the very small sticking probability, which ranges from 0.34 at coverages close to zero to just 0.04 ± 0.004 at 0.35 ML and 0.029 ± 0.003 in the steady-state regime.

The initial adsorption heat is considerably larger than the TDS estimates[17][18][20] above, but in line with the calculated binding energies obtained by Ray[22], and only ~ 10% higher than the calorimetric heat for polycrystalline Pt according to Brennan *et al*[23]. No abrupt change in the adsorption heat is seen at 0.2 ML, where a change of adsorption site was suggested by Freyer *et al*[25], although a sudden drop of ~ 70 kJ mol^{-1} is seen at 0.3 ML; however, this is close to the estimated saturation coverage[25] and so could mark the onset of some reversible adsorption, although our sticking and heat curves continue to trend downwards until ~ 0.5 ML.

The adsorption heat in the steady-state regime is 153 ± 50 kJ mol^{-1}, which is rather high for a spontaneously-desorbing species, though the lower end of the confidence

interval would be reasonable. The sticking probability is sufficiently low (0.03) that we should consider whether competing adsorption from residual gas in the vacuum chamber could have some significant effect. In particular, CO will adsorb with a sticking probabililty of ~ 0.6 (see Chapter 4) and efficiently remove oxygen as CO_2 to give a new adsorption site for oxygen chemisorption, which will then occur with a higher adsorption heat than for a weakly-bound molecule on a saturated adlayer. The total residual gas pressure in the experimental chamber was typically $8 \infty 10^{-11}$ mbar. Were this due only to CO, then converting this to a molecular impingement rate, oxygen atoms will be removed at a rate of

$$\frac{8\times10^{-11}\times100\times0.6}{\sqrt{2\pi mkT}} = 1.4\times10^{14}\ \text{molec m}^{-2}\ \text{s}^{-1}$$
$$\equiv 1.5\times10^{-5}\ \text{ML s}^{-1}$$

Oxygen adsorption takes place at rate of $4.8 \infty 10^{-4}$ (molec)ML s^{-1} or $9.5 \infty 10^{-4}$ (atom)ML s^{-1}, some two orders of magnitude more. Only a negligible contribution of ~ 1.5% of oxygen adsorption will therefore occur onto new clean sites created by CO and so the unexpectedly high heat of adsorption is not explained in this way.

4 NO on Pt{110}

4.1 Review of Previous Studies

There have been only a handful of studies dealing with NO adsorption on Pt{110}. The first was by Lambert and Comrie[27] in 1974 dealing briefly with CO and NO adsorption and their interaction in more detail, followed by another[28] in 1976 concentrating on NO adsorption alone. TDS showed a dominant sharp peak at 450 K accompanied at high coverages by a low-temperature shoulder at 390 K. A broad mass 28 desorption peak at 490 K was attributed to N_2 desorption indicating NO dissociation, although no corresponding O_2 desorption was detected. The proportion of molecules dissociating was estimated to be < 20%. They reported that

the (1 ∞ 2) clean surface reconstruction was lifted by NO at room temperature analagously to the behaviour of CO.

Gorte, Gland and Schmidt[29] studied NO/Pt{110} by TDS and parametrized the desorption rate as $10^{(16 \pm 0.5)}$ exp(–(33.5 ± 1) kcal mol^{-1} / *RT*) s^{-1} by applying a variable heating rate method to the sharp peak which they report at 450 or 470 K (along with weaker features at lower desorption temperatures). They also observed N_2 desorption at 500 K suggesting a dissociated fraction of ~ 15%. We might therefore expect to measure a calorimetric heat of 140 kJ mol^{-1} corresponding to the molecular NO or some higher value if that dissociation should occur at room temperature, accompanied by some lower adsorption heat species at high coverages. EELS spectra[30] further showed that two types of NO were present following adsorption at 230 K with a 1610 cm^{-1} band present at low coverage being accompanied by a second band at 1760 cm^{-1} at coverages of > 30% of saturation, which were attributed to bridge-bound and atop molecules respectively. A c(4 ∞ 8) LEED pattern developed simultaneously with the appearance of the 1760 cm^{-1} species. The two species were present also following adsorption at 100 K and heating to 300 K. The 1620 cm^{-1} peak was associated with the sharp desorption peak at 450 K. Lifting of the (1 ∞ 2) reconstruction occurred only upon heating above 300 K but below 350 K.

Finally Freyer *et al*[31] have presented XPS and work-function change measurements. Their X-ray data contradict the findings of the previous studies in that no atomic oxygen was seen, implying that no NO dissociation occurred, even following repeated cycles of NO dosing and desorption. Calibrating coverages by reference to the 0.5 ML CO/Pt{111}-c(4 ∞ 2) structure they estimated a saturation coverage of 0.6 ML at 300 K and 0.9 ML at 120 K (the latter compares with 1.08 ± 0.07 ML by NRA[7]). The O(1s) spectra for adsorption on the (1 ∞ 1) surface indicated the possible occurrence of two types of NO on the surface at coverages of ~ 0.5 ML, although the spectra were too noisy to perform an unambiguous fit; only one broad peak was seen on the (1 ∞ 2) surface, however, during thermal desorption from an

initially saturated adlayer. The (1 ∞ 2) to (1 ∞ 1) reconstruction was noted at 370 K in LEED.

4.2 Calorimetric Data for NO on Pt{110}

4.2.1 Experimental Detail

The molecular beam flux measurements for NO were performed using the improved accumulation tube incorporating the spinning rotor gauge (see Chapter 2). During initial experiments an anomalously low beam flux was measured. This problem was solved by allowing a considerably longer time to achieve an equilibrium pressure in the tube compared with the other gases used (~ 1 hr rather compared to ~ 1 min), which was probably required due to reactions between the highly reactive NO and adsorbates on the tube walls giving rise to additional residual gas. The beam flux used in the initial experiments was then corrected by applying the measured ratio between a similar CO beam flux and the NO flux, measured using the long equilibration time, to CO beam measurements performed at the time of those experiments.

4.2.2 Results and Discussion

The adsorption heat and sticking probability data are presented in Figure 3. It is apparent that two heat regimes are present: the initial heat is 160 kJ mol^{-1}, and (within errors) remains constant for the first 0.2-0.25 ML. The curve then drops abruptly to 140 kJ mol^{-1} and again remains constant up to approximately 0.67 ML, before dropping steeply towards the reversible value of 95 kJ mol^{-1}. The two-stage adsorption sequence is consistent with the EELS data[30], with the 1610 cm^{-1} species quoted as accounting for the first 30% (or 0.27 ML using our extrapolated sticking curve which gives saturation as 0.9 ML) followed by the 1760 cm^{-1} species which grows in and eventually dominates the first species by a factor of ~ 2.

The long plateau at 140 kJ mol^{-1} does not correspond with the sharp 450 K peak for which a desorption energy of 140 kJ mol^{-1} was estimated[30], because that peak

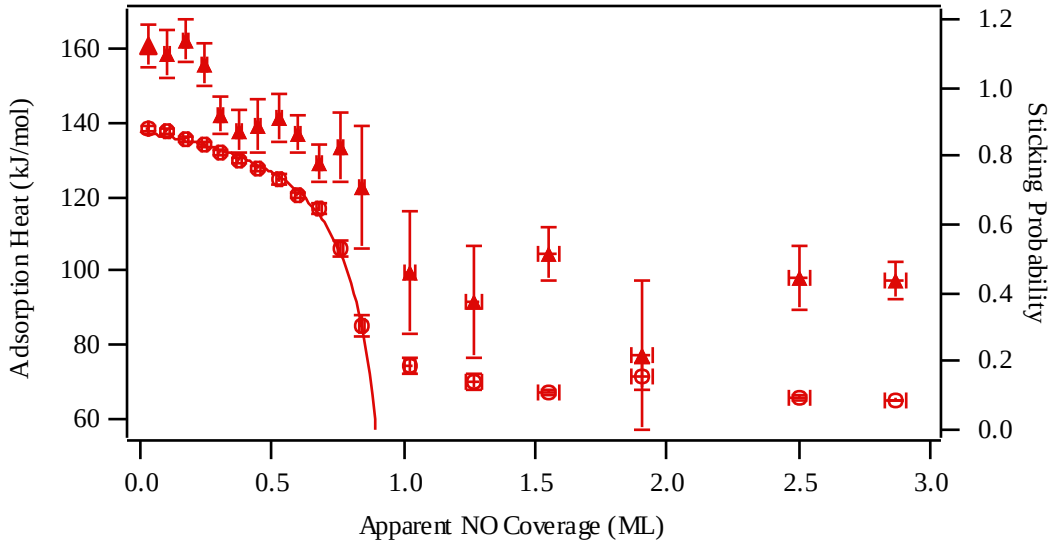

Figure 3. Adsorption heat (filled triangles) and sticking probability (open circles) for NO adsorption on Pt{110} at 300 K. The solid line through the sticking data shows a fit to the Kisliuk expresssion.

corresponded to the low-coverage species which we find adsorbs with an energy of 160 kJ mol^{-1}. Furthermore at coverages where EELS at 230 K shows approximately equal coverages of the two species, TDS show very little contribution from that which adsorbs second. The TDS may be complicated by the contribution from the recombination of any dissociated NO, and during the thermal ramp the surface undergoes reconstruction and the adsorbate molecules may shift site; so in this case, desorption at 450 K is by no means the reverse process of adsorption at 300 K, and TDS cannot provide detailed information of the energetics of the adsorbed species at room temperature. Only calorimetry can provide this data experimentally.

The sticking probability data are reasonably described by the Kisliuk expression (see Equation (1)), indicative of precursor-mediated kinetics, as for CO on this surface, but with an initial sticking probability of 0.87 and K = 0.12. The sticking curve would extrapolate to zero at a coverage of approximately 0.9 ML, as does that for CO, some 50% more than indicated by the XPS results[31]; additionally, there is a significant decline in the measured sticking for another 0.3 ML, although the data here could represent some mixture of reversible and "permanent" adsorption in which case less than 0.3 ML is actually added to the surface in this range.

In the steady-state regime attained after saturation of the overlayer, the sticking probability and adsorption heat for each pulse of gas remain constant at 0.09 and 95 kJ mol^{-1} respectively. Applying the same quasi-equilibrium analysis as for CO above using Equation (2), we arrive at a first-order desorption frequency factor of $8.2 \infty 10^{13}$ s^{-1}, a reasonable value yet some two orders of magnitude lower than the estimate of 10^{16} s^{-1} from the analysis of Gland *et al*[30]. Again, this analysis neglects the effect of precursor-mediated desorption.

Assuming the approximation to equilibrium is valid, we can further extract the differential entropy of the adsorbed gas added during the pulse using Equation (7). The standard entropy[32] of gaseous NO, S^0, may be taken as 210.65 J K^{-1} mol^{-1} at 298 K and a standard pressure p^0 = 1 atm. This gives a value for the differential entropy of the adsorbed gas S = 87 ± 23 J K^{-1} mol^{-1} and hence an entropy change for the adsorption process of ΔS = –124 ± 23 J K^{-1} mol^{-1}.

5 Conclusions

The initial adsorption heats of CO, O_2 and NO on Pt{110} at 300 K are 183, 335 and 160 kJ mol^{-1} respectively. Both the absolute magnitude and the coverage dependence of the CO data are in excellent agreement with existing isosteric measurements[7] based on absolute coverage measurements, strongly indicating that the calibrations used in these experiments were reliable. In all three cases the adsorption heat shows a strong coverage dependence, which in the case of NO appears to correlate with two different adsorbed phases previously elucidated from EELS[30]. This coverage dependence of the adsorption heat should be valuable in kinetic models which describe the desorption rate of these species at different coverages. In addition, these data will be essential in interpreting the *reaction* heat results for CO and oxygen presented in the following chapter.

The initial sticking probabilities of the three gases are 0.83, 0.34 and 0.87 respectively, while the negative curvature of the sticking versus coverage curve, well fitted by the Kisliuk expression of Equation (1), clearly shows precursor-

mediated uptake kinetics for CO and NO with a possible weaker effect for oxygen also.

References

[1]J.T. Kummer, J. Phys. Chem. **90** (1986) 4747.

[2]G. Ertl, P.R. Norton and J. Rustig, Phys. Rev. Lett. **49** (1982) 177.

[3]R. Imbihl, Prog. Surf. Sci. **44** (1993) 185.

[4]R. Imbihl, M.P. Cox and G. Ertl, J. Chem. Phys. **83** (1985) 1578.

[5]J.R. Engstrom and W.H. Weinberg, Surf. Sci. **201** (1988) 145.

[6]C.T. Campbell, G. Ertl, H. Kuipers and J. Segner, J. Chem. Phys. **73** (1980) 5862.

[7]T.E. Jackman, J.A. Dvies, D.P. Jackson, W.N. Unertl and P.R. Norton, Surf. Sci. **120** (1982) 389.

[8]C.M. Comrie and R.M. Lambert, J. Chem. Soc. Faraday I **72** (1976) 1659.

[9]J.R. Engstrom and W.H. Weinberg, Surf. Sci. **201** (1988) 145.

[10]J. Fair and R.J. Madix, J. Chem. Phys. **73** (1980) 3480.

[11]P. Hofmann, S.R. Bare and D.A. King, Surf. Sci. **117** (1982) 245.

[12]S.R. Bare, P. Hofmann and D.A. King, Surf. Sci. **144** (1984) 347.

[13]T. Gritsch, D. Coulman, R.J. Behm and G. Ertl, Phys. Rev. Lett. **63** (1989) 1086.

[14]P. Kisliuk, J. Phys. Chem. Solids **3** (1957) 95.

[15]D.A. King, Surf. Sci. **64** (1977) 43.

[16]J.T. Stuckless, N. Al-Sarraf, C. Wartnaby and D.A. King, J. Chem. Phys. **99** (1993) 2202.

[17]M. Wilf and P.T. Dawson, Surf. Sci. **65** (1977) 399.

[18]C.T. Campbell, G. Ertl, H. Kuipers and J. Segner, Surf. Sci. **107** (1981) 220.

[19]P.R. Norton, K. Griffiths and P.E. Bindner, Surf. Sci. **138** (1984) 125.

[20]G.W. Coulston and G.L. Haller, J. Chem. Phys. **95** (1991) 6932.

[21]T.W. Root and L.D. Schmidt, Surf. Sci. **134** (1983) 30.

[22]N.K. Ray and A.B. Anderson, Surf. Sci. **119** (1982) 35.

[23]D. Brennan, D.O. Hayward and B.M.W. Trapnell, Proc. Roy. Soc. A **256** (1960) 81.

[24]R. Ducros and R.P. Merrill, Surf. Sci. **55** (1976) 227.

[25]N. Freyer, M. Kiskinova, G. Pirug and H.P. Bonzel, Surf. Sci. **166** (1986) 206.

[26]J. Schmidt, C. Stuhlmann and H. Ibach, Surf. Sci. **284** (1993) 121.

[27]R.M. Lambert and C.M. Comrie, Surf. Sci. **46** (1974) 61.

[28]C.M. Comrie, W.H. Weinberg and R.M. Lambert, Surf. Sci. **57** (1976) 619.

[29]R.J. Gorte, L.D. Schmidt and J.L. Gland, Surf. Sci. **109** (1981) 367.

[30]R.J. Gorte and J.L. Gland, Surf. Sci. **102** (1981) 348.

[31]N. Freyer, M. Kiskinova, G. Pirug and H.P. Bonzel, Appl. Phys. A **39** (1986) 209.

[32]A.M. James and M.P. Lord, *Macmillan's Chemical and Physical Data*, p459 (Macmillan, London, 1992).

[33]G.N. Derry and P.N. Ross, Surf. Sci.**140** (1984) 165.

Chapter Four

Calorimetric Measurement of Catalytic Surface Reaction Heat: CO Oxidation on Pt{110}

Abstract

The technique of single crystal adsorption microcalorimetry has for the first time been applied to the study of a catalytic reaction, namely the oxidation of CO on a Pt{110} substrate at room temperature. By comparing the measured heat deposited in the crystal with that expected for the reaction, the excess energy removed by the desorbing CO_2 molecules can be deduced. It is found that when CO is dosed onto a saturated oxygen overlayer, the product CO_2 molecules remove only 9 ± 17 kJ mol^{-1} more energy than expected for thermally accommodated molecules. However, when oxygen is dosed onto a CO overlayer, the product CO_2 molecules remove 52 ± 21 kJ mol^{-1} of excess energy. We suggest that the more highly excited CO_2 molecules are formed by reaction of CO molecules with "hot" oxygen adatoms produced by the dissociation process and not thermally accommodated to the surface.

1 Introduction

The heat change associated with a reaction is thermodynamic information of fundamental importance in understanding the process; however, despite the application of a plethora of surface probes this quantity has never been directly accessible for reactions on single crystal surfaces. One of the most extensively studied catalytic reactions, as discussed in the previous chapter, is the oxidation of CO on Pt surfaces, and here we report the first direct calorimetric measurements of the heat of reaction for CO and oxygen on Pt{110}.

This reaction is of particular interest because it is well known that the CO_2 molecules produced on Pt surfaces can be ejected into the gas phase with a translational, vibrational and rotational energy in excess of that expected from the substrate temperature[1,2]. The excess translational energy alone can be some 56 kJ mol^{-1} in the

reaction of atomic oxygen with CO on Pt{111}[3], although under some circumstances the highly excited product is accompanied by thermally accommodated molecules giving bimodal angular and time-of-flight (TOF) distributions[4,5]. The characteristic vibrational temperature of the CO_2 produced on polycrystalline foils varies somewhat between vibrational modes but increases with surface temperature from[2,6] about 1250 K with T_s = 750 K, to[7] 1900 K with T_s = 1000 K. In the present work, for the first time, the heat released during a catalytic reaction is measured calorimetrically, giving a direct measure of the total excess energy carried away by the products.

2 Review of Excited CO_2 Formation

2.1 Kinetic Energy

The first indication that the CO_2 molecules produced by CO oxidation on platinum left the surface with excess energy was the peaked angular distribution measured by Palmer[8] in 1974, using Pt{111} films grown epitaxially on a mica substrate. The first direct measurement of the kinetic energy of the product molecules was performed[1] by Becker, Auerbach and co-workers in 1977. A chopped molecular beam of CO was directed at the sample, which was maintained in an ambient pressure of oxygen, and the time-of-flight spectrum of the CO_2 was collected at normal and 45° from it, giving rise to translational temperatures $\langle E_{kinetic}/2k \rangle$ of 1780 and 1070 K respectively for molecules formed on a Pt foil maintained at only 880 K. This is equivalent to an *excess* translational energy of 15.0 and 3.2 kJ mol^{-1} respectively.

Two recent studies have shown that under some circumstances the highly excited CO_2 can be accompanied by a second component that is thermally accommodated to the surface, as shown by bimodal angular and TOF distributions. Poehlmann *et al*[5] measured TOF and angular distributions for CO_2 molecules desorbing from a Pt{111} crystal on which the reaction was maintained in steady state using a chopped molecular beam of CO and continuous exposure of oxygen at a temperature of 550 K. They found a thermalised Maxwellian contribution following

a $cos\ \theta$ angular distibution coexisting with a component following a $cos^8\theta$ distribution with an excess of 0.4 eV or 39 kJ mol^{-1} kinetic energy, and noted that the thermally accommodated fraction increased with increasing oxygen coverage. Allers *et al*[4] performed a temperature-programmed reaction (TPR) experiment in which layers of molecular oxygen and CO were coadsorbed (in that order) at 100 K and then the CO_2 pressure, TOF spectrum and angular distribution were recorded as the crystal was heated to 400 K or more. Four CO_2 desorption peaks were found: α, β_3, β_2 and β_1 at 145, 210, 250 and 330 K respectively. Of these all showed some energetic, peaked nature but only the β_1 peak showed a bimodal distribution. The α peak corresponded to the dissociation temperature of O_2 and showed a particularly peaked TOF spectrum, indicating a reaction channel coupled to the dissociation process at low temperature. This result is of particular interest in the light of our findings.

A similar TPR study was performed by Matsushima *et al*[9] on the Pt{110} surface, although unfortunately the sample was heated to remove or dissociate O_2 molecules prior to the CO dose, so that no analogue of the α peak seen by Allers was found. Interestingly the angular distribution of desorbed CO_2 was split into two peaks along the [001] direction, at least for low CO coverages, indicating desorption perpendicular to the {111}-like microfacets of the (1 ∞ 2) missing-row reconstructed surface. Four peaks were observed in the TPR spectrum, with 410 and 310 K peaks present only at low initial CO coverages being accompanied by 250 and 170 K peaks at higher CO coverages. TOF analysis was performed for the two higher temperature peaks with a fit producing a translational temperature of 1450 ± 100 K, or an excess of 19 kJ mol^{-1}. Although the authors did not describe the spectrum as bimodal, a single Maxwellian curve did not fit the data perfectly; the 1450 K curve fitted the slow tail reasonably but did not match the sharpness of the high-speed peak.

The most energetic CO_2 molecules have been produced using an atomic oxygen source. Mullins, Rettner and Auerbach[3] measured an average kinetic energy normal

to their 90 K Pt{111} sample of 0.6 ± 0.05 eV, an excess of some 56 kJ mol^{-1}. As thermalized oxygen adatoms would not react significantly at such low temperature, the reaction clearly occurs before the oxygen atoms accommodate to the surface.

2.2 Internal Energy

In addition to the excess energy partitioned into the translational motion of the CO_2 molecules produced in the oxidation reaction, further excess energy can be channelled into both vibrational and rotational degress of freedom. This can be detected experimentally by observing the infrared chemiluminescence spectrum of the CO_2 in the region in front of the crystal. These studies are almost all performed in steady-state conditions on Pt foils, limiting the results to relatively high surface temperatures such that the reaction is not poisoned by excessive CO coverage blocking oxygen adsorption. A compilation of the values measured in different studies is shown in Figure 1.

Brown and Bernasek[7] found a vibrational temperature of 1270 to 1060 K, decreasing with increasing oxygen coverage, for CO_2 desorbing from a Pt foil at 800 K. Coulston and Haller[10] found a Boltzmann temperature of ~ 1500 K for the vibrational energy of CO_2 molecules produced on a Pt foil held at 800 K.

Mantell, Kunimori and Haller have produced a series of publications concerning the internal excitation of CO_2 molecules produced on both Pt and Pd foils. On Pt, they found[6] an average vibrational temperature of 1500 K with a surface temperature of 730 K, but a rotational temperature of only 1050 K. With the surface at 900 K the vibrational and rotational temperatures increased to 1700 K and 1200 K respectively, and they also found significant differences between the Boltzmann temperatures of different vibrational modes at both surface temperatures. In addition to steady-state measurements, time-resolved data were collected[11] to obtain chemiluminescence spectra as a function of time during CO molecular beam pulses. As the oxygen coverage was substantially depleted during each pulse, information regarding the oxygen coverage dependence of the CO_2 internal state distribution was obtained;

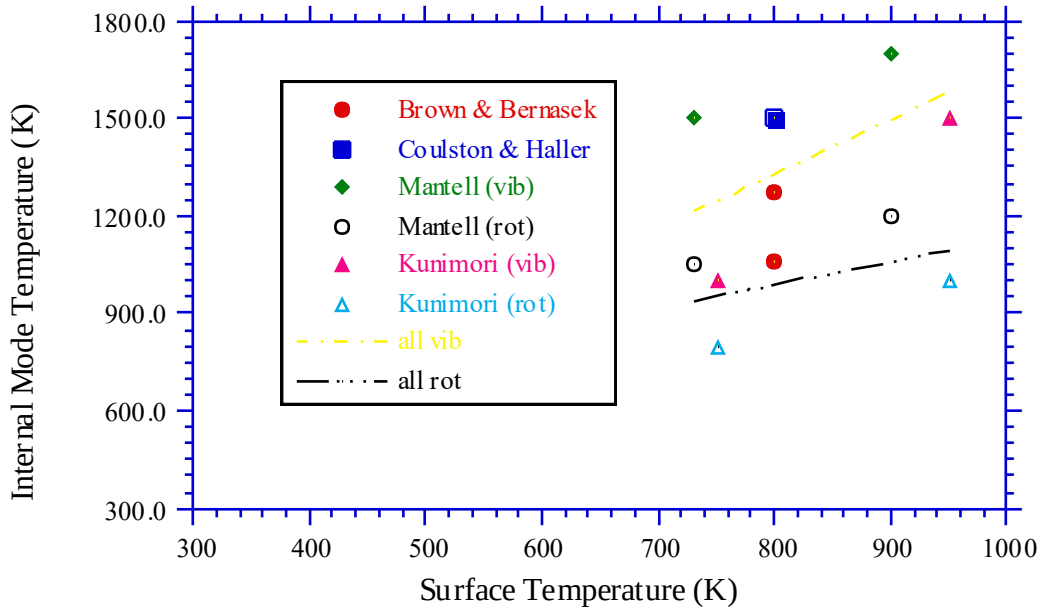

Figure 1. Vibrational and rotational Boltzmann temperatures of CO_2 molecules produced by CO + O_2 reaction on platinum foils.as measured by different groups.

they found a narrowing of the asymmetric stretch band with declining oxygen coverage, which was attributed to the removal of some excited component so indicating a smaller degree of vibrational excitation at lower oxygen coverages.

Kori and Halpern[12] performed the chemiluminescence experiment with a target of oxidised Pt, with which O atoms and CO molecules interact much more weakly than clean Pt. Using a continuous oxygen atom source they maintained the oxidation reaction at room temperature. They concluded that 250 kJ mol^{-1} was channelled into the asymmetric CO_2 stretch alone, with v = 11 the average level in that mode; in contrast, even the v = 1 level would be negligibly populated ($N_1/N_0 \sim 10^{-5}$) for a room-temperature molecule.

3 Results and Discussion

The coadsorption of CO and oxygen was investigated in two elementary ways: by first dosing pure oxygen and then adding pure CO, and *vice versa*.

3.1 Reaction of CO with Preadsorbed Oxygen

In Figure 2 the calorimetric results are shown for the addition of CO to the Pt{110} surface previously saturated with a molecular beam dose of oxygen equivalent to an ambient exposure of 100 L. The approximate saturation coverage of oxygen dosed at 300 K on Pt{110} has been estimated at 0.35 ML by quantitative XPS[13], though our results suggest that it could be closer to 0.5 ML. Coverages here are quoted relative to the ideal bulk-terminated surface, i.e. 1.0 ML + 9.22 ∞ 10^{14} molec cm^{-2}. The amount of CO_2 produced by the reaction could not be evaluated quantitatively, and so the "sticking probability" shown in Figure 2b determined via the King and Wells technique[14] is the sum of the reaction and adsorption probabilities for CO, while the coverage scale obtained is the number of monolayers of CO either reacted or adsorbed. Similarly the molar heat presented in Figure 2a is the heat deposited in the crystal per mole of CO which either reacts or adsorbs during the 50 ms adsorption pulse. The error bars indicate the standard error between five or more runs and so reflect the precision or reproducibility of the experimental results; additionally we would expect absolute uncertainties in calibrations of the order of 5-10%.

In preliminary experiments the adsorption heat of oxygen alone on the Pt{110} surface was calorimetrically determined (see Chapter 3). The heats of formation of CO_2 and CO in the gas phase are well known, and the expected heat of reaction can therefore be calculated assuming that all sticking molecules react. Should some CO adsorb and some react, we would expect to measure a heat intermediate between that expected for the reaction and that of simple adsorption, though the heat change for the latter process will in general be different from that on the clean surface.

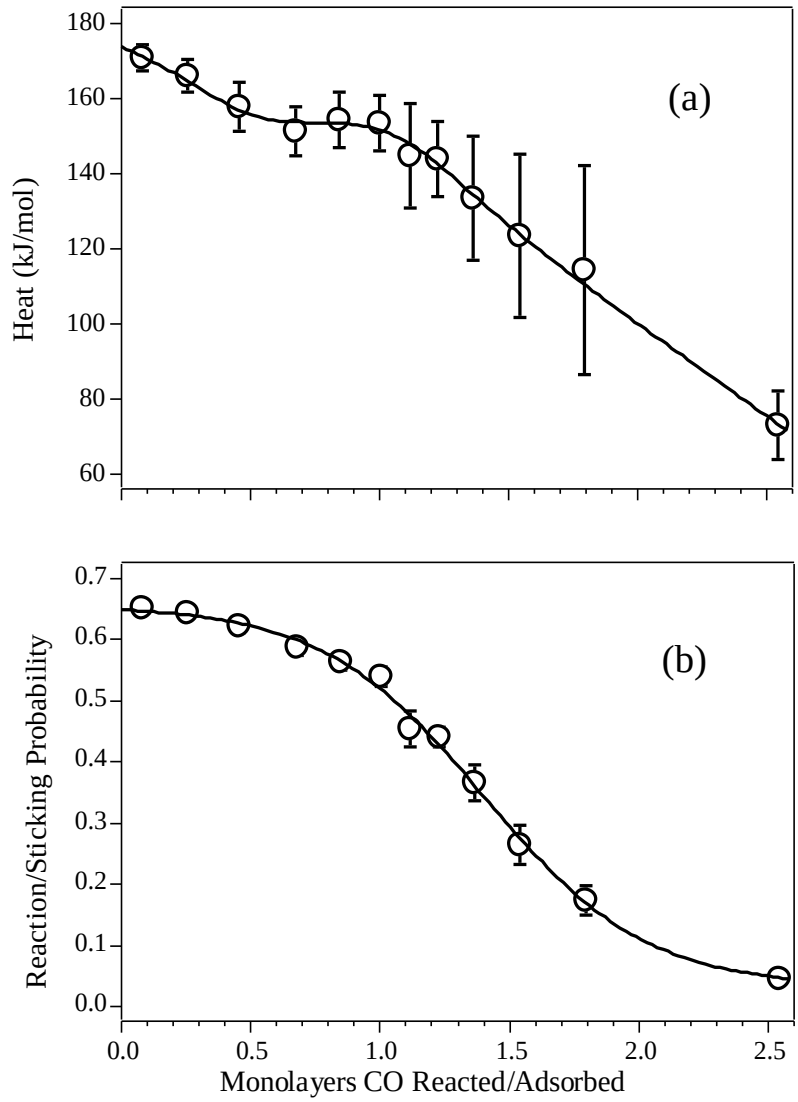

Figure 2. (a) Heat of reaction or adsorption and (b) probability of reaction or sticking for CO on an oxygen-saturated Pt{110} surface at 300 K. The lines represent smooth polynomial fits to the data.

Both the heat and sticking/reaction probability curves show the same general form as for the adsorption of CO on the clean surface. The molar heat for the interaction with O-predosed Pt{110} has an initial value of 171 ± 4 kJ mol^{-1}, falling only gradually to 155 kJ mol^{-1} at 0.5 ML and remaining constant up to 1 ML, before falling once more to approximately 120 kJ mol^{-1} at 1.8 ML. As the CO saturation coverage on the clean surface is only 0.9 ML it is clear that much of the CO must react with the preadsorbed oxygen and leave as CO_2 to give more free surface for adsorption. If all preadsorbed O reacts to form CO_2, we would expect 0.35 to 0.5 ML of CO to react and a further 0.9 ML to adsorb, giving a total of 1.25 - 1.4 ML. However, as the surface approaches saturation the usual steady-state situation is achieved in which the quantity of CO added during the molecular beam

pulse, for which we measure some finite sticking probability and adsorption heat, is exactly balanced by the quantity which desorbs between pulses. Summing our sticking contributions gives an apparent coverage scale which extends indefinitely while the true coverage reaches some definite limit.

We must note that even if complete reaction should occur, it is possible that the heat measured during the 50 ms beam pulse corresponds simply to CO adsorption and that reaction occurs on a longer timescale. In Figure 3, the partial pressure of CO_2 as a function of time is shown for the first seven pulses of CO directed at the oxygen overlayer in one particular experiment. The first CO_2 peak is sharp, and has the same decay constant (~ 250 ms) as seen for a molecular beam pulse of CO_2 reflected from the gold flag; the reaction is fast, and so the measured heat will correspond to the reaction. However, successive pulses become broader and smaller until only an increased background is seen; here the reaction is slow, and the measured heat will correspond mainly to adsorption of CO. This dramatic reduction in reaction rate with falling oxygen coverage has been previously measured in a study employing surface temperature modulation[15] and was attributed to a large rise in the activation energy with decreasing oxygen coverage.

The reaction is:

$$CO_{(g)} + O_{(Pt)} \varnothing CO2_{(g)},$$

and the heat of reaction which we would expect to measure, $\Delta_r H$, is thus given by:

$$\Delta_r H = \Delta_f H[CO_{2(g)}] - \Delta_f H[CO_{(g)}] - \Delta_f H[O_{(Pt)}].$$

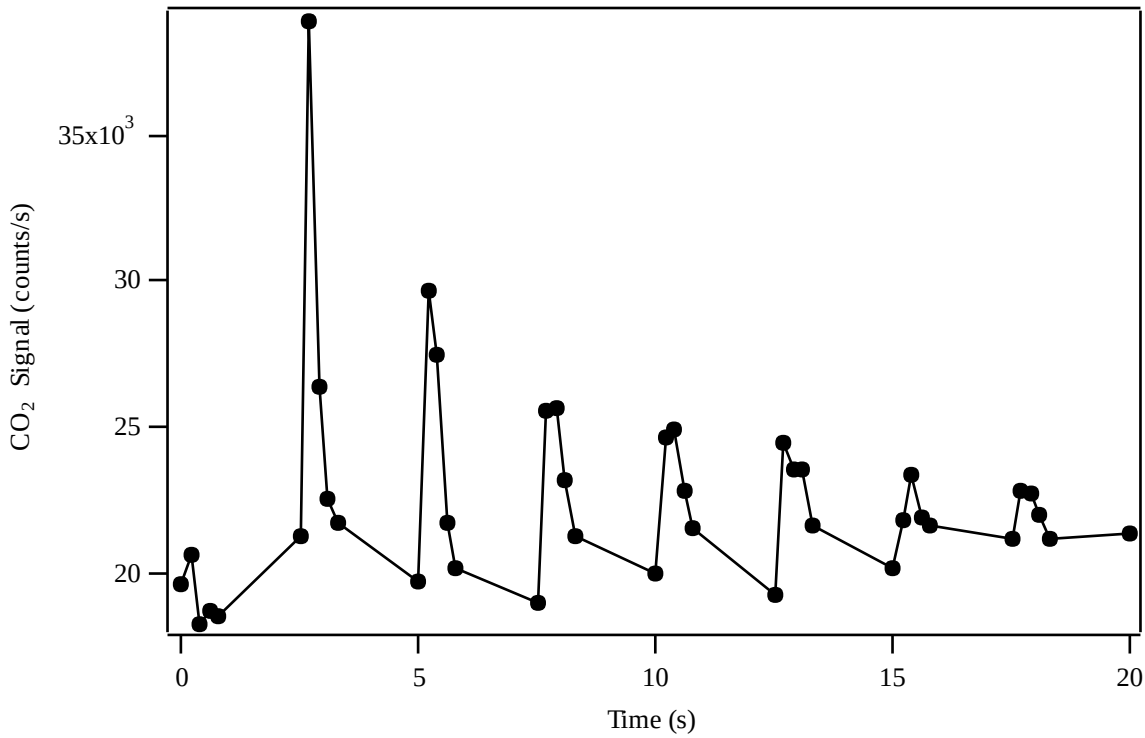

Figure 3. CO_2 partial pressure as a function of time as CO is pulsed onto oxygen-predosed surface. The first pulse is introduced at 2.5 s and the repetition period is 2.5 s.

The heats of formation ($\Delta_f H$) of gaseous CO_2 and CO at 298 K and 1 atm pressure are –393.5 and –110.5 kJ mol^{-1} respectively[16]; the enthalpy change due to expansion to low pressure, which is zero for an ideal gas, is ignored. Oxygen alone adsorbs with a heat ranging from 335 ± 10 kJ mol^{-1} at low coverage to 214 ± 24 kJ mol^{-1} at 0.35 ML and 199 ± 27 at 0.50 ML, between which coverages saturation should occur, giving an average value of $\Delta_f H[O_{(Pt)}]$ = –103 ± 16 kJ mol^{-1} retaining the maximum and minimum limits as the error bar. We thus calculate the expected heat for the initial reaction, in which the more weakly bound oxygen atoms are removed, to be $\Delta_r H$ = 180 ± 16 kJ mol^{-1}, and this is the quantity of heat that we would expect to measure calorimetrically should the CO_2 leave without excess internal or translational energy.

From Figure 2, the heat measured for the initial interaction of CO with the oxygen overlayer is 171 ± 4 kJ mol^{-1}, which is lower than expected for fully accommodated CO_2 production, and so the CO_2 molecules leave on average with 9 ± 17 kJ mol^{-1} of

excess energy. The error bar encompasses zero, indicating that fully accommodated CO_2 molecules might be formed, although the previous work detailed in Section 2.1 suggests that some excess energy is more likely. The figure of 9 kJ mol^{-1} is small compared with the 56 kJ mol^{-1} excess kinetic energy alone observed for the reaction of CO with atomic oxygen beams[3], but is in fair agreement with the time-of-flight analysis of a temperature programmed reaction study on Pt{110}, where an excess translational energy of 17 kJ mol^{-1} was measured[9]. However, as we measure the total excess energy removed, we must also take into account the excess energy partitioned into internal modes in comparing our results to previous work. Chemiluminescence experiments to determine vibrational and rotational excitation (which are of similar magnitude) have been performed only at surface temperatures of 730 K and above except on oxidised Pt. From Figure 1 we can see that the vibrational results from different groups[2,6,7,10] show considerable scatter, and there is little data from the more demanding experiment to extract rotational information, but it is clear that the degree of excitation increases with surface temperature. Back-extrapolating linearly to 300 K would suggest little excess vibrational energy (T_{vib} ~ 500 K or an excess of ~ 2.5 kJ mol^{-1}) and rotational energy (T_{rot} ~ 650 K or an excess of (350R) = 2.9 kJ mol^{-1}), whereas if the downward trend in internal excitation with surface temperature levels off a characteristic vibrational and rotational temperature of the order of 1250 K could be expected, equivalent to an excess energy of 40 kJ mol^{-1}. It is impossible to make a quantitative comparison but our measurement clearly shows only a modest degree of total excitation among the range of values that might be expected.

3.2 Reaction of Oxygen with Preadsorbed CO

It was found that the sticking probability of oxygen on a surface previously saturated with CO was too small to perform accurate heat measurements. Just 0.67 ML of CO, therefore, was predosed onto the surface prior to oxygen adsorption to study the reaction. The oxygen sticking probability was still only of the order of

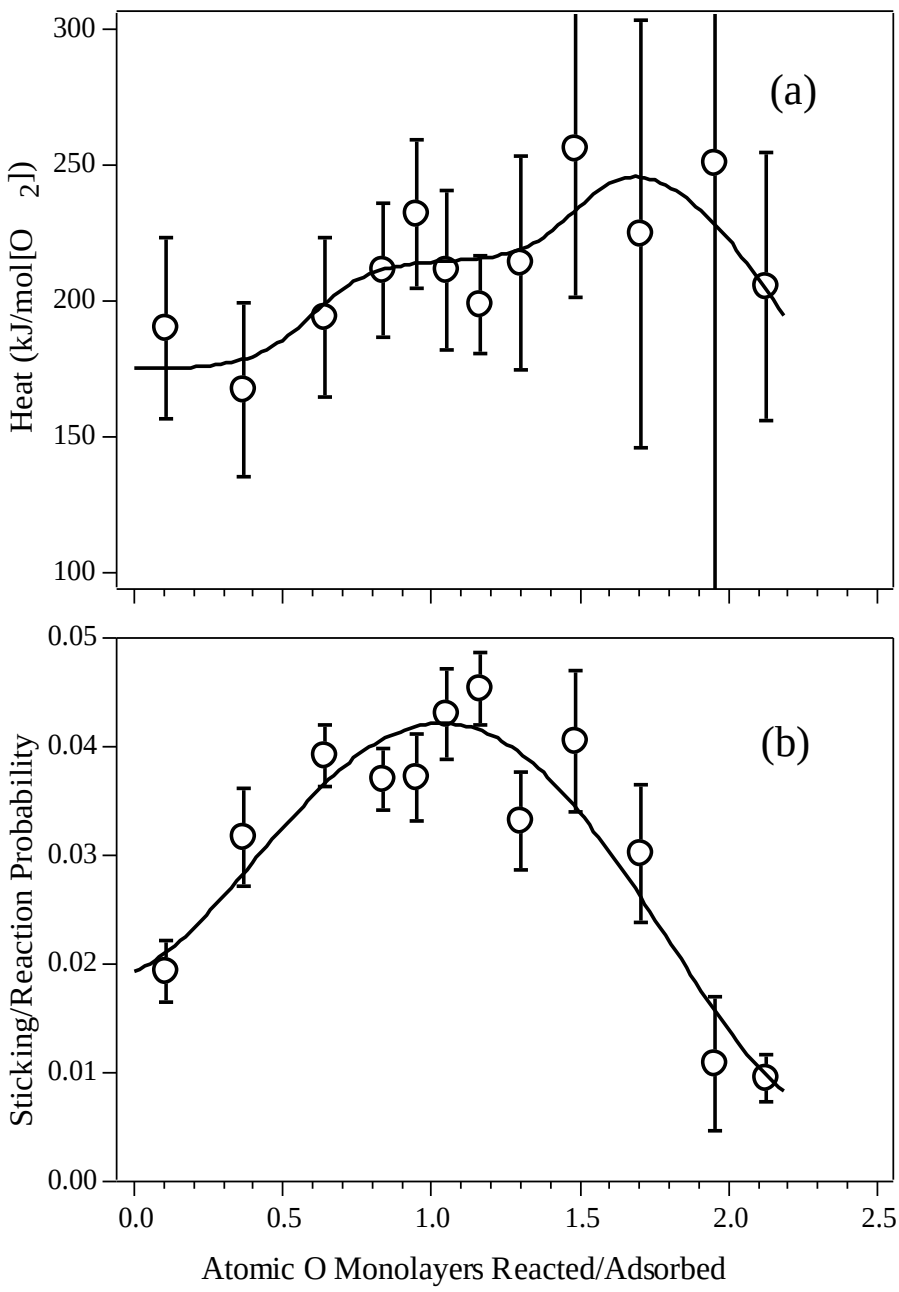

Figure 4. (a) Heat of reaction or adsorption (in terms of O_2) and (b) probability of reaction or sticking for oxygen on Pt{110} surface previously dosed with 0.67 ML CO at 300 K. The solid lines represent smooth analytical function fits to the data.

10^{-2}, giving rise to a larger scatter in the experimental data points than in the case of CO adsorption presented above because of the combined difficulties of measuring the very small sticking proability and very small quantity of heat.

As shown in Figure 4, the initial reaction heat measured per mole of oxygen molecules, averaged over the first 0.3 ML, is 185 ± 27 kJ mol^{-1}, gradually *increasing* with coverage to 250 kJ mol^{-1}. The sticking/reaction probability first increases with coverage, clearly indicating that reaction with CO produces fresh adsorption sites, and only after 1.5 ML of oxygen atoms have either adsorbed or

reacted does adsorption predominate and the sticking probability fall. Due to the large exposure of oxygen required each experimental run took ~ 2.5 h to complete, and inevitably some additional CO will have adsorbed (with a high sticking probability, see Figure 2b) from the residual gas mixture present at around $8 \infty 10^{-11}$ mbar in the vacuum chamber. This "topping up" of the CO coverage, of the order of 0.15 ML, will increase the amount of oxygen required to remove it and so extend our coverage scale. However, adding the CO predose, the extra CO dose from the background and our estimate for the saturation coverage of oxygen on the clean surface, a total O atom coverage of 0.67 + 0.15 + 0.5 = 1.32 ML at most would be expected to complete the reaction, which is signficantly less than the near 2 ML of oxygen that sticks or reacts as seen in Figure 4b. There is a possible explanation for this discrepancy: while the saturation coverage of oxygen dosed onto the (1 ∞ 2) surface at 300 K as measured[13] by XPS is 0.35 ML, that on the metastable (1 ∞ 1) surface is 0.8 ML at 250 K (above which temperature reconstruction to the (1 ∞ 2) occurs). Here the oxygen replaces CO which will have induced the (1 ∞ 2)∅(1 ∞ 1) reconstruction, and so it appears that oxygen adsorbs onto the (1 ∞ 1), achieving the higher coverage, more quickly than the surface reconstructs to the (1 ∞ 2).

We can again calculate the expected heat of reaction, given that the microcalorimetric adsorption heat of CO adsorption on the clean surface ranges from 178 ± 5 kJ mol^{-1} at 0.05 ML down to 146 ± 9 at 0.50 ML and 138 ± 17 kJ mol^{-1} at 0.67 ML.

$$O_{2(g)} + 2CO_{(Pt)} \varnothing 2CO_{2(g)}$$

$$\Delta_r H = 2 \,.\, \Delta_f H[CO_{2(g)}] - 2 \,.\, \Delta_f H[CO_{(Pt)}] - \Delta_f H[O_{2(g)}]$$

The heat of formation of oxygen gas is zero by convention and those of CO and CO_2 are as used above. For complete reaction to CO_2 at 300 K, an initial heat of 288 ± 34 kJ mol^{-1} would be expected compared to the 180 kJ mol^{-1} measured.

Assuming that initially the oxygen adsorption channel is negligible compared with the reaction channel, the difference amounts to 103 ± 43 kJ mol^{-1} per oxygen molecule or 52 ± 21 kJ mol^{-1} per CO_2 molecule produced. This is the lower limit for the excess energy carried away by the product CO_2 assuming that any oxygen simply adsorbing does so with a heat greater than 185 kJ mol^{-1}.

4 General Discussion

The CO_2 molecules produced when CO is added to an overlayer of oxygen show a much smaller degree of excitation (9 kJ mol^{-1}) than those produced, at the same surface temperature, when oxygen is added to a CO overlayer (52 kJ mol^{-1}). One reason for this could be the drop in the reaction activation energy with increasing oxygen coverage, with a concomitant reduction in the downward energy slope followed by the product; however, it has been suggested that the reduced activation energy at high oxygen coverages is due to the reduced binding energy of the reacting oxygen atoms rather than a less energetic transition state[15], and indeed our calorimetric measurements show a drop of some 150 kJ mol^{-1} in the oxygen adsorption heat as the O coverage increases from zero to 0.5 ML coverage.

A second explanation is that "hot" oxygen adatoms are formed in the dissociation process which react, before losing excess translational energy, with adsorbed CO molecules to form the more highly excited CO_2. Such hot adatoms have been implicated in the production of highly excited CO_2 molecules produced in the temperature-programmed CO oxidation reaction on Pt{111} at 130 K as O_2 dissociation occurs[4], while non-accommodated oxygen atoms have been shown to give rise to CO_2 molecules with greater internal excitation in the steady-state reaction on a Pt foil[2] and on Pt{111}[3] at 90 K. The bimodal angular and velocity distributions observed on Pt{111}[5] at 550 K in a steady-state reaction where CO and O_2 were dosed continously onto the surface might also be explained in these terms, the fast component being produced by hot oxygen atoms that react quickly after dissociation with pre-adsorbed CO molecules, and the slow component from oxygen

atoms which become accommodated to the surface and are later reacted off by diffusing CO. However, the same explanation cannot hold true for the bimodal distribution seen for a 330 K peak in a temperature-programmed reaction study[4] where no hot oxygen adatoms could be present.

In conclusion, we have directly measured for the first time the heat evolved by a catalytic reaction on a single crystal surface. We have reacted CO with O/Pt{110} and oxygen with CO/Pt{110}, in each case generating gaseous CO_2 as the product. Unexpectedly we find, from the difference between the measured heat deposited in the crystal with that expected, that in the former case the CO_2 molecules depart with only 9 ± 17 kJ mol^{-1} excess energy but in the latter case 52 ± 21 kJ mol^{-1} is removed. We suggest that the much greater degree of excitation in the second case could be due to the channelling of energy from the dissociation of the oxygen molecule to the product CO_2 via "hot" oxygen adatoms, which never thermally accommodate to the surface.

References

[1]C.A. Becker, J.P. Cowin, L. Wharton and D.J. Auerbach, J. Chem. Phys. **67** (1977) 3394.

[2]K. Kunimori, H. Uetsuka, T. Iwade, T. Watanabe and S. Ito, Surf. Sci. **283** (1993) 58.

[3]C.B. Mullins, C.T. Rettner and D.J. Auerbach, J. Chem. Phys. **95** (1991) 8649.

[4]K.-H. Allers, H. Pfnür, P. Feulner and D. Menzel, J. Chem. Phys. **100** (1994) 3985.

[5]E. Poehlmann, M. Schmitt, M. Hoinkes and H. Wilsch, Surf. Sci. **287** (1993) 269.

[6]D.A. Mantell, K. Kunimori, S.B. Ryali, G.L. Haller and J.B. Fenn, Surf. Sci. **172** (1986) 281.

[7]L.S. Brown and S.L. Bernasek, J. Cehm. Phys. **82** (1985) 2110.

[8]R.L. Palmer and J.N. Smith (Jnr.), J. Chem. Phys. **60** (1974) 1453.

[9]T. Matsushima, Y. Ohno and J. Murakami, Surf. Sci. **287** (1993) 192.

[10]G.W. Coulston and G.L. Haller, J. Chem. Phys. **95** (1991) 6932.

[11]D.A. Mantell, S.B. Ryali and G.L. Haller, Chem. Phys. Lett. **102** (1983) 37.

[12]M. Kori and B.L. Halpern, Chem. Phys. Lett. **110** (1984) 223.

[13]N. Freyer, M. Kiskinova, G. Pirug and H.P. Bonzel, Surf. Sci. **166** (1986) 206.

[14]D.A. King and M.G. Wells, Proc. R. Soc. London, Ser. A **339** (1974) 245.

[15]J.R. Engstrom and W.H. Weinberg, Surf. Sci. **201** (1988) 145.

[16]J.D. Cox, D.D. Wagman and V.A. Medvedev, *CODATA Key Values for Thermodynamics* (Hemisphere Publishing Corporation, New York 1989).

Chapter Five

Ethylene on Pt{110}

Abstract

The calorimetric heat of adsorption for a hydrocarbon on a single crystal surface has been measured for the first time. For ethylene on Pt{110}-(1 ∞ 2) at low coverages it is about 200 kJ mol^{-1} and drops in several steps to 120 kJ mol^{-1} with increasing coverage. We correlate these heat changes with three stable species previously assigned from vibrational spectroscopy and the average bond dissociation energy of a Pt–C single bond is extracted for each of them. The mean value is 231 kJ mol^{-1}, and we observe a systematic decrease from 249 kJ mol^{-1} to 217 kJ mol^{-1} as the number of single Pt–C bonds per adsorbate molecule increases from 2 to 4.

1 Introduction

Ethylene can be hydrogenated to ethane in the presence of Pt, a system which serves as a model for hydrogenation-dehydrogenation reactions in catalysis, and much effort has been spent in elucidating the various surface species formed as ethylene decomposes on Pt surfaces, with some success. Previous studies have shown that ethylene adsorbs reversibly on Pt at low temperatures but that it decomposes into various intermediates near room temperature or above[1][2][3][4]. Elaborate models of the catalytic pathways have been constructed[5] in order to deduce likely reaction mechanisms, yet the estimates of binding energies and activation barriers have had no experimental basis other than a single datum, namely the desorption energy of reversibly adsorbed ethylene which is 70 kJ mol^{-1} on Pt{111}[6]. Calorimetric measurements of the binding energy of various irreversibly adsorbed hydrocarbon species will therefore be of great value in generating more reliable reaction schemes.

The nature of these intermediates depends on the crystallographic orientation of the surface and the temperature of adsorption. On the (1 ∞ 2) Pt{110} surface Yagasaki *et al*[3] have found at least two different species at temperatures above 100 K. At 300 K

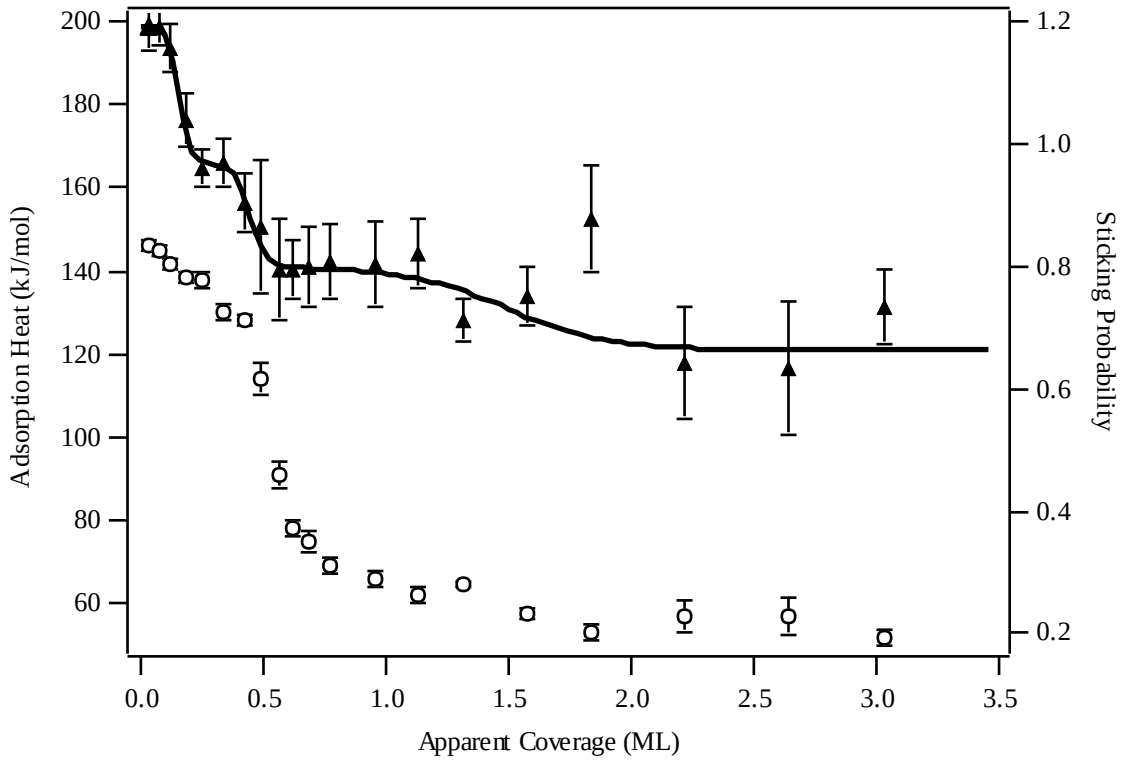

Figure 1. Heat of adsorption (filled triangles) and sticking probability (open circles) of ethylene on Pt{110}-(1 ∞ 2) at 300 K as a function of coverage. The solid line passing through the heat data is a smooth functional fit.

their EELS and TDS study indicates the presence of C_2H_2 and C_2H_3 which they attribute to ethylylidine and ethylidine (see Figure 3). Low exposures of ethylene produce mostly C_2H_2 species while at saturation there seems to be about twice as much C_2H_3 on the surface as C_2H_2. We should therefore expect to see changes in the ethylene adsorption heat as a function of coverage corresponding with these changes in decomposition products.

2 Results

2.1 Adsorption Heat

Figure 1 shows the coverage-dependent heat of adsorption of ethylene on Pt{110}. The statistical errors in the heat were obtained from 5 different experiments and are smaller than about 6%. However, the absolute values of the heats given depend on

the calibration of several physical quantities and we estimate the sum of these systematic errors to be smaller than 8%.

Initially the heat of adsorption is 200 kJ mol^{-1}. Between 0.1 and 0.2 ML the heat drops sharply to about 175 kJ mol^{-1} and then levels out briefly at 165 kJ mol^{-1}. A second drop to 140 kJ mol^{-1} occurs around 0.5 ML coverage. Between 0.6 and 1.2 ML apparent coverage the heat remains constant at about 140 kJ mol^{-1} and finally drops to approximately 120 kJ mol^{-1} at apparent coverages above 1.5 ML. At this point the usual steady-state situation is reached where as many molecules desorb between consecutive pulses as adsorb during each pulse. We were not able to detect any reaction products of ethylene that could be formed in this steady-state on the Pt surface. Coadsorption of deuterated ethylene with normal ethylene did not reveal any exchange of hydrogen atoms. It therefore seems that in the steady-state the ethylene molecules chemisorb on the surface without breaking up and then desorb slowly compared to the molecular pulse time.

2.2 Sticking Probability

The initial sticking probability is 0.83, falling approximately linearly to 0.7 at an apparent coverage of 0.42 ML before dropping abruptly to a value of 0.3 between 0.77 and 1.3 ML. A further small yet significant decline then occurs before a constant value of 0.22 is achieved in the steady-state regime above 1.5 ML.

2.3 LEED Measurements

The clean surface LEED pattern at 50 eV is shown in Figure 2a. In addition to the expected (1 ∞ 2) pattern, some additional streaking indicative of the presence of other (1 ∞ n) periodicities is present. This reflects the low annealing temperature of only ~ 600 K rather than the 1000 K or more required to obtain excellent order[7].

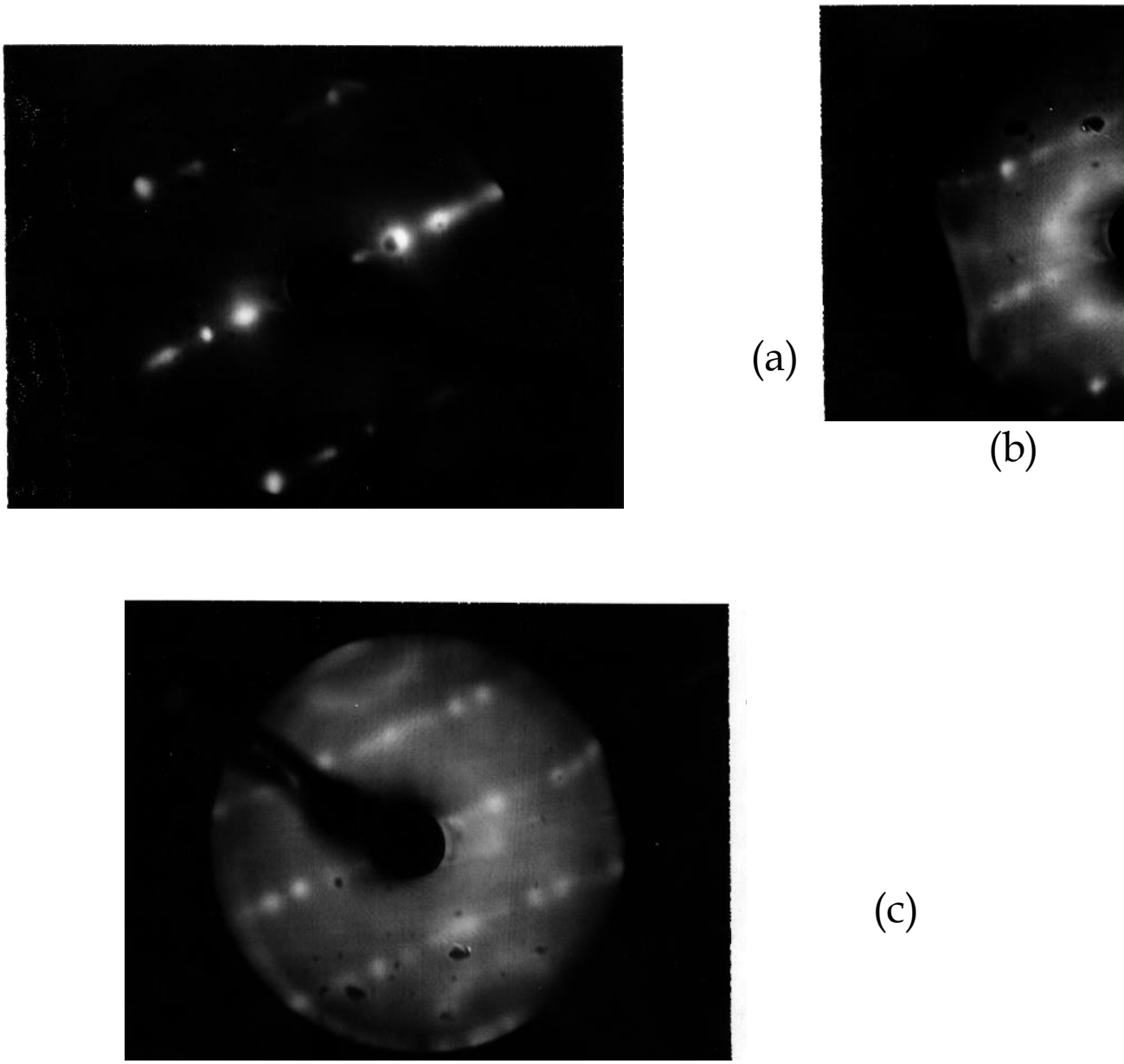

Figure 2. LEED patterns for Pt{110} at room temperature with and without adsorbed ethylene. (a) (1 ∞ 2) clean surface structure at 50 eV; (b) with 0.55 ML adsorbed ethylene at 83 eV, showing a ring of extra diffuse spots about the (0,0) beam; (c) the same at 107 eV, showing the ring also about the (±2,0) beams.

Adding ethylene to the surface at 300 K resulted in the formation of a ring-like pattern of diffuse spots arond the (0,0) beam and an increase in background intensity especially along the (1/2,x) regions. This pattern is shown in Figure 2b at 83 eV and Figure 2c at 107 eV with an ethylene coverage of around 0.55 ML; in the latter it can be seen that the ring appears around the (0,0) and (±2,0) beams but not around the (±1,0) beam. At a coverage of 0.1 ML, the ring was barely visible at 83 eV and no additional structure was seen at other energies; at 0.2 ML, the ring was

clearly present but less well resolved into distinct spots than in Figure 2b. At 0.55 ML, the ring pattern was observed between 77 and 95 eV and again at around 107 eV, as shown. We conclude that the (1 ∞ 2) reconstruction is not lifted by C_2H_4 adsorption under these conditions. These results are in contradiction with two previous studies, which in turn contradict each other: Yagasaki *et al*[3] reported an increase in background intensity upon ethylene adsorption but no extra spots, while Boronin *et al*[4] reported a (1 ∞ 2)∅(1 ∞ 1) conversion induced by the adsorbate at 300-370 K.

3 Discussion

Yagasaki *et al*[3] have investigated the adsorption of ethylene on Pt{110} with EELS and TDS. Their data indicate that at first ethylene decomposes only into ethylylidyne (+C–CH_2–, see also Figure 3) which bonds to the Pt surface in the troughs of the missing-row reconstruction. As is seen in Figure 1, the heat of adsorption for this process is about 200 kJ mol^{-1} at 0 ML decreasing to about 195 kJ mol^{-1} at 0.12 ML because of intermolecular repulsion and the simultaneous beginning of ethylidyne (+C–CH_3) formation. When all sites in the troughs of the (1 ∞ 2) reconstruction are filled, ethylene can no longer decompose into ethylylidyne, and the heat drops sharply between 0.1 and 0.2 ML. At this stage only ethylidyne is produced on the surface. This compound forms readily on Pt{111}, and it is therefore probable that it adsorbs on the (111) microfacets of the missing-row reconstruction on Pt{110}. As these facets become covered with ethylidyne, the heat of reaction drops from 175 kJ mol^{-1} at 0.2 ML coverage to 160 kJ mol^{-1} at 0.4 ML. At around 0.5 ML coverage most of the (111) microfacets are covered with ethylidyne, and a second sharp drop appears in the measured heat. From the saturation coverages of C_2H_2 and C_2H_3 (0.16 and 0.45 ML, taking the coverage at which the heat curve reaches the halfway point between plateaus) we calculate that on a completely covered surface there is about 2 times more C_2H_3 than C_2H_2. This is in excellent agreement with Yagasaki *et al*[3] who report a ratio of 2.3 : 1 at saturation.

Our LEED data show no change in surface structure with coverage coincident with these differing adsorbed species, but only an increase in intensity of the extra diffraction features.

Type of reaction	**Heat of reaction [kJ mol^{-1}]**
$H_2C{=}CH_2 + 4Pt \varnothing Pt_3C{-}CH_2{-}Pt + 2H_a$	200
$H_2C{=}CH_2 + 3Pt \varnothing Pt_3C{-}CH_3 + H_a$	165
$H_2C{=}CH_2 + 2Pt \varnothing Pt{-}H_2C{-}CH_2{-}Pt$	140
$H_2C{=}CH_2 + 1Pt \varnothing Pt(H_2C{=}CH_2)$	120

Table 1. Three different reactions of ethylene with Pt{110}-(1 ∞ 2) at 300 K. H_a designates hydrogen atoms adsorbed on the surface. Pt denotes asurface Pt atom. The assignment of the latter two heats to di-σ and π-bound ethylene is tentative.

Between an apparent coverage of 0.6 and 1.2 ML the heat of reaction remains constant at about 140 kJ mol^{-1} and finally reaches its steady-state value of about 120 kJ mol^{-1} above 1.5 ML apparent coverage. Since we could not detect any gaseous reaction products other than ethylene and the ethylene decomposition into C_2H_3 and C_2H_2 species is completed around 0.5 ML coverage, these two plateaus must correspond to the reversible adsorption of ethylene species on the surface (rather than decomposition and recombination). Two possibilities are di-σ ethylene and π-bound ethylene. In analogy to the Pt{111} surface where Steininger *et al*[8] have found di-σ ethylene and ethylidyne coexisting to temperatures up to 340 K, we tentatively suggest that between apparent coverages of 0.6 and 1.2 ML mostly di-σ ethylene is added to the surface, while at steady-state adsorption/desorption takes place through π-bound ethylene, presumably on the ridges of the missing-row reconstruction. Although Yagasaki *et al*[3]find di-σ ethylene only up to 280 K on Pt{110} their EELS spectra at 300 K are consistent with a small amount of di-σ ethylene on the surface (but not π-bound) and Boronin *et al*[4] report a small amount of C_2H_4 desorption around 450 K for Pt{110} saturated with ethylene at 320 K.

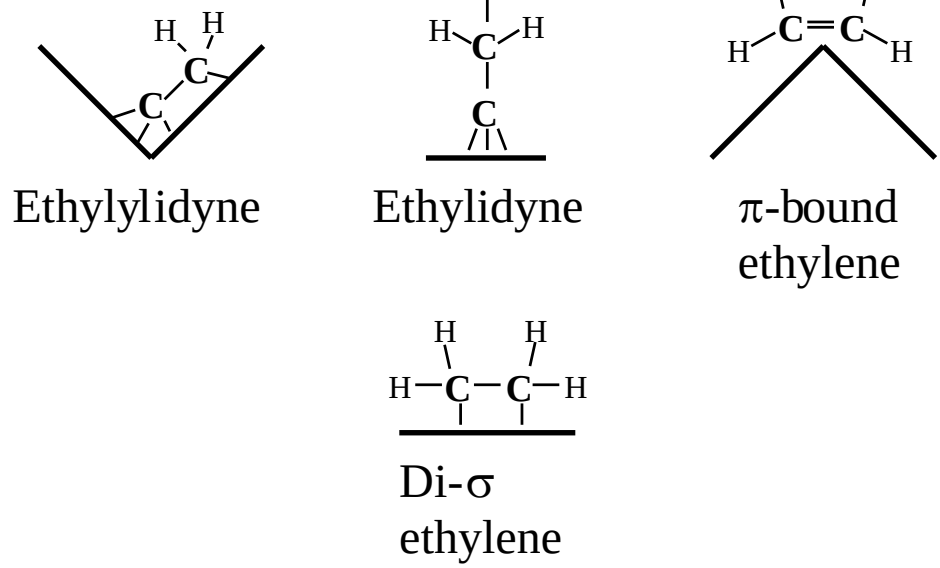

Figure 3. Schematic structures of ethylylidyne, ethylidyne and di-σ and π-bound ethylene.

Considering these coverage-dependent changes in adsorbed species, we see from the sticking curve in Figure 1 that the rate of uptake of ethylene is unperturbed by the transition from ethylylidyne to ethylidyne adsorption, but a dramatic change is seen once adsorption of those species saturates and the possible di-σ adsorption begins at 0.5 ML coverage. The small drop in sticking probability at around 1.5 ML apparent coverage correlates with the drop in adsorption heat at a similar coverage also.

The heats of adsorption of the four species on Pt{110} are summarized in Table 1. From them the average C–Pt bond dissociation energy for each species can be determined, as illustrated in the following example for the formation of ethylidyne in which a carbon atom forms single bonds to three Pt surface atoms.

1. $4Pt + H_2C{=}CH_{2(g)} \varnothing Pt_3C{-}CH_{3(a)} + Pt{-}H \qquad \Delta H_1 = -165 \text{ kJ mol}^{-1}$

Bond type	Number before	Number after	Net change	Bond dissociation energy (kJ mol^{-1})
C–C	0	1	1	376
C=C	1	0	–1	733
C–H	4	3	–1	412
Pt–H	0	1	1	256
Pt–C	0	3	3	x

ΔH_1 is obtained from the present work; we note that the microcalorimeter measures the heat released during the time period of a gas pulse, i.e. 50 ms, and the timescale at 300 K for H_2 desorption is significantly longer[9]. The measured heat therefore refers to step (1), with H atoms retained on the surface. The Pt–H bond dissociation energy is obtained from the heat of adsorption for H_2 on Pt{110}, determined from the desorption data of Engstrom *et al*[9] (75 kJ mol^{-1}) and the dissociation energy for H_2 (436 kJ mol^{-1})[10]. The C–H bond is the average bond dissociation energy while the C–C and C=C bond energies, which are somewhat larger for C_2 species than longer hydrocarbons, are that of ethane and ethylene respectively[11]. From the sum of these enthalpy changes, we get:

$$\Delta H_1 = -376 + 733 + 412 - 256 - 3x = -165$$

$$x = 226 \text{ kJ mol}^{-1}.$$

The C–Pt single bond dissociation energy for ethylidyne on Pt{110} is therefore estimated as 226 kJ mol^{-1}. We note that this procedure is approximate, as it is based on the use of average bond dissociation energies and the assumption that Pt–Pt and C–H bond energies are unaltered by adsorption.

The C–Pt single bond dissociation energies for ethylene and for ethylilydyne were obtained in the same way, and the results are summarized in Table 2. These results give a remarkably close agreement for all three species (all lie in the interval (232 ±

7%) kJ mol^{-1}), although the measured adsorption heats range from 200 to 140 kJ mol^{-1} and the number of bonds per adsorbed ethylinic species range from 4 to 2. This can be taken as some confirmation of the various structures suggested in Figure 3. The average C–Pt bond energy from this work therefore provides a unique experimental handle on estimates for adsorption heats for any hydrocarbon species not π-bonded to the surface[5]. It must be noted that there is a systematic variation in the C–Pt bond dissociation energy with the number of C–Pt bonds formed per ethylinic adsorbate molecule: 249 kJ mol^{-1} for two bonds, 226 kJ mol^{-1} for three bonds and 217 kJ mol^{-1} for four bonds. A linear extrapolation of these bond dissociation energies as a function of the number of bonds per molecule n indicates that a molecule bound with one single Pt–C bond to the Pt{110} surface should have a bond dissociation energy of about 263 kJ mol^{-1}. A value of 222 kJ mol^{-1} has been calculated[12] for the Pt–C bond in the discrete $Pt(CH_3)_2$ molecule using an *ab initio* method, and this was used as the Pt–C bond energy in the reaction schemes of Carter and Koel[5] for all σ-bonded species, in fortuitously good agreement with our average value of 231 kJ mol^{-1}.

Adsorbate on Pt surface	Number of Pt–C single bonds of the compound	Average Pt–C single bond dissociation energies [(kJ mol^{-1})/bond]
$Pt_3C–CH_2–Pt$	4	217
$Pt_3C–CH_3$	3	226
$Pt–H_2C–CH_2–Pt$	2	249

Table 2. Average bond dissociation energies of three different surface species on Pt{110} at 300 K.

4 Conclusions

In conclusion, the heat of adsorption of ethylene on Pt{110} at room temperature as a function of coverage clearly shows four different regimes which can be correlated with chemical changes on the surface. Initially mainly ethylylidine adsorbs

irreversibly on the surface. Between 0.1 and 0.2 ML a transition to the formation of ethylidyne occurs. At high exposures di-σ bound ethylene is probably formed before a steady-state situation is reached where ethylene adsorbs and desorbs reversibly.

From these data we were able to determine the average C–Pt bond dissociation energy for di-σ ethylene, $+C–CH_2–$ and $+C–CH_3$ on a single-crystal surface. This bond dissociation energy decreases systematically from 249 kJ mol^{-1} to 217 kJ mol^{-1} as the number of bonds per molecule increases from 2 to 4. Based on work of this kind, the formation of a database for average bond dissociation energies should finally enable us to quantitatively predict the behaviour of chemical reactions on single crystal surfaces.

References

[1]G.H. Hatzikos and R.I. Masel, Surf. Sci. **185** (1987) 479.

[2]M. Salmeron and G.A. Somorjai, J. Phys. Chem. **86** (1982) 341.

[3]E. Yagasaki, A.L. Backman and R.I. Masel, J. Phys. Chem. **94** (1990) 1066.

[4]A.I. Boronin, V.I. Bukhtiyarov, R. Kvon, V.V. Chesnokov and R.A. Buyanov, Surf. Sci. **258** (1991) 289.

[5]E.A. Carter and B.E. Koel, Surf. Sci. **226** (1990) 339.

[6]R.G. Windham, M.E. Bartram and B.E. Koel, J. Phys. Chem. **92** (1988) 2862.

[7]T. Gritsch, D. Coulman, R.J. Behm and G. Ertl, Surf. Sci. **257** (1991) 297.

[8]H. Steininger, H. Ibach and S. Lehwald, Surf. Sci. **117** (1982) 685.

[9]J.R. Engstrom, W. Tsai and W.H. Weinberg, J. Chem. Phys. **87** (1987) 3104.

[10]P. W. Atkins, *Physical Chemistry*, 3rd ed. (Oxford University Press, 1986).

[11]D.R. Lide (editor), *CRC Handbook of Chemistry and Physics*, 75th ed (CRC Press, Florida, 1994).

[12]J.J. Low and W.A. Goddard III, Organometallics **5** (1986) 609.

Chapter Six

Oxygen Chemisorption and Oxide Film Growth on Ni{100}, {110} and {111}: Sticking Probabilities and Microcalorimetric Adsorption Heats

Attribution

Sticking probability and adsorption heat measurements for oxygen on Ni{100}, {110}, and {111} are presented in this chapter, along with additional heat measurements for potassium-predosed surfaces. I obtained the data for all the {110} measurements and for those on {100} without potassium; the other data (including the fitting of the sticking curves) are due to N. Al-Sarraf and J.T.Stuckless[1], but are included here to make a coherent comparative discussion possible.

Abstract

The initial heats of adsorption of oxygen on Ni{100}, {110} and {111} are 550, 475 and 440 kJ (mol O_2)$^{-1}$ respectively, and the heat is found to drop rapidly with coverage in the chemisorption regime, indicating strong interadsorbate interactions. This rapid decline is not seen with coadsorbed potassium, however, a difference discussed both in terms of electron availability and coadsorbate attractions. The integral heats of adsorption for oxide film formation are 220, 290 and 320 kJ mol^{-1} respectively. Corresponding sticking probability measurements show initial values, all less than unity, of 0.63, 0.78 and just 0.23, again for the {100}, {110} and {111} surfaces in that order. The coverage dependence of the sticking probability is consistent in each case with a passivating oxide film four layers thick.

1 General Introduction

Industrially, nickel has been used for some time as a Fischer-Tropsch catalyst to synthesize methane from CO and H_2. More recently the abundance of natural gas as a feedstock has provoked interest in the oxidative coupling of methane to obtain

higher hydrocarbons. In particular NiO, suitably doped with alkali or alkali earth metal promoters, has been shown to be effective[2][3] in converting methane to ethane and ethylene. Academically, oxygen on nickel has provided a prototypical dissociative chemisorption system which has been subjected to a large number of surface science studies using a great range of techniques, many of which are referenced in the text below. The facile oxidation of nickel surfaces to form thin oxide films in UHV conditions has similarly provided a convenient model system as a metal oxide while retaining the conductive metal support, so allowing the use of experimental techniques that use or create charged particles without charging problems being encountered.

However, while many questions of structure and kinetics are now thoroughly answered, there is very little information pertaining to the energetics of either oxygen chemisorption or thin oxide film formation on nickel surfaces, because the adsorption is irreversible, in that heating leads not only to desorption but also to oxygen dissolution into the substrate. This means that adsorption energies cannot be estimated from TDS and equilibrium isosteres cannot be constructed (except for an oxygen-saturated substrate, which has been attempted[4]). Here for the first time calorimetric adsorption heats are presented for oxygen on all three low-index nickel surfaces, both for the initial chemisorption process and for the passivating oxidation, along with the corresponding sticking probability data. The results are divided into two sections: firstly the coverage-dependent sticking probability data, and then the corresponding adsorption heats.

2 Sticking Probability Data

2.1 Introduction

The sticking behaviour of oxygen on nickel has already been studied many times, usually by measuring the oxygen AES or XPS intensity as a function of exposure. This method often relies upon an uncalibrated ionisation gauge for the exposure measurements, and, in cases of high sticking probability, suffers from poor coverage

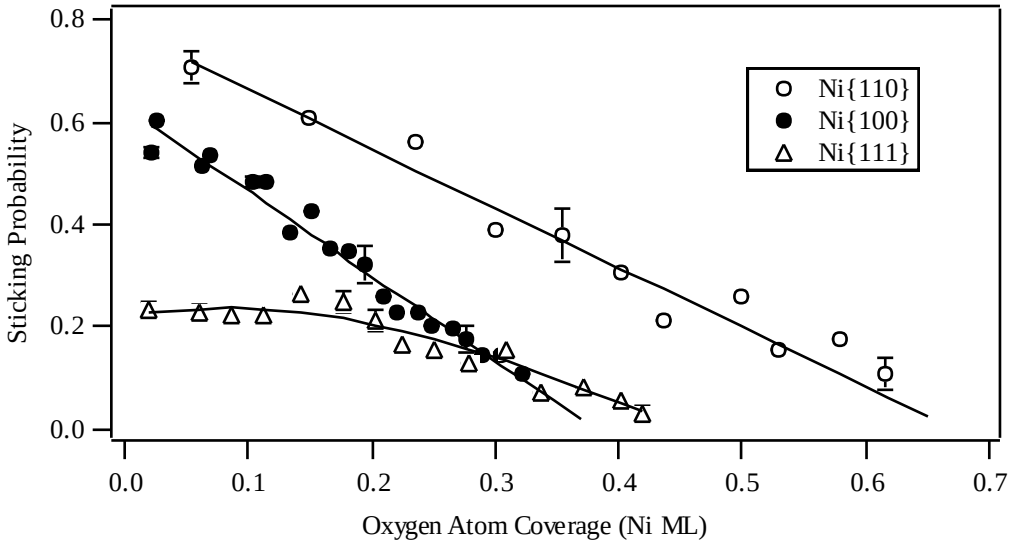

Figure 1. Oxygen sticking probability on Ni{100}, {110} and {111} at 300 K in the low-coverage region.

resolution. The technique which we use, similar to that devised by King and Wells[5], but adapted to a pulsed molecular beam, works especially well in cases of high sticking probability, and is performed with an absolute calibration of the gas dosing.

2.2 Sticking Probabilities in the Chemisorption Region

We start with an examination of the sticking probability in the low coverage chemisorption regime. Most previous studies have indicated that the three different low-index nickel surfaces show very similar behaviour, with an oxygen sticking probability which drops linearly with coverage from an initial value of close to 100%. Our measurements do reveal some substantial differences between the three surfaces, however, as shown in Figure 1.

Examining the most well studied of these systems, oxygen on Ni{100}, Holloway and Hudson[6] have reported that the sticking probability drops linearly with coverage from an initial value of 1.0 to an extrapolated chemisorption saturation coverage of 0.25 ML. A similar result, using XPS measurement of uptake rather than AES, was reported by Brundle *et al*[7], who find an initial sticking probability of 1.0

and a saturation coverage of 0.2 ML. Our data, seen in Figure 1, shows an extrapolated saturation coverage of 0.38 ML and a substantially lower initial sticking probability of 0.63. The saturation coverage appears inconsisent with the previous work cited above; however, Holloway and Hudson assume an initial sticking probability of unity and use that value to calibrate their coverage scale; they would have found a saturation coverage not of 0.25 but of 0.4 ML using our value for the initial sticking probability, while Brundle would have found 0.33 ML following the same procedure. These adjusted values then neatly bracket our extrapolated saturation coverage of 0.38 ML.

The ideal c(2 ∞ 2) structure should saturate at 0.5 ML, but a demanding empty site array requirement for dissociation probably prevents completion of the chemisorption structure. A Monte Carlo simulation of the sticking data by Brundle *et al*[8] indicates that an array of 8 adjacent empty atomic adsorption sites is necessary for sticking. That simulation also yielded interaction energies for the oxygen atoms, as fit parameters which determine the amount of order in an adlayer of adatoms which are assumed mobile. However, the disorder at room temperature is probably kinetic in origin rather then thermodynamic, since ordering actually increases with heating[9] and at room temperature the p(2 ∞ 2) phase, which is thermodynamically preferred for coverages up to 0.25 ML, is not detected by LEED[9]. This is in keeping with the very low adatom mobility at room temperaure observed in STM experiments[10]. The energies obtained in the Monte Carlo fit were necessarily around kT in magnitude, but our calorimetric data, to be discussed later, indicates that the adatom repulsions are in fact very much larger than this.

Considering next the {110} surface, Rieder[11], using AES to monitor oxygen uptake, finds that the sticking drops linearly with coverage from an initial sticking probability assumed to be 1.0 to an extrapolated saturation coverage of 0.55 ML, obtained using that assumed sticking. In contrast, Winkler *et al*[12], using a quartz crystal microbalance to monitor uptake, and with an exposure scale independently calibrated against a spinning rotor gauge, found that the sticking probability had a

constant value of 0.88 out to about 0.2 ML coverage, before falling towards zero at 0.5 ML coverage. Our data, shown in Figure 1, more closely resembles that of Rieder, as the sticking drops linearly with coverage, with an initial sticking of 0.78 and a saturation coverage of 0.67 ML. Using our initial sticking probability Rieder would have obtained an extrapolated saturation coverage of 0.7 ML, in good agreement with our results. We note that there is an example of oxygen sticking on Ni{110} which uses a reflection-detection technique similar to our own, by Sau and Hudson[13], and significantly, their initial sticking probability is almost identical to ours although they report an extrapolated saturation coverage of only 0.48 ML (but do not explain how this value was obtained).

The simplest interpretation of the linear fall in sticking probability with coverage on Ni{110} is that it is due to the ordered filling of a chemisorption overlayer saturating at 0.67 ML, and that further dissociative adsorption is precluded on this structure. Indeed, a weak $(3 \infty 1)$ LEED pattern is observed at room temperature[11] which corresponds to the coverage of 0.64 ± 0.06 ML reported using nuclear reaction analysis (NRA)[14], in close correspondence to our saturation value of 0.67 ML. It must be noted, though, that as with the previous system there is substantial disorder kinetically frozen into the room temperature structure; the LEED pattern sharpens after annealing[14], and the surface is reconstructed by oxygen adsorption[47].

Finally, AES measurements of oxygen uptake on Ni{111}, as reported by Holloway and Hudson[15] and by Rieder[11], indicate that the sticking probability drops linearly with coverage from an initial value assumed to be 1.0 to an extrapolated saturation coverage near 0.33 ML. However Winkler *et al*[12] report that the initial sticking probability is only 0.12, and that it actually increases with coverage to a value of 0.24 at 0.2 ML, before decreasing towards zero at a saturation coverage of 0.33 ML. Our result (Figure 1) this time more closely reproduces that of Winkler *et al*. The initial sticking probability is low, 0.23, and perhaps rises slightly as the coverage increases to 0.16 ML. Although the data is better fitted to the modified Kisliuk equation of Winkler and Rendulic[16] than to the classical Kisliuk equation[17], the

sticking curve is similar in shape to that usually found for precursor mediated adsorption kinetics, the amount of any rise in the sticking probability with coverage being near the limit of uncertainty of our measurements. The result obtained here is quite different from that reported by Rieder[11], or by Holloway and Hudson[15]. It must be stressed that in those works the initial sticking probability is actually only *assumed* to be unity, in effect as a calibration of the exposure scale. Also, their coverage resolution during the rapid initial gas uptake might not have been fine enough to reveal the initial sticking plateau. The first two data points shown by Holloway and Hudson for sticking at room temperature are at 0.1 and 0.2 ML, and we too would report a monotonic decrease using such coarse coverage increments.

Most experiments agree that oxygen chemisorption on Ni{111} is saturated at a coverage of about 0.33 ML, which corresponds to completion of the $\sqrt{3} \times \sqrt{3}$ R30° structure seen in LEED at temperatures near and below 300 K. Our curve extrapolates to a slightly higher coverage of about 0.45 ML, although as we shall discuss shortly part of this sticking may be attributed not to simple chemisorption but the initiation of oxidation. Our data shows that the sticking probability remains almost constant with early increases in the coverage, implying that the impinging molecule can sample multiple sites before desorbing or dissociating. The molecule is in an adsorption "precursor" state while doing this site sampling, and this precursor effect is convoluted with and obscures the dissociation site availability at a given coverage.

Our data clearly shows differences in the sticking probability between the three low-index surfaces. One apparent correlation is that the initial sticking is higher for less dense, or less smooth, nickel planes. Also, the precursor effect is most apparent where the surface is most closely packed. This is the same behaviour seen[18] on the most directly comparable oxygen / transition metal system, namely dissociative chemisorption on tungsten surfaces at room temperature. On the close packed bcc {110} plane the initial sticking is 0.45, or less[19], and does not decrease significantly until beyond 30% saturation coverage. On the less dense W{100} face the initial

sticking is higher, near unity, and drops more quickly with coverage, and at higher temperatures the initial sticking is about 0.8, and shows an almost linear decrease with coverage.

In the classic Kisliuk picture one can explain the correlation between the initial sticking and the sticking behaviour as a function of coverage by assuming that the attractive precursor potential on the more closely packed surfaces is smoother, with less deep wells. There is then increased precursor desorption, even over empty sites, but precursor diffusion is also increased, so that it can sample more sites even with this shorter lifetime. Alternatively, within the framework of a dynamic, or "hot" precursor model, we could assume that energy accomodation is more difficult on the smooth surface, so that the initial sticking is low, and that oxygen coverage, while blocking sites, helps increase the efficiency of relaxation into a dissociative state of either the molecule impinging directly from the gas state, or of a hot precursor skidding along the surface.

2.3 Sticking Probabilities in the Thin Oxide Film Regime

So far we have only discussed the chemisorption at low exposures. As the exposure increases the sticking does not actually reach zero at the extrapolated saturation coverage; instead, higher density chemisorption or oxide structures form. After this initial rapid chemisorptive uptake the sticking probability remains relatively low for some time. The exposure range of this latency period is very sensitive to conditions of temperature and of nickel surface order. Commencement of oxidation is indicated by a Ni^{2+} XPS signature, or, and perhaps more sensitively, by an increase in the sticking probability. Only a few layers of oxide form on the nickel surface during this period of rapid uptake, and further tarnishing occurs very slowly at 300 K or more rapidly at elevated temperatures and pressures. In their classic paper, Holloway and Hudson[6] model nickel oxidation as starting at nucleation points on the surface, and proceeding by the lateral growth of oxide islands of fixed thickness. Since oxygen incorporation only occurs at the island edges, and this is the rate

limiting step, the uptake rate increases initially with the increase in island size. As they get larger, however, and start to merge, the total perimeter edge length eventually decreases. The uptake rate then falls, until a continuous passivating oxide layer is formed, at which point the sticking probability approaches zero. This mechanism should lead to a bump in the sticking probability versus coverage, as indeed can be seen in Figure 2 showing the oxygen uptake on Ni{100} at room temperature.

Empirically this model, with oxygen uptake varying with island perimeter rather than area, provides a reasonable fit to our sticking data, but we might ask why this should be so. Holloway and Hudson decide that the reaction rate is limited either by surface diffusion or by some combination of surface diffusion and incorporation of oxygen into the oxide. However, there may be another explanation, based on two STM studies. We have already noted that Kopatzki and Behm[10] found that the spontaneous adatom hopping rate at room temperature was extremely low (~ 1 hr^{-1}), which suggests that diffusion across the chemisorbed layer cannot efficiently feed oxide island growth. Additionally a micrograph of Bäumer *et al*[20] showing oxide islands growing into the chemisorbed adlayer appears to show no adatoms immediately surrounding each island. We suggest that adatoms close to the oxide are "pulled in" and incorporated into it, or alternatively migrate sub-surface to extend it, to leave a thin strip of empty sites around each island, providing fresh clean surface for adsorption with a high local sticking probability. The adsorption rate will then be limited by the area of these perimeter strips, giving rise to the observed uptake kinetics. This would imply, however, that the local diffusion barrier for an adatom adjacent to a growing island being incorporated into it is considerably smaller than the diffusion barrier elsewhere; certainly the lattice at the edge of an oxide island suffers great distortion, so it is not unreasonable that an adatom sees a quite different potential energy surface there. Alternatively, Chakraborty *et al*[21] discuss how the activation energy for subsurface oxygen incorporation can be greatly reduced *dynamically* by lattice imperfections (such as

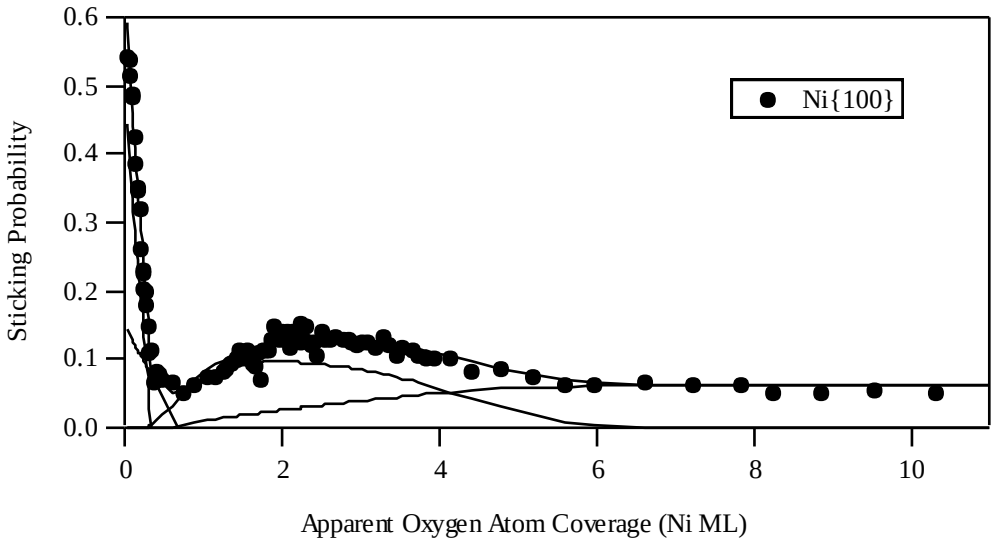

Figure 2. Oxygen sticking probability on Ni{100} at 300 K including the chemisorption, oxidation and reversible regimes. The smooth line running through the experimental data is the sum of the other fit lines including two straight lines as an empirical fit to the chemisorption sticking, a peaked curve corresponding to oxidation by island growth, and a dependent curve corresponding to reversible adsorption.

adjacent existing oxide) modifying local lattice vibrations favourably in a phonon-assisted rate process.

There is an anomalous feature of Figure 2 which we must address, namely that the observed sticking probability never drops to zero, even as the apparent oxygen coverage becomes very high. Once again this sticking is due to the reversible adsorption, here of molecular oxygen on the oxide surface, leading to a steady state population which increases with net adsorption during the gas pulse, and decreases with net desorption between gas pulses. Our experiment only measures the net uptake during the pulse, while the slow desorption between pulses is not monitored, and so the coverage obtained by summation of the sticking contributions appears to be increasing in this steady state regime. The reversible adsorption of molecular oxygen on oxidized nickel surfaces has recently been studied by Norton *et al*[22]. For conditions not too dissimilar to our own, a temperature of 325 K and dosing at $1 \propto 10^{-7}$ torr, they find an equilibrium oxygen coverage of 0.013 ML. We observe that the desorption rate at steady state (equal to the time averaged *adsorption*

rate) is $1.2 \propto 10^{-3}$ ML s^{-1}. When we discuss the calorimetric heats below, this data can be used to determine the desorption frequency factor or entropy of the adsorbed molecules, as described in Chapter 3 for CO and NO on Pt{110}.

Returning to Figure 2, we would like to fit an analytical function to the data describing the rate of oxidation as a function of coverage. Uptake curves have been analysed several times[11][23][24] after Holloway and Hudson using the island growth model described above, fitting the oxygen coverage to

$$\theta = \theta_{ad} + \Delta\theta_{oxide} \qquad (1)$$

where θ_{ad} is the coverage due to the chemisorption adlayer, and $\Delta\theta_{oxide}$ is the increase in coverage due to the oxide. For island growth in two dimensions, from islands of fixed thickness, the latter function is

$$\Delta\theta_{oxide} = (\theta_{satn} - \theta_{ad})(1 - \exp[-K_i N_0 (L - L_0)^2]) \qquad (2)$$

where θ_{satn} is the saturation oxygen coverage, L is the oxygen dosage, conveniently expresed in Langmuirs, and L_0 is the exposure at which oxide nucleation is initiated. For an ideal "extended" surface, where islands do not overlap or compete for admolecules, the sticking is a quadratic function of coverage with a proportionality constant equal to $K_i N_0$. This parameter is determined by the probability that a molecule at or near an island edge site will react, and the probability at a given coverage of the molecule actually meeting such a site, which depends upon the number of islands per unit area, N_0, and also upon any ability of the molecule to sample multiple sites.

Differentiating Equation 1 for coverage, with respect to exposure, yields the sticking probability as a function of coverage, which we fit to our data. This fit must include an additional term for sticking due to transient adsorption of molecular oxygen on the oxide islands. In keeping with the model of lateral oxide island growth of fixed thickness we use

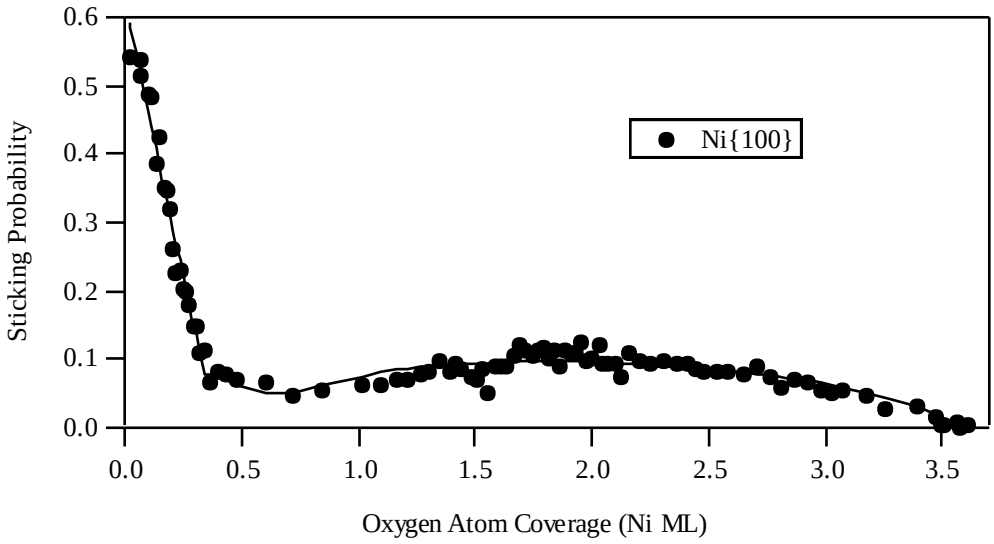

Figure 3. Oxygen sticking probability on Ni{100} at 300 K, now with the reversible contribution subtracted out to give a net sticking probability and absolute coverage scale.

$$s_{rev} = (\theta_{oxide} / \theta_{satn})\, s_{satn} \qquad (3)$$

where s_{satn} is the sticking probability at saturation, or steady state.

Figure 2 shows the best fit obtained to our data for oxidation of the Ni{100} surface. Once the amount of reversible or transient adsorption has been determined as a fitting parameter, then the apparent coverage and sticking probability can be corrected to yield net sticking and coverage, as shown for Ni{100} in Figure 3. We should mention that the calorimetric data will also be adjusted to take into account this transient adsorption on the oxide, so as to yield the net heat of *oxidation* versus the real coverage. The oxygen sticking results for the {111} and {110} surfaces are shown in Figures 4 and 5, and the extracted fit parameters for the oxidation are given in Table 2.

The fits to equations (2) and (3) were optimised for the higher exposure region where oxidation has already commenced, and dominates the sticking. At intermediate exposures the situation is more complex, as mixed chemisorption is occurring, and also the oxide islands are nucleating, perhaps via oxygen atom penetration below the nickel surface layer[21]. This process might be very dependent

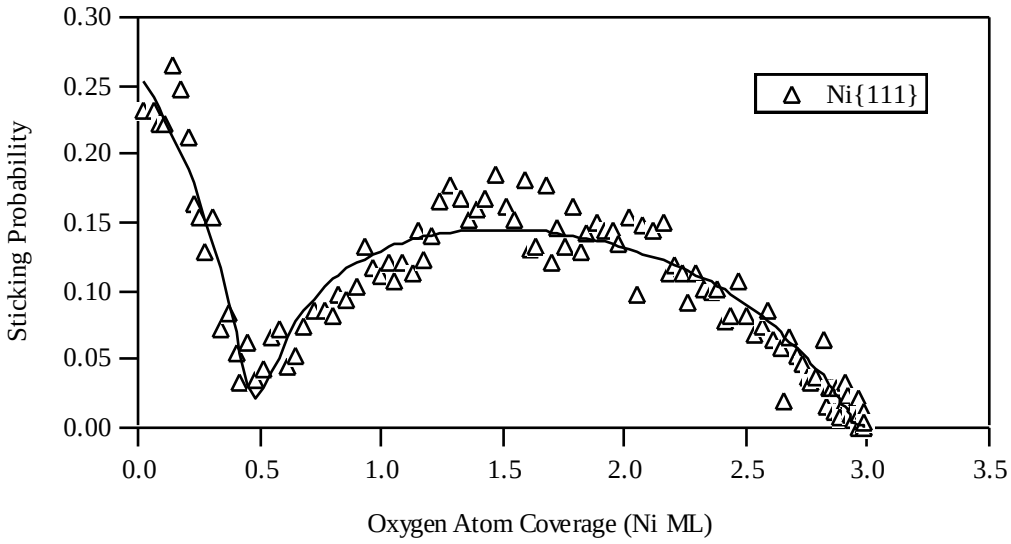

Figure 4. Oxygen sticking probability on Ni{111} at 300 K, now with the reversible contribution subtracted out to give a net sticking probability and absolute coverage scale.

upon the defect concentration of the substrate[25][20] or of the chemisorption adlayer[7]. We have not attempted to develop a model which would allow us to extract meaningful fit parameters describing the sticking in this region. With reference to Figure 2 for instance, the chemisorption region was fitted by the sum of two straight lines, but we consider this only an empirical fit. We will, however, extract an oxide initiation coverage, simply as the point at which the sticking starts to increase, and this is given in Table 2.

For the Ni{111} surface the sticking probability increases after about 0.45 ML, which is somewhat larger than the 0.33 ML found in the literature[7]. For Ni{100} the sticking rises at 0.68 ML, which is higher than the coverage where oxide nucleation is usually thought to begin[7], but in reasonable agreement with Pope *et al*[26] who quote a coverage of 0.57 ± 0.05 ML for the approximate point where oxygen uptake begins to accelerate, and point out that the rise in sticking might correspond to oxygen atom penetration of the surface before charge transfer or oxidation actually commences. For Ni{110}, our sticking behavior seems somewhat erratic, reaching a minimum at 0.9 ML, perhaps rising, then falling again to a minimum at 1.2 ML. This

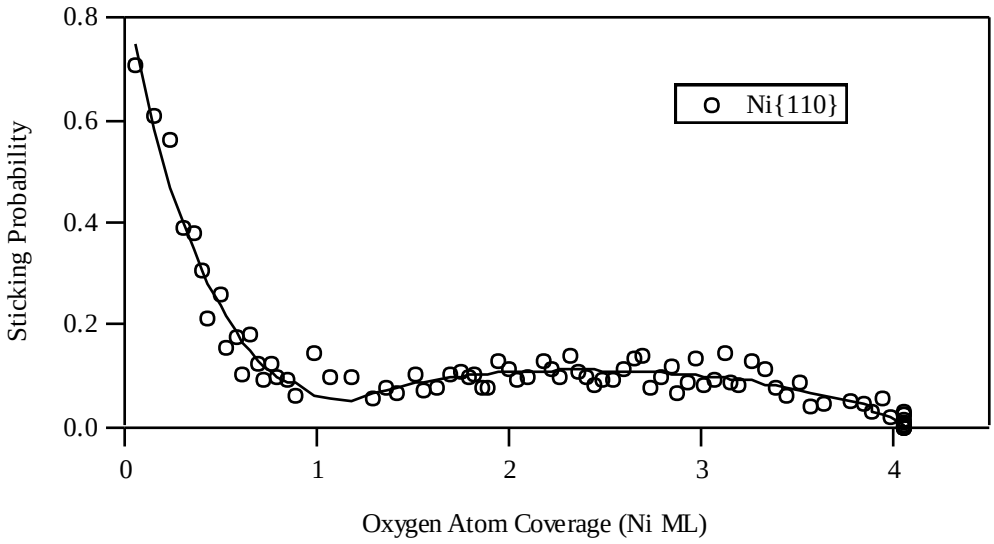

Figure 5. Oxygen sticking probability on Ni{110} at 300 K, now with the reversible contribution subtracted out to give a net sticking probability and absolute coverage scale.

behaviour may be associated with the $(9 \infty 4)$ "pseudo oxide" structure seen at ~ 1 ML coverage by Masuda *et al*[27] and others[28][24].

Another parameter of great interest is the passivation coverage, i.e. the amount of oxide created in each case. Here the net oxygen uptake is measured, but the thickness of the oxide layer depends upon its composition, structure and orientation. The simplest interpretation, which we shall follow, is that the thin film has the same composition and structure as the bulk NiO, an NaCl-type structure. The lattice parameters, compared to that of Ni substrate, can be found in ref. [29]. The lattice parameters may be perturbed from those of the bulk oxide, due to epitaxy with the nickel substrate, and that the oxide is probably highly defective in most cases, with many vacancy type defects where the islands coalesce, and also stoichiometric defects[30], like the oxygen rich Ni_2O_3 surface of bulk NiO samples. The following film thicknesses from the present study and from the literature are summarised in Table 1.

For NiO grown on Ni{111} at room temperature the oxide is reported[31] to be oriented predominantly with the {111} face parallel to the substrate, though the LEED pattern is often weak[11][15]. This is epitaxial growth in terms of symmetry,

but the lattice match is poor, with the oxide Ni^{2+} ions about 30% further apart then the substrate Ni atoms. The {111} orientation has alternate layers of oxygen and nickel ions parallel to the surface, and could be formed by oxygen place exchange with nickel atoms, with relatively little correlated atomic motion. At higher temperatures, however, above 500 K, the NiO{100} orientation dominates[31]. This should be thermodynamially more favourable due to the high electrostatic surface excess energy of the {111} face of NaCl type crystal structures[32].

	Reference	Oxide Layers	
		if {100}	if {111}
Ni{111}	present work		4.2
	[29]		3.4
	[11]		3
	[15]		2
	[33]		3
Ni{100}	present work	5.1	4.2
	[30]	3.7	3.1
	[34]	3.7	5.1
	[6]	2	
	[26]	3.4	
	[35]	4.7	
	[20]	4.5	
Ni{110}	present work	4.1	
	[14]	3.0	
	[11]	2	
	[35]	2.4	

Table 1. Passivating oxide film thickness on Ni{111}, {100} and {110}.

The saturation oxygen coverage on Ni{111} measured here is 3.0 ML, an integrated area density of $5.6 \infty 10^{15}$ atom cm^{-2}. Considering the oxygen atom density in the {111} plane of NiO this corresponds to 4.2 layers of the oxide as the passivating thickness. Our result is in reasonable agreement with that of Norton *et al*[29] who find $(4.5 \pm 0.5) \infty 10^{15}$ atom cm^{-2}, but supports four layers of oxide as the passivating thickness rather than Norton's three layers, which were also reported by Rieder[11]. Conversely, Holloway and Hudson[15] report that passivation occurs with a thickness of two {111} layers, while Narusawa *et al*[33] report a three layer amorphous oxide.

Just as for the Ni{111} surface, oxide growth on the Ni{100} surface occurs most easily for a NiO{111} orientation, with a more thermodynamically favourable NiO{100} able to form at higher temperatures[36]. For this system, however, the cross-over point between the two oxides is near room temperature, and the oxidation process around 300 K is very sensitive to temperature. In fact the room temperature oxide has been reported[34][35] as composed of mixed {100} and {111} crystallites. Our saturation oxygen coverage is 3.55 ML, an integrated area density of $5.75 \infty 10^{15}$ atom cm^{-2}, a larger value than the 2.6 ML reported by Carley *et al*[30] and Hall *et al*[34]. This would correspond to 5.1 layers of NiO{100} or to 4.2 layers of NiO{111}. Values in the literaure, ranging from 2 layers[6], through 3.4 layers[26], to 4.7 layers[35], are mainly derived from AES or XPS measurements, and are dependent upon an analysis of electron attenuation by the overlayer. Saiki *et al*[35], for instance, outline a very careful treatment of their XPS data, but their analysis depends upon the assumption that the oxide has a {100} orientation. Since this has a smaller density of O emitters per layer, and the layers are further apart, which they suppose leads to greater attenuation per layer, a larger saturation coverage is calculated than if the same signal were due to a {111} oxide layering. This might help explain why they report an oxygen saturation coverage which is significantly larger than that which has usually been reported (although in good agreement with our

result). Bäumer *et al*[20] report 4-5 layers of NiO{100} grown on a surface closely vicinal to Ni{100} using STM, in agreement with our result.

Of course there might be a very real difference in the oxide thickness and orientation on different samples depending upon surface quality and temperature. It is interesting to note here that the value of the sticking probability at its minimum on Ni{100}, after the chemisorption, is relatively high, and so the uptake more closely resembles that at temperatures below the oxide orientation cross-over point, rather than that at higher temperatures where the sticking minimum is more pronounced. It could be that the latency period before oxidation is closely correlated with oxide orientation, whether the kinetically favoured, low temperature, NiO{111} surface, or the thermodynamically favoured, high temperature NiO{100} surface. It seems likely that in our case the oxide is predominantly {111}, in keeping with a four layer passivation model and the relatively low exposure required for the oxidation to start.

Turning to our remaining sample, the {110} surface, oxides grown at room temperature appear to be only poorly ordered[11][24][37]. At slightly higher temperatures, above 313 K, NiO{100} is observed[28]. Also, at intermediate exposures a {100}-like ($9 \infty 4$) pseudo-oxide is often seen[11][24][37]. The NiO{100} orientation appears to supersede NiO{111}, perhaps because there is a good epitaxy of NiO{100} on Ni{110}, with about the same Ni-Ni spacing for each plane. We measure a saturation coverage of 4.1 ML, which is higher than the 3.0 ML reported by Norton *et al*[14] and significantly higher than the 2 ML reported by Rieder or the 2.4 ML reported by Sau and Hudson[35]. Again, there might be a large real variation between samples at room temperature. Finally, we note that our 4.1 ML coverage corresponds to 4.1 layers of the {100} oxide, again in keeping with the four-layer passivation model.

	Oxidation Rate K_iN_0 (L^{-2})	Saturation Coverage θ_{sat} (ML)	Oxidation Onset (ML)	Saturation Sticking s_{rev}
Ni{100}	0.0002	3.6	0.68	0.062
Ni{111}	0.002	3.0	0.45	0.059
Ni{110}	0.0005	4.1	0.8 - 1.2	0.072

Table 2. Data pertaining to the oxidation regime for the three surfaces.

Included in Table 2 are values of K_iN_O, the effective rate constant for oxidation (Equation 2). First we consider the Ni{111} surface. Holloway and Hudson[15] report a rate of 0.009 L^{-2} , while Rieder[11] reports a rate about 3 ∞ slower than this, 0.003 L^{-2}. The value found here is 0.002 L^{-2}, in close agreement with Rieder. The rate is much slower on Ni{100}, according to Holloway and Hudson[6], and to Smeenk[37], it is 0.0003 L^{-2}, and only about 0.0001 L^{-2} acording to Mitchell *et al*[23]. Our result is 0.0002 L^{-2}, in good agreement with all of the previously quoted results. Finally, for the Ni{110} surface, several groups[38][24][28] have reported rates of between 0.006 L^{-2} and 0.007 L^{-2}, or even faster[11], 0.011 L^{-2}. Our result is significantly different, a rate of only 0.0005 L^{-2}. This is in agreement, actually, with a qualitative study by Liu *et al*[39] showing that Ni{110} oxidized more slowly than Ni{111}.

Our Ni{110} result is atypical, with a thicker than expected oxide, and slower oxidation rate. These two parameters are correlated in the fit to the data; the sticking probability at a given exposure can be obtained by lowering the thickness and increasing the rate. This does, however, change the shape of the uptake curve, and our data can not reasonably be fit using the typical literature results. It might be that the island growth model does not hold here, where lateral growth is perhaps faster than the thickening process, so giving a two step oxidation. It might also be that the difference between samples is real, and we have slow oxidation perhaps due to a

very low defect concentration[25] on the crystal sample. We note that our data resembles that obtained[38][28] on {110} surfaces at slightly higher temperatures, near 350 K, where the adlayer is more ordered.

To summarise this section, several important observations have been made using the reflection-detection technique to measure sticking and coverage. Most suprising was the very low chemisorption sticking probability on Ni{111}, with evidence for an adsorption precursor, and the notably low initial sticking probability on Ni{100}. All three oxide films could reasonably be described as having a four layer passivating film. Our technique does not depend upon electron overlayer attenuation factors to obtain absolute coverages. The measured oxide passivation thicknesses, along with calorimetric determination of the molecular lifetime on the oxide, should allow us to extract the electron tunnelling parameter limiting further oxidation from occurring. The sticking probability measurements are useful for understanding oxygen chemisorption and nickel oxidation, but they are also required for the determination of molar adsorption heats, presented in the next section.

3 Adsorption Heat Data

3.1 Introduction

Adsorption heats for gases that are adsorbed in a strictly reversible way can be obtained by isosteric measurements or estimated from thermal desorption data. The adsorption of oxygen on nickel surfaces, however, is irreversible, and so the heat cannot be obtained by such means; the bond is very strong and would require, one expects, about 1500 K for desorption. Upon heating above 600 K, however, chemisorbed oxygen adatoms dissolve into the nickel selvedge[40][38]. A result[4] for equilibrium adsorption isotherms refers to an oxygen-saturated high temperature nickel sample, and a report of high temperature "desorption"[41] is largely accounted for by absorption into the substrate. Calorimetric results[42], described below, exist for polycrystalline films but with poor coverage resolution and a necessarily ill-

defined surface. If large oxygen exposures are used to create a surface oxide film, upon heating it will segregate into chemisorbed atoms and bulk micro-crystallites[20][43].

3.2 Adsorption Heats in the Chemisorption Regime

Table 3 lists the initial heat of adsorption for oxygen on the three Ni surfaces. Each value is actually the average of the first two coverage increments, with a presumed $\sqrt{2}$ improvement in the uncertainty, which is measured as the standard deviation between trials. In order to compare our values to the literature the oxygen-nickel bond strengths are shown also, derived by correcting for the molecular O–O bond dissociation energy[44] of 498 kJ mol^{-1}. Note that this simple approach does not take into account any endothermicity due to distortions of the Ni–Ni bonds, and experiments have shown that the first layer-second layer spacing does change during adsorption[45] according to LEED I(V) analysis and ion scattering[46][33] while the Ni{110} surface reconstructs[47]. Despite this simplification it is striking how well our data agrees with the results of Siegbahn and Wahlgren[48] who performed *ab initio* calculations on clusters ranging in size from Ni_5O to $Ni_{43}O$.

	Ni{100}	Ni{111}	Ni{110}
$q^{cal}_{\theta=0}$	550 ± 10	440 ± 30	475 ± 25
$D^{cal}_{\theta=0}$	520	470	485
$D^{theory}_{\theta=0}$	540	480	—

Table 3. Calorimetric adsorption heats for oxygen on the three low-index crystal planes of Ni ($q^{cal}_{\theta=0}$) in the limit of low coverage, for the process $O_{2(g)}$ + Ni ∅ $2O_{ad}$/Ni and the derived O–Ni bond dissociation energy $D^{cal}_{\theta=0}$ for the process O_{ad}/Ni ∅ $O_{(g)}$. The *ab initio* results $D^{theory}_{\theta=0}$ from ref. [48] are included for comparison.

The values of Siegbahn are perhaps systematically high, though near our experimental uncertainty. We might also mention Egelhoff's trick[49], the equivalent core hole (ECH) approximation, whereby he finds a value for D(O–Ni) very close to

Sieghbahn's at 544 kJ mol^{-1}. This treatment was based on the electronic equivalence of N^+ (with a 1s core hole) with an O atom, applied to XPS data for the c(2 ∞ 2) structure of N/Ni{100}, although his value would presumably include the interaction of the ECH O atom with the N atoms in the 0.5 ML adlayer, and also the effect of a frozen Ni–N bond length for the ECH O atom.

There has been no value calculated for the {110} surface, probably because the initial site is not known, structural determinations being complicated by reconstruction of the open surface during chemisorption. In this case, there must certainly be some energetic price paid in reconstructing the surface that will be included in our adsorption heat. A likely possibility is the formation of Ni–O–Ni–O rows in the form of [001] oriented added-row reconstructions[47] as suggested by STM, with the oxygen atoms occupying (pseudo-four fold hollow) long bridge sites, or displaced slightly to quasi-three fold sites[50], though complicated by the formation of $[1\bar{1}\,0]$ oriented rows at low coverage. However, considering the remarkable degree of agreement between our data and the *ab initio* calculations of Siegbahn[48], our results could perhaps be used as one criterion to predict the correct structure by choosing that which gives best agreement, although a rather large cluster might be required for these more complicated structures.

Theoretical estimations necessarily become more difficult when interadsorbate interactions are included, requiring larger unit cells. Experimentally however, we can extract the adsorption heat as a detailed function of coverage. Figure 6a shows a plot of the differential adsorption heats for oxygen on the three crystal planes of Ni in the chemisorption region as a function of accumulated coverage, while Figure 6b shows the same data recast as the *integral* adsorption heat, extending beyond the end of the chemisorption regime. Our results are the first experimental data available, and show that the oxygen binding energy varies widely with coverage, indicating very strong O–O adatom interactions.

The {100} surface, the most extensively studied, is discussed first. The heat falls dramatically with increasing oxygen coverage: first nearest neighbour positions are

never occupied[10], presumably due to a large repulsion at that separation, 2.5 Å. The heat drop, if it is due to local repulsions, could then be associated with pairwise interactions between third nearest neighbour pairs at 5.0 Å, characteristic of the p(2 ∞ 2) overlayer, or to second nearest neighbour interactions at 3.5 Å characteristic of the c(2 ∞ 2) overlayer. LEED and STM are consistent with an attractive interaction at the p(2 ∞ 2) separation, however, so the heat drop is due to 2nn interactions. Quantifying these pair interaction energies is difficult due to the non-equilibrium disordering present at RT, as evidenced by the sharpening of LEED patterns upon thermal annealing[6][40]. We can estimate a value, however: the *integral* heat of adsorption falls to 400 kJ mol^{-1} at 0.5 ML compared to 550 kJ mol^{-1} for the first 0.05 ML, and ascribing this drop to 2nn interactions, ω_2, in a perfect c(2 ∞ 2) overlayer would imply ω_2 ~ 40 kJ mol^{-1} (although oxide nucleation may well have begun by 0.5 ML).

The large drop in atomic binding energy which we observe, ~ 30% by 0.5 ML, is perhaps suprising, since after some early suggestions to the contrary[51] it was determined that the Ni–O bond is largely unchanged in going from the p(2 ∞ 2) to the c(2 ∞ 2) coverage regimes, as indicated by cluster calculations[52] and as inferred from the equivalence of the Ni–O bond length for the two adlayer structures determined by Pendry *et al*[53][54]. Furthermore, the electronic spectrum is largely unchanged with coverage[55][56]. However, XPS shake-off features[55] do indicate an O–O interaction in the c(2 ∞ 2) adlayer which is not present in the p(2 ∞ 2) structure. It is well known[57] that the Ni–O vibrational frequency shifts from 427 to 318 cm^{-1} in going from p(2 ∞ 2) to c(2 ∞ 2) oxygen coverage. This is most easily ascribed to a change in bond strength of about 45%, of the same order as that implied by our calorimetric data. Of course this shift in vibrational frequencies depends not on the depth of the binding potential, but on its shape[57] and also any coupling to lattice vibrations[58]. However, recent phonon dispersion measurements and lattice dynamical calculations do indicate a substantial repulsion between the adatoms in the c(2 ∞ 2) structure, either by a direct[59] or an indirect[60] interaction, with an O–O

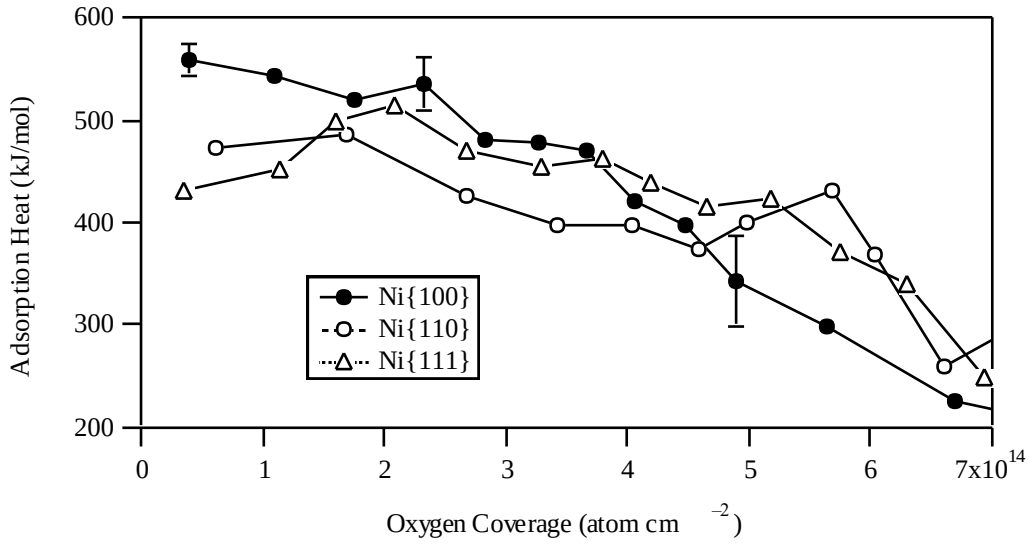

Figure 6a. Oxygen differential heat of adsorption on Ni{100}, {110} and {111} as a function of coverage in the chemisorption regime. 1 Ni ML + 1.61, 1.14 and 1.86 ∞ 10^{15} atom cm^{-2} respectively.

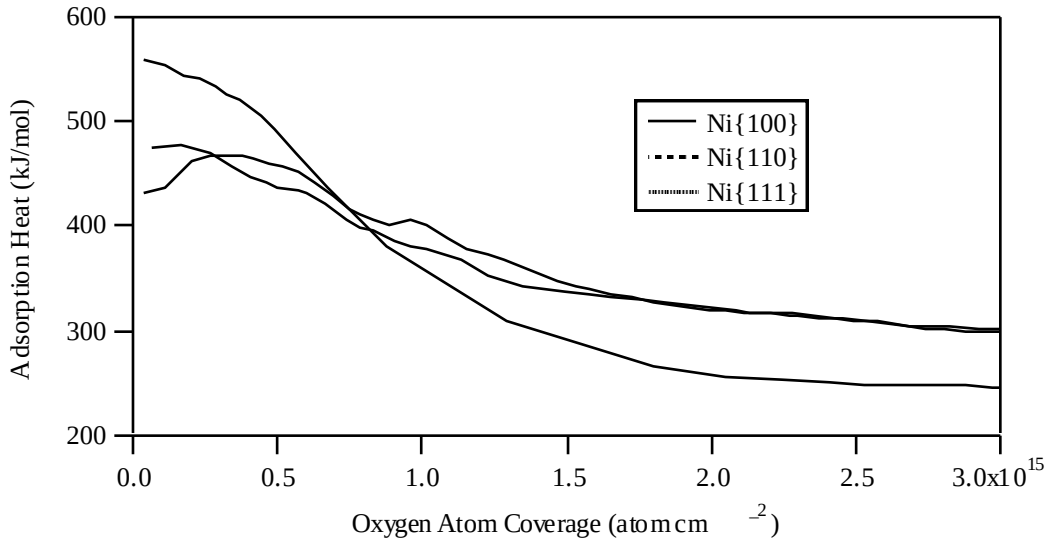

Figure 6b. Integral heats of adsorption for oxygen on Ni{100}, {110} and {111} in the chemisorption and early oxidation regimes.

force constant of ~ 10% of the magnitude of the O–Ni, close to the ratio of our O–O and O–Ni bond strengths at this coverage. Our results should prove invaluable for determining the accuracy of these two sets of force constants. There have also been explicit calculations of the binding energy for O atom pairs at 2nn and 3nn positions.

According to Panas *et al*[61] the binding energy is largely unchanged. However Gallagher and Haydock[62] have pointed out that there may be a substantial amount of closed shell repulsion between atoms at the 2nn separation, and they estimate a repulsive energy ω_2 of about 50 kJ mol^{-1}, which is in good agreement with our data.

We next look at the {110} result. Here the discussion is complicated by uncertainty about the precise binding site and adlayer structure. We might assume the added row model[47] with adatom seperations of 7.5 or 5.0 Å in the [1$\bar{1}$ 0] direction (for the 0.33 ML $(3 \infty 1)$ and 0.5 ML $(2 \infty 1)$ structures respectively) and 3.5 Å in the perpendicular [001] direction. The later value is the same as for c$(2 \infty 2)$ on {100}, but these adatoms, in long bridge sites, are well shielded from one another by the intervening top layer nickel atom. Our data shows that the heat does not drop as quickly as on the {100} surface. The final chemisorption structure suggested in Ref. [47], with pairs of adjacent added rows alternating with one "missing" row to give a 0.67 ML $(3 \infty 1)$ structure, has pairs of oxygen nearest neighbours at only 2.5 Å separation, which would seem improbable given the strong oxygen-oxygen repulsions our data indicate, although the adsorption heat is, at only ~ 150 kJ mol^{-1}, dramatically reduced at coverages of ~ 0.6 ML. In any case adatom mobility at room temperature appears to be limited[38] and the degree of order increases with temperature[14], indicating a non-equilibrium adatom distribution at 300 K.

Finally we consider the {111} surface. The initial heat of adsorption is relatively low, corresponding to adsorption in the shallow three fold hollow sites. The heat actually increases with increasing oxygen exposure at low coverages, the same regime in which the precursor effect is apparent in the adsorption kinetics. According to Roelofs *et al*[63] the adlayer is fairly mobile, and can reach an equilibrium configuration at room temperature, the LEED pattern becoming less intense with increasing temperature. At low coverages they observe islanding of the p$(2 \infty 2)$ adlayer, indicating an attractive potential at the 5.0 Å separation (though at 300 K they see no LEED pattern up to about 0.2 ML). In Gallagher and Haydock's study[62] of O on Ni{100} they estimate an attractive potential of about 1.35 kJ mol^{-1} at this

separation. If each atom had six neighbours, then the integral heat (corrected for double counting of the pair interactions) should increase by about 8 kJ mol^{-1} of O_2. The data (Figure 6b) show an integral heat rise of about 40 kJ mol^{-1}, the same order of magnitude but considerably larger. Of course, that interaction was calculated for the {100} surface, and with a rough confidence limit of a factor of three, and might be substantially different on {111}. If the adlayer is mobile then it should achieve the most thermodyncamically stable arrangement at any given coverage, and so we might expect a monotonically decreasing integral heat. It is possible though that the structure of lowest free energy at low coverages is entropically disordered sufficiently that a noticeable enthalpic gain is achieved when ordering is forced by increasing coverage, as seen to a lesser extent for the {100} surface at higher temperature (see Chapter 7). When the heat *is* observed to fall it may be attributable to repulsive 5nn pair production, leading to the $(\sqrt{3} \times \sqrt{3})$R30° structure, though the 4.3 Å separation is less than for the c(2 × 2) adlayer on Ni{100}. Indeed, by 0.3 ML the integral heat on {111} is hardly less than the initial heat was. The heat fall might also be due to 4nn pairs at domain boundaries.

For each of these surfaces we must also consider whether the heat drops due to the indirect interaction model mentioned by Gallagher and Haydock[62], wherein the oxygen adatom bonding involves a localised nickel surface band with insufficent charge to support higher coverages. In this context we discuss the results of further experiments we have performed in which the nickel surfaces were predosed with potassium, whereupon the surface band electron density has presumably been increased by charge transfer from the alkali metal.

Figure 7 shows the heat of adsorption of oxygen on Ni{100}, {110} and {111} with a high potassium precoverage. It is striking that, by comparison to Figure 6, the results for all three surfaces now approximately coincide. The initial heat for the {100} surface is unaffected, perhaps because the oxygen adatom is very low down in the 4-fold hollow site, so that there is no direct interaction with potassium adatoms. At higher oxygen coverages, however, the potassium is seen to make a very large

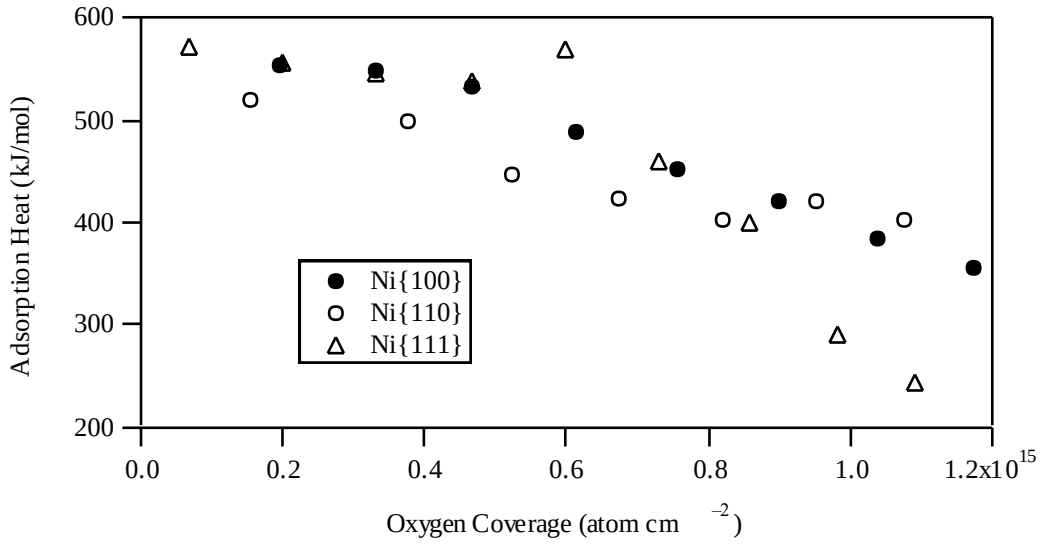

Figure 7. Oxygen adsorption heat as a function of accumulated oxygen coverage on Ni{100}, {110} and {111} surfaces predosed with potassium coverages of 0.2-0.5 ML.

difference to the adsorption heat. This cannot be due just to better ordering of the adlayer, since it persists to above 0.25 ML ($4 \infty 10^{15}$ atom cm^{-2}), after which second nearest neighbour oxygen pairs *must* be forming. It might be due to the exothermic ionisation of the adsorbed potassium screened by the negatively charged oxygen adatoms and strong K^{+}–$O^{\delta-}$ attractions counteracting the O–O repulsions, similar to the effect observed by Al-Sarraf *et al*[64] for CO adsorption. Within the context of this discussion, however, it is natural to consider whether the potassium indirectly donates charge to the oxygen adlayer as the nickel surface layer becomes depleted.

This same model has been used by Kiskinova *et al*[65] to explain the electronic energy loss peaks of oxygen dosed alkylated nickel. A slightly different formulation is to consider that in the environment of the positively charged potassium ions, the molecular orbital levels of the oxgyen adatoms will be depressed relative to the Fermi level, and so may accept more charge from the nickel and/or better match bulk states in energy, giving rise to stronger bonding.

Considering the Ni{111} case, again there is a large effect at high oxygen coverage, the heat maintaining a high, almost constant value. Also, and unlike the {100} case, there is an immediate effect at low coverages. This might indicate a direct O-K

interaction on the more shallow Ni{111} surface. It is interesting that the alkylated surface has such a similar adsorption heat curve to that of {100}, with a nearly equal value for the initial heat of adsorption. Similarly the {110} shows an increased initial oxygen adsorption heat close to that of the {111} and {100}. Is this the heat representative of the complete transfer of 2 e^- worth of charge to the oxygen adatom?

In discussing these effects, work function measurements are directly relevant. The highest resolution data for oxygen on nickel is that of Norton *et al*[14] for the {110} surface. Their work function increase as a function of coverage bends away from a linear rise between 0.1 and 0.2 ML, the coverage at which our calorimetric heat of adsorption starts to drop. The work function perhaps bends similarly at ~ 0.2 ML in the data of Krishnan *et al*[66] for the Ni{100} surface (although the data has more scatter), and it might be that the "kink" seen in Figure 6, where the heat starts to drop more quickly, is the point where less charge per atom is being donated to the oxygen. If such an indirect interaction between oxygen atoms is responsible for the fall in adsorption heat rather than a direct, local interaction, the higher coverage $(3 \infty 1)$ structure[47] suggested for oxygen on Ni{110} (without potassium) in which pairs of adatoms are only 2.5 Å apart becomes tenable.

3.3 Adsorption Heats in the Oxide Film Regime

Next we consider the adsorption heat behaviour beyond chemisorption. Figure 8 shows the calorimetric heat as a function of oxygen coverage up to passivation of the surface oxide. The different surfaces behave somewhat similarly, with the chemisorption heat dropping during chemisorption, then levelling off or rising during oxidation, before dropping to a steady state value. This structure mimics that of the sticking data, or vice-versa, as kinetics will often follow the thermodynamics, unless changes in the activation barrier take precedence. Note that the coverage dependence of the adsorption heat is not seen in the data of Brennan *et al*[42] for calorimetry of oxygen on a polycrystalline evaporated nickel film. (Actually their

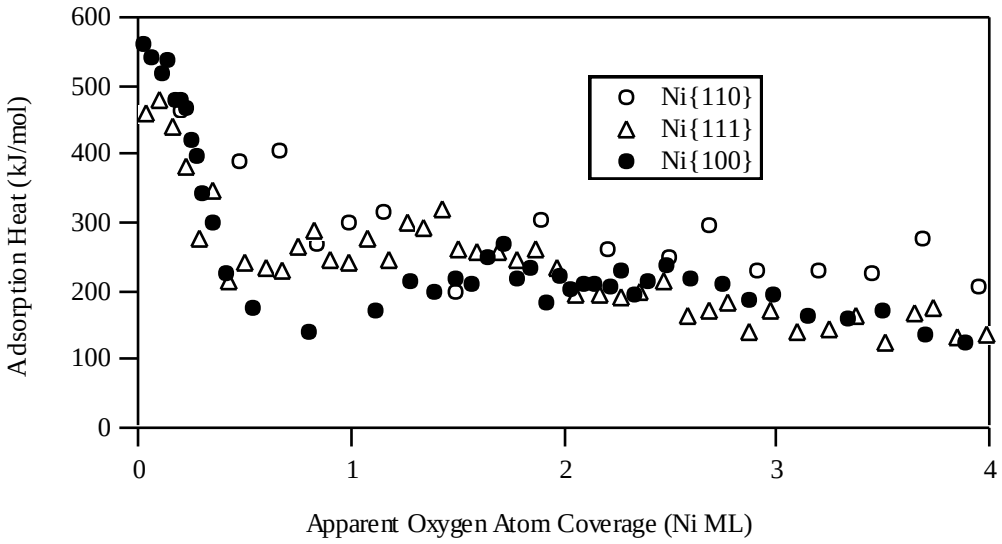

Figure 8. Oxygen differential adsorption heat on Ni{100}, {110} and {111} surfaces at 300 K including the oxidation regime.

data does show a small dip in the heat at about 0.4 ML, which is apparently ignored as an experimental artifact.) As discussed earlier, the uptake kinetics proceed at different rates on the different single crystal surfaces, and so at any given total coverage a polycrystalline sample should have a range of different local coverages, and any coverage dependent structure in the heat curve will tend to be washed out. However, as shown by Horgan and King[67] the coverage-dependent structure of the *sticking probability* curves is still readily apparent on polycrystalline samples. Also, Brennan's integral heat value is some 440 kJ mol^{-1}, which is distinctly higher then we find. It should be kept in mind that his result is "pre-UHV", and may suffer from surface contamination, and genuinely higher binding energies may be achieved at defect sites, which should be abundant in a polycrystalline film.

For the Ni{111} and, especially, the Ni{100} surfaces, the differential adsorption heat passes through a minimum before increasing during oxidation. This may indicate that early in the oxidation there is mixed adsorption, with some low-heat chemisorption still occurring, though it would be expected anyway that the initial oxidation will be less exothermic than later oxidation, as the islands are quite small, and so have a relatively high surface and edge excess free energy. Also, Chakraborty

et al[21] have described how the initial oxide nucleation may require an energetically disfavourable distortion of the nickel surface lattice, which becomes less important with larger nucleii. There has been discussion as to whether or not the pre-nucleation chemisorbed film is thermodynamically stable with respect to the oxide. Experiments by Mitchell et al on Ni{100}[68] and on Ni{110}[69] indicate that the saturated chemisorbed film is at least kinetically stable with respect to oxidation. Although our calorimetric heat of Figure 6a shows a dip before rising during oxidation, this is a *differential* heat. The *integral* heat of the chemisorbed layer, shown in Figure 6b, is always higher than the calorimetric heat at higher coverages, and so the chemisorbed layer is thermodynamically stable (neglecting entropy differences) with respect to the oxide.

It is very interesting to note that the integral heat at the commencement of oxidation is almost identically ~ 380 kJ mol^{-1} on each of the three nickel surfaces. This may be coincidence, especially as the chemisorbed layer might be quite heterogeneous, with oxidation commencing at denser, low-heat sites; or perhaps at 380 kJ mol^{-1} the adlayer is unstable with respect to penetration of the nickel selvedge.

We can point out here how the heat curve also has a contribution from the reversible adsorption of molecular oxygen on the oxide film, a process described in the sticking section. The constant adsorption heat at large exposure (not shown in Figure 8) is that due to the molecular oxygen, and equals about 87 kJ mol^{-1} on each surface. According to Bushby *et al*[22], the population of molecular oxygen on an oxidised nickel surface at room temperature is about 0.013 ML. At steady state the desorption rate is equal to our observed adsorption rate of 0.0012 ML s^{-1}, and if the calorimetric heat is taken as the energy barrier for desorption, the frequency factor for desorption is then $1 \infty 10^{14}$ s^{-1} following the simple analysis of Chapter 3. This is slightly lower than we found for CO desorption from nickel[70], but higher than the surprising low values for CO desorption from Pt{110} and CO from K/Ni{110} (see Chapters 3 and 8 respectively).

Finally, we wish to compare the thermodynamic stability of the different oxide films produced on each nickel surface. The height of the heat bumps in Figure 8 reflects the stability of the film, but also of the chemisorbed layer being consumed during film growth. We must integrate this data over coverage to obtain a number comparable to the bulk heat of formation of the oxide. Also, we must correct for the contribution to the heat due to reversible adsorption occuring on the oxide. This is done using the real film thickness values found in the sticking section, and taking an adsorption heat of 87 kJ mol^{-1} for the excess apparent uptake. The results are shown in Table 4. The values obtained are all much less than the bulk heat of formation of NiO, which is[44] 479 kJ mol^{-1} of O_2. The heat of formation of Ni_2O_3 is closer, 326 kJ mol^{-1} of O_2, but this is probably coincidental. Almost all elemental analyses have indicated a 1:1 ratio of oxygen and nickel in the surface oxide, although Carley *et al*[30] have postulated that the oxide surface is rich in Ni^{3+} defects, bound to O^- adatoms. In any case it is hardly suprising that the surface oxide would have a lower heat of formation than the bulk oxide, considering the long range nature of the electrostatic attractions responsible for its stability and the thinness of the film, and it is known that the surface film irreversibly forms bulk oxide crystallites when heated in vacuum above 525 K. According to Chen *et al*[71] the phonon overtone spectra of the oxide crystallite reveals an oxide bond strength of about 350 kJ mol^{-1}. The oxide heat of formation is a sensitive function of its very large lattice energy, which for an atom in the surface layer could be 100's of kJ mol^{-1} lower than an atom in the bulk, depending on the exact surface structure. For an oxide film which is only four layers thick, this is a significant effect. The lattice energy will also be compromised at the boundary between oxide islands which have grown into one another out of registry, the films grown at room temperature being in general only poorly ordered. In addition there may be considerable lattice strain of both the oxide and nickel substrate at their interface.

	Ni{100}	Ni{110}	Ni{111}
Q_{cal} (kJ mol^{-1})	220	290	320

Table 4. Integral adsorption heats for complete oxide film formation, corrected for reversible adsorption.

Comparing the different samples surfaces, one sees that the Ni{100} surface oxide has the smallest heat of formation. At room temperature this oxide is particularly disordered, containing mixed {111} and {100} faced domains[35], and with only mild heating it irreversibly converts[9] to a more ordered {100} oriented oxide, presumably with a higher heat of formation (though still unstable with respect to the bulk oxide). The Ni{110} surface oxide has a higher heat of formation, which would be expected as its orientation is {100}, which has the lowest surface energy, and also, coincidentally, there is a very good epitaxial match between the NiO{100} oxide and the Ni{110} lattice parameters. More suprising is the high heat of formation of the Ni{111} surface oxide, which has a {111} orientation when grown at room temperature[31], and might be expected to be comparable in energy to that grown on a Ni{100} substrate. The Ni{111} surface oxide also converts to a NiO{100} orientation upon annealing, but the turnover point is ~ 470 K as opposed to ~ 300 K for the Ni{100} surface oxide[9], which may indicate that it has a greater thermodynamic stability (but it might be purely kinetic). The Ni{111} oxide and substrate have the same symmetry, so even with different lattice parameters there might be some super-lattice (7/6) registry. It is likely that the Ni{111} oxide is relatively stable because it is relatively well ordered and defect free[11]. The quality of the oxide appears to be directly correlated with the ease (speed) with which the oxide grew (see the sticking discussion). In the standard model the uptake rate increases with the number of nucleating centres, but in terms of oxide quality might be better related to the speed with which individual islands grow. Indeed, the initial sticking probability does indicate the presence of a molecular precursor on the Ni{111}

chemisorption layer, and this would help an island to grow more quickly, so that a larger ordered domain is formed.

4 Summary

In the chemisorption regime, the initial adsorption heats of oxygen on the three surfaces studied are 550, 475, and 440 kJ (mol O_2)$^{-1}$ for the Ni{100}, {110} and {111} surfaces respectively, although with high coverages of preadsorbed potassium the three surfaces show rather similar heats, of 560, 520, and 570 kJ mol^{-1}. Without alkali metal the heat of adsorption falls rapidly with oxygen coverage on the more open {100} and {110} surfaces, with a second nearest neighbour repulsion of 40 kJ mol^{-1} estimated for the {100} case, assuming that the drop in binding energy is due to localised interactions. Such strong adsorbate interactions were predicted by some theory work[62] but not others[61], but are consistent with lattice dynamical analyses[59][60] of phonon spectra. With coadsorbed potassium the fall in adsorption energy with oxygen coverage was dramatically curtailed, due either to local K-O attractions compensating for O-O repulsions, analogously to previous results we have found before for K/CO coadsorption[64] on Ni{100} (and see Chapter 8 on CO/K/Ni{110}), or perhaps to the provision of additional electronic charge required for strong Ni-O bonding[62]. In fact, this issue is resolved in the following chapter.

The initial sticking probability is less than unity in all three cases: s_0 = 0.63, 0.78 and just 0.23 for Ni{100}, {110} and {111} respectively, in contrast to the assertions of several previous studies[6][7][11][15]. Ni{111} alone clearly exhibited precursor-mediated adsorption kinetics in the oxygen chemisorption regime.

Proceeding to the oxidation regime, the sticking probability data can be reasonably described using a lateral island-growth model, saturating at a thickness of about four NiO layers in each case. The integral adsorption heat (and hence heat of formation, as the reactants are the elements in their standard states) of the thin oxide films varied widely between the three crystal planes, a variation which we attribute

mostly to the degree of order in each case: 220, 290, and 320 kJ mol^{-1} for the {100}, {110} and {111} orientations of the substrate, considerably lower than the heat of formation[72] of bulk NiO of 479 kJ mol^{-1}.

References

[1]N. Al-Sarraf, PhD thesis, University of Cambridge 1993.

[2]K. Otsuka, Q. Liu and A. Morikawa, Inorg. Chim. Acta **118**, L23 (1986).

[3]K.M. Dooley, S.Y. Chen and J.R.H. Ross, J. Catal. **145**, 402 (1994).

[4]H.J. Grabke and H. Viefhaus, Surf. Sci. **112**, L779 (1981).

[5]D. A. King and M. G. Wells, Proc. Royal Soc. **A 339**, 245 (1974).

[6]P. H. Holloway and J. B. Hudson, Surf. Sci. **43**, 123 (1974).

[7]C. R. Brundle and J. Q. Broughton in *The Chemical Physics of Solid Surfaces and Heterogenous Catalysis*, Chapter 3, Volume 3a. Edited by D. A. King and D. P. Woodruff (Elsevier, Amsterdam, 1990).

[8]C. R. Brundle, R. J. Behm and J A. Barker, J. Vac. Sci. Tech. A. **2**, 1038 (1984).

[9]W.-D. Wang, N.J. Wu and P.A. Thiel, J. Chem. Phys. **92** (1990) 2025.

[10]E. Kopatzki and R. J. Behm, Surf. Sci. **245**, 255 (1991).

[11]K. H. Rieder, Appl. of Surf. Sci. **2**, 74 (1978).

[12]A. Winkler, K. D. Rendulic and K. Wendl, Appl. of Surf. Sci. **14**, 209 (1982).

[13]R. Sau and J. B. Hudson, Surf. Sci. **102**, 239 (1981).

[14]P. R . Norton, P. E. Bindner and T. E. Jackman, Surf. Sci. **175**, 313 (1986).

[15]P. H. Holloway and J. B. Hudson, Surf. Sci. **43**, 141 (1974).

[16]A. Winkler and K. D. Rendulic, Surf. Sci. **118**, 19 (1982).

[17]P. Kisliuk, J. Phys. Chem. Solids **3**, 95 (1957); J. Phys. Chem. Solids **5**, 78 (1958).

[18]C. Wang and R. Gomer, Surf. Sci. **84**, 329 (1979).

[19]M. Bowker and D. A. King, Surf. Sci. **94**, 564 (1980).

[20]M. Bäumer, D. Cappus, H. Kuhlenbeck, H. -J. Freund, G. Wilhelmi, A. Brodde and H. Neddermeyer, Surf. Sci. **253**, 116 (1991).

[21]B. Chakraborty, S. Holloway and J. K. Nørskov, Surf. Sci. **152/153**, 660 (1985).

[22]S. J. Bushby, T. D. Pope, B. W. Callen, K. Griffiths and P. R. Norton, Surf. Sci. **256**, 301 (1991).

[23]D. F. Mitchell, P. B. Sewell and M. Cohen, Surf. Sci. **61**, 355 (1976).

[24]R. G. Smeenk, R. M. Tromp, J. F. Van der Veen and F. W. Saris, Surf. Sci. **95**, 156 (1980).

[25]R. Miranda, J. M. Rojo and M. Salmeron, Solid State Commun. **35**, 83 (1980).

[26]T. D. Pope, S. J. Bushby, K. Griffiths and P. R. Norton, Surf. Sci. **258**, 109 (1991).

[28]D. F. Mitchell, P B. Sewell and M. Cohen, Surf. Sci. **69**, 310 (1977).

[29]P. R. Norton, R. L. Tapping and J. W. Goodale, Surf. Sci. **65**, 13 (1977).

[30]A. F. Carley, P. R. Chalker and M. W. Roberts, Proc. R. Soc. Lond. A **399**, 167 (1985).

[31]T. M. Christensen, C. Raoul and J. M. Blakely, Appl. Surf. Sci. **26**, 408 (1986).

[32]C. R. Helms and W. E. Spicer, Phys. Rev. Lett. **32**, 228 (1974).

[33]T. Narusawa, W. M. Gibson and E. Törnqvist, Phys. Rev. Lett. **47**, 417 (1981).

[34]R. B. Hall, C. A. Mims, J. H. Hardenbergh and J. G. Chen, in: Surface Science of Catalysis, Eds. D. J. Dwyer and F. M. Hoffmann, ACS Symp. Ser. 482 (am. Chem. Soc., Washington, 1992) p. 85.

[35]R. S. Saiki, A. P. Kaduwela, M. Sagurton, J. Osterwalder, D. J. Friedman, C. S. Fadley and C. R. Brundle, Surf. Sci. **282**, 33 (1993).

[35]R. Sau and J. B. Hudson, Surf. Sci. **102**, 239 (1981).

[36]W. -D. Wang, N. J. Wu and P. A. Thiel, J. Chem. Phys. **92**, 2025 (1990).

[37]R. G. Smeenk, Thesis, University of Utrecht., 1982.

[37]S. Masuda, M. Nishijima, Y. Sakisaka and M. Onchi, Phys. Rev. B **25**, 863 (1982).

[38]P. H. Holloway and R. A. Outlaw, Surf. Sci. **111**, 300 (1981).

[39]H. -T. Liu, A. F. armitage and D. P. Woodruff, Surf. Sci. **114**, 431 (1982).

[40]D.E. Taylor and R.L. Park, Surf. Sci. **125**, L73 (1983).

[41]J.B. Benziger and R.E. Preston, Surf. Sci. **141**, 567 (1984).

[42]D. Brennan, D.O. Hayward and B.M.W. Trapnell, Proc. Roy. Soc. **A 256**, 81 (1960).

[43]J.G. Chen, M.D. Weisel and R.B. Hall, Surf. Sci. **250**, 159 (1991).

[44]*CRC Handbook of Chemistry and Physics*, 75th edition, eds. D.R. Lide and H.P.R. Frederikse (CRC Press, 1994).

[45]S.R. Chubb, P.M. Marcus, K. Heinz and K. Müller, Phys. Rev. B **41**, 5417 (1990).

[46]P.F.A. Alkemade, S. Deckers, F.H.P.M. Habraken and W.F. Van Der Weg, Surf. Sci. **189/190**, 161 (1987).

[47]F. Besenbacher and I. Stensgaard, and C.J. Barnes in *The Chemical Physics of Solid Surfaces* Vol. 7 Chapters 14 and 13 respectively, eds. D.A. King and D.P. Woodruff (Elsevier, 1994) and references therein.

[48]P.E.M. Siegbahn and U. Wahlgren, Intl. J. of Quantum Chem. **42**, 1149 (1992).

[49]W.F. Egelhoff (Jr.) Phys. Rev. B **29**, 3681 (1984).

[50]B. Voigtländer, S. Lehwald and H. Ibach, Surf. Sci. **225**, 162 (1990).

[51]T.H. Upton and W.A. Goddard III, Phys. Rev. Lett. **46**, 1635 (1981).

[52]C.W. Bauschlicher and P.S. Bagus, Phys. Rev. Lett. **52**, 200 (1984).

[53]W. Oed, H. Lindner, U. Starke, K. Heinz, K. Muller and J.B. Pendry, Surf. Sci. **224**, 179 (1989).

[54]W. Oed, H. Lindner, U. Starke, K. Heinz, K. Muller, D.K. Saldin, P. Deandres andJ.B. Pendry, Surf. Sci. **225**, 242 (1990).

[55]A. Nilsson and N. Mårtensson, Chem. Phys. Lett. **182**, 147 (1991).

[56]K. Jacobi, Solid State Commun. **22**, 17 (1977).

[57]S. Andersson, Solid State Commun. **20**, 229 (1976).

[58]S. Andersson, P.-A. Karlsson and M. Persson, Phys. Rev. Lett. **51**, 2378 (1983).

[59]R. Berndt, J.P. Toennies and Ch. Wöll, Surf. Sci. **244**, 305 (1991).

[60]T.S. Rahman, D.L. Mills, J.E. Black, J.M. Szeftel, S. Lehwald and H. Ibach, Phys. Rev. B **30**, 589 (1984).

[61]I. Panas, P. Siegbahn and U. Wahlgren, J. Chem. Phys. **90**, 6791 (1989).

[62]J.M. Gallagher and R. Haydock, Surf. Sci. **83**, 117 (1979).

[63]L.D. Roelofs, A. R. Kortan, T.L. Einstein and R.L. Park, J. Vac. Sci. Technol. **18**, 492 (1981).

[64]N. Al-Sarraf, J.T. Stuckless and D.A. King, Nature **360**, 6401 (1992).

[65]M. Kiskinova, L. Surnev and G. Bliznakov, Surf. Sci. **104**, 240 (1981).

[66]N.G. Krishnan, Surf. Sci. **57**, 1 (1976).

[67]A.M. Horgan and D.A. King, Surf. Sci. **23**, 259 (1970).

[68]D.F. Mitchell, P.B. Sewell and M. Cohen, Surf. Sci. **61**, 355 (1976).

[69]D.F. Mitchell, P.B. Sewell and M. Cohen, Surf. Sci. **69**, 310 (1977).

[70]J.T. Stuckless, N. Al-Sarraf, C. Wartnaby and D. A. King, J. Chem. Phys. **99**, 2202 (1993).

[71]J.G. Chen, M.D. Wisel and R.B. Hall, Surf. Sci. **250**, 159 (1991).

[72]*Macmillans Chemical and Physical Data*, edited by A.M. James and M.P. Lord (Macmillan Press Ltd, 1992).

Chapter Seven

Pyroelectric Calorimetry: Oxygen on Ni{100}

Abstract

A prototype calorimeter was designed and built relying not on the detection of blackbody radiation but on pyroelectric heat detection, applicable to a far wider range of temperature. The device was sufficiently sensitive to obtain useful results for the system of oxygen adsorption on Ni{100}, at temperatures ranging from 90 to 410 K. The room temperature results obtained were in good agreement with similar data measured using the conventional technique. Analysis and Monte Carlo simulation of the temperature-dependent adsorption heat curves indicates that the large drop in adsorption heat with coverage seen previously at room temperature is consistent with a local second-nearest neighbour adatom-adatom repulsion rather than a long-range electronic effect.

1 Introduction

While the infrared heat detection method employed in the microcalorimeter yielded good-quality signals for room-temperature samples, it was unsuitable for low temperature measurements; the change in radiated power ΔP resulting from some small temperature rise ΔT induced in the crystal is, from the Stefan-Boltzmann law, proportional to $T^3\Delta T$ and so becomes rapidly smaller with decreasing temperature. Compounding this problem, the peak in the spectral distribution of the infrared light moves to higher wavelength with decreasing temperature, and most of the light will eventually occur outside the 2 to 15 μm detection window. Integrating over the portion of the Planck energy distribution curve

$$\rho(\lambda) = \frac{8\pi hc}{\lambda^5}\left(\frac{1}{e^{hc/\lambda kT} - 1}\right)$$

between these wavelengths, only 1.3% of the energy spectrum lies in our detection window at 100 K compared with 56% at 300 K.

Combining these two effects, we would expect signals scaled down by a factor of 2000 in going from 300 to 100 K, although the fall in the metal heat capacity with temperature would partly offset this loss (by a factor of only ~ 3 for nickel). Furthermore as most heat exchange between the crystal and its surroundings occurs by radiation rather than conduction, cooling the sample would require the non-trivial incorporation of extensive radiation shielding occupying most of the crystal's field of view.

An alternative method of heat detection, which did not depend on collecting infrared radiation, was therefore adopted to allow the collection of calorimetric data at cryogenic temperatures[1]. This method relied on the pyroelectric effect, and has been applied already[2][3] to adsorption calorimetry on evaporated films of dysprosium (chosen because of the high adsorption heat expected for oxygen). These are the first pyroelectric adorption calorimetry measurements on single crystal surfaces, however.

2 Pyroelectric Detectors

A thorough explanation of the principles and practice of pyroelectric detectors is given in a review by Porter[4], but a brief description of relevant points is given here.

A pyroelectric material is one which possess an inherent electrical polarisation P, the magnitude of which generally varies with temperature. Most pyroelectrics are also ferroelectric, which means that the direction of their polarisation can be reversed by the application of a suitable electric field, and their polarisation reduces to zero at some temperature known as the Curie temperature by analogy with ferromagnetism. The gradient of the polarisation-temperature curve, dP/dT, is the pyroelectric coefficient p.

2.1 Implementation

A pyroelectric heat detector can be constructed by attaching metal electrodes on opposite faces of a pyroelectric sample, the material being oriented such that its polar axis is perpendicular to the electroded faces. Generally a ferroelectric consists of a large number of separate domains with differing directions of polarisation, so that the net effect over the whole slice is zero. Before use, therefore, these domains must be reoriented by the application of an electric field so that a preferred direction is assumed. This is usually done at some elevated temperature so that a smaller field strength is required.

Even across a suitably poled detector, there will generally be no observable voltage. This is because its internal polarisation is balanced by a surface charge which accumulates via various leakage paths between the two faces. For this reason, the pyroelectric detector can only be used in an ac mode and at a frequency high enough for this electrical leakage to be ineffective; that is, only *changes* in temperature can be detected, which in turn dictates that the sensitivity of the detector will become small as the frequency of the excitation approaches the reciprocal of the thermal time constant of the detector.

The voltage change induced across a pyroelectric detector by some temperature change can either be measured directly using a high impedance amplifier, or be measured as a current if the two electrodes are short-circuited. Usually the former method is employed.

2.2 Noise

The useful sensitivity of a pyroelectric detector is limited by the relative magnitude of the various noise signals which compete with the expected heat signal. The various possible sources of such noise are listed by Porter[4] but the most important source in this particular case was found to be the microphonic pick-up of mechanical vibrations. The strain induced across a pyroelectric wafer gives rise to a voltage because all pyroelectric materials are also piezoelectric, and these small induced

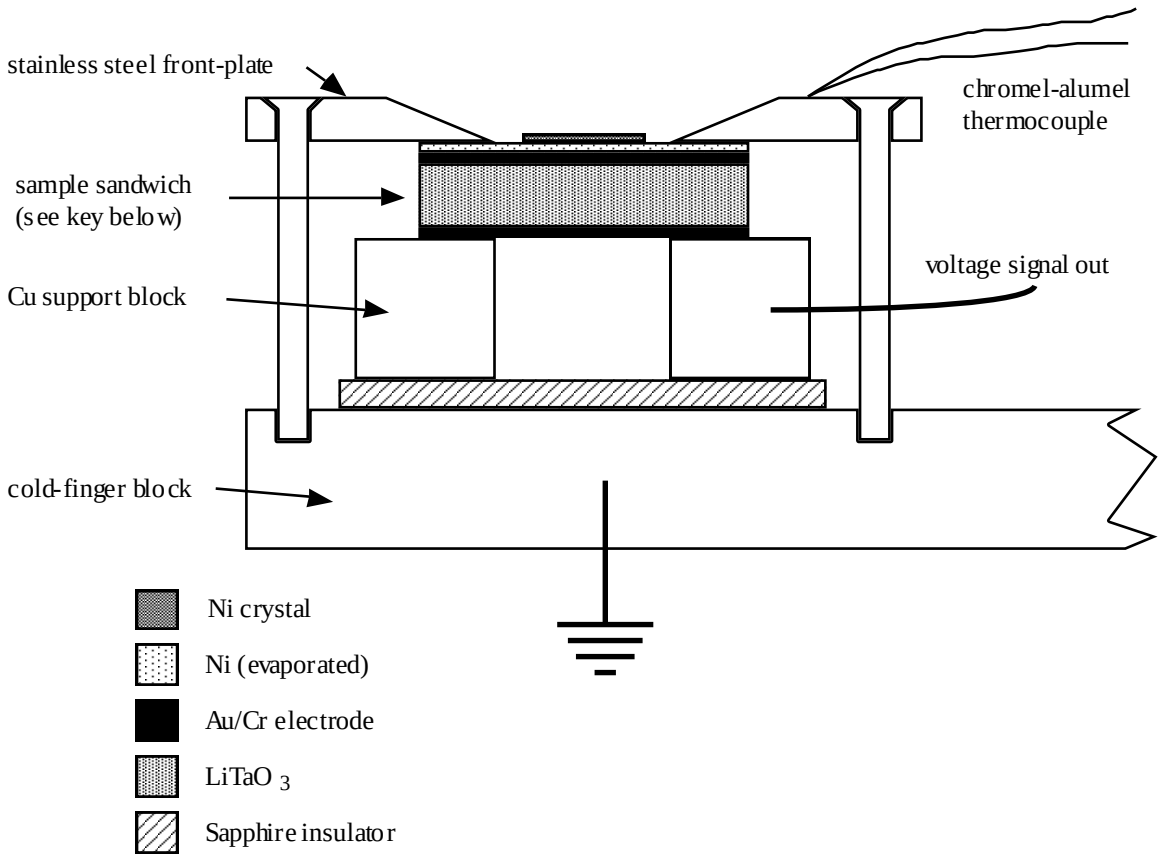

Figure 1. Schematic cross-sectional diagram of pyroelectric detector and sample mount.

voltages will be inextricably superimposed upon those induced by temperature changes. Only if they differ in frequency from the desired signal is filtering possible; in any case the detector must be mechanically designed so as to minimise such vibrations.

3 Design

Of the several pyroelectric materials available $LiTaO_3$ was chosen because of its good sensitivity, UHV compatibilitiy, and high Curie temperature of ~ 900 K, the latter allowing bake-out of the apparatus and annealing of the crystal during cleaning cycles without the polarisation of the material being destroyed. The $LiTaO_3$ crystal wafer, which measured 12 ∞ 14 ∞ 0.3 mm thick (Crystal Technologies Inc.) was supplied with AuCr electrodes evaporated onto its faces. Criteria to meet in the design of the detector were the bonding of the sample metal crystal to the wafer

with good thermal contact, mounting avoiding mechanical vibration, good electrical contacts to the wafer, and some compromise between having a sufficiently poor thermal coupling between the wafer and its support to give a reasonably long thermal time constant (to prevent low-frequency insensitivity) and yet good enough contact to facilitate rapid cooling by conduction.

The Ni crystal was bonded[5] to the $LiTaO_3$ wafer by cold-welding onto an intermediate layer of polycrystalline Ni which in turn was evaporated onto one AuCr electrode. The wafer sandwich was then clamped between a copper block and a stainless steel plate. The copper block was insulated from the rest of the mount by a sheet of sapphire, to maintain a good thermal contact for cooling, and a thin wire was attached to it to measure the voltage of one electrode relative to the other, which was connected to ground via the steel plate and clamping screws. The steel plate had a circular hole to expose the crystal, and the edges of that hole were bevelled in order that the near-grazing ion and electron beams used for sputtering and (especially) Auger respectively could still "see" the crystal. A chromel-alumel thermocouple was spot-welded to the front of the steel plate and the temperature thus measured was assumed to be approximately equal to the crystal temperature. The thin signal wire was connected to a thicker wire which ran along the cold-finger to a BNC feedthrough, to which the specially-designed high impedance amplifier was directly attached. The output of the amplifier was then passed to the analogue-to-digital converter of the experimental microcomputer.

Troublesome low-frequency vibrations from the rotary pumps were much reduced by inserting heavy inertial damping blocks on the tubes connecting them to the chamber. Vibrational noise was nevertheless troublesome and to minimise the effect the sample mount was designed so as not to touch the slot that the usual mount fitted into in the experimental section of the UHV chamber, but instead to hang freely in space supported only by the manipulator.

To obtain the 410 K data, a resistive heater was inserted into the liquid nitrogen cold finger of the manipulator and left running at constant output for some hours to

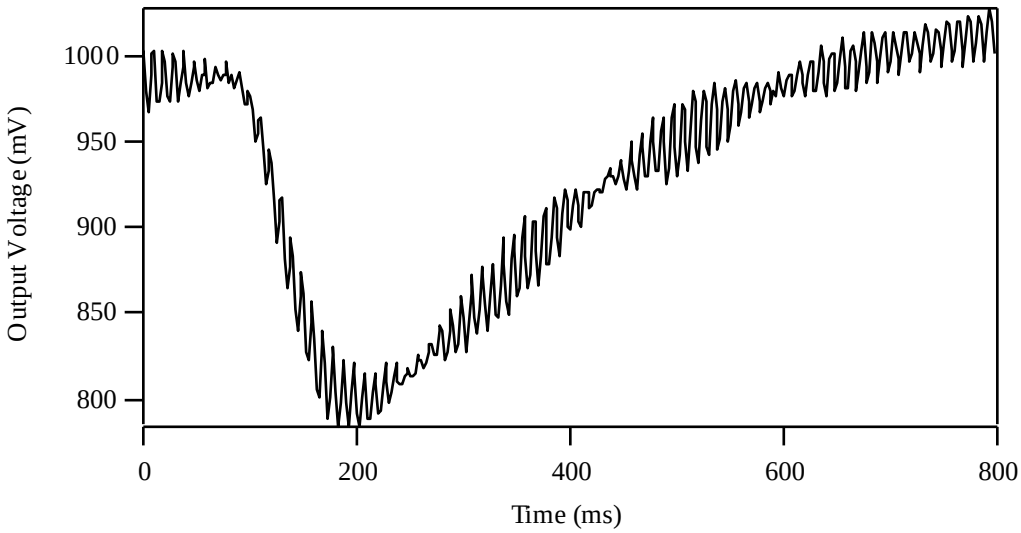

Figure 2. Pyroelectric heat signal from the first 50 ms dose of oxygen on Ni{100} at ~ 100 K.

achieve thermal stability. The crystal was cleaned and annealed using the radiative heater in the normal way without interrupting the conductive heating.

4 Results

The adsorption of oxygen on the pyroelectric detector mounted Ni{100} crystal was studied at three temperatures: 300 K, so that a comparison with the existing (radiation method) results could be made, and then 100 K and 410 K to investigate the behaviour of the adsorption heat and sticking versus coverage curves over the widest temperature range possible.

4.1 Low-Coverage Adsorption Heat Data

Figure 2 shows a signal corresponding to the heat liberated by the first dose of oxygen to adsorb on the surface at 100 K, corresponding to about 0.03 ML. Signal-to-noise varied from day to day with different ambient vibrations present in the building. The signal shown is representative of the best quality data, with only a regular high-frequency (mainly 50 Hz) modulation which is easily removed by smoothing. Nevertheless the signal-to-noise ratio is only ~ 5, an order of magnitude less than comparable signals using the infrared emission technique. With a large

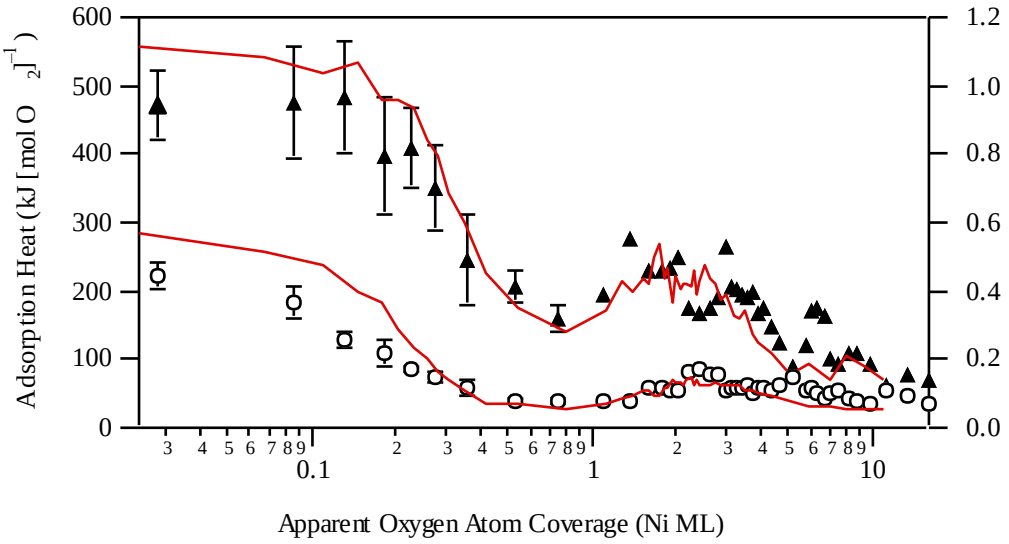

Figure 3. A comparison of data obtained using the pyroelectric and infrared techniques for oxygen on Ni{100} at 300 K. A log scale is used in order that both chemisorption (low-coverage) and oxidation (high-coverage) regimes can be seen in reasonable detail. The filled triangles represent adsorption heat and the empty circles sticking probability for the pyroelectric data, while the solid lines represent the corresponding data obtained using the infrared emission technique.

initial heat of adsorption (~ 500 kJ mol^{-1}) and sticking probability (~ 0.6) combining to give relatively large heat signals of ~ 2 nJ per pulse for this system, useful data could still be extracted despite this limitation. The peak height was found to be directly proportional to the heat dose by firing laser pulses of widely differing intensities at the detector and measuring the response (as for the sensitivity calibration, which was directly analagous to that of the IR emission technique). The sensitivity was calibrated after every experiment and found to be approximately constant over the temperature range covered.

The oxygen adsorption heat and sticking probability as a function of coverage at 300 K are shown in Figure 3, along with corresponding data obtained using the infrared emission technique on a different Ni{100} crystal. Overall the agreement is very good, but at low coverages both the adsorption heat and sticking probability are significantly lower than those obtained in the standard way. This might be attributed to a difference in crystal quality, or in the case of the heat to some systematic error in the laser sensitivity calibration. However, both the heat and

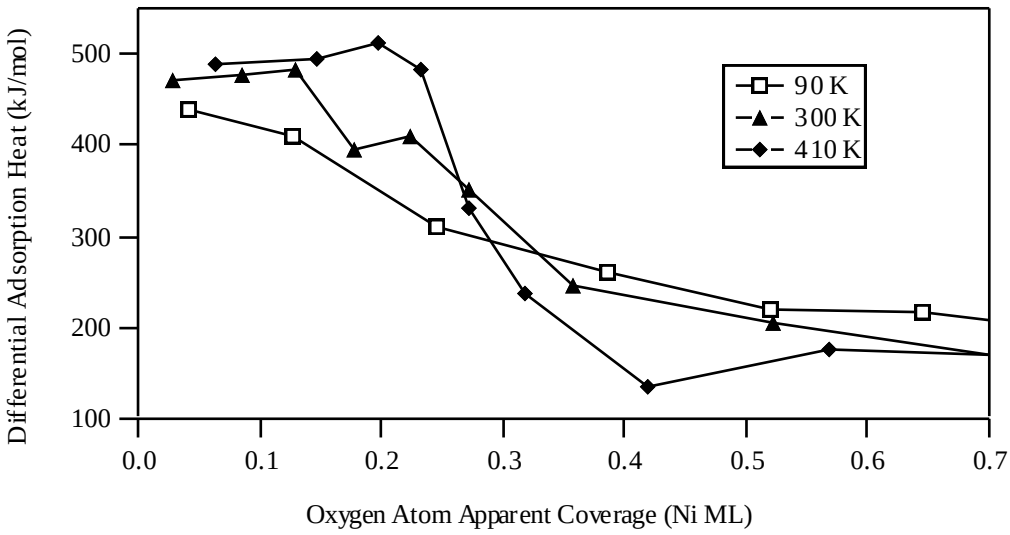

Figure 4. Differential adsorption heat versus coverage for oxygen on nickel at 90, 300 and 410 K in the low-coverage regime.

sticking curves coincide excellently with the existing data if the coverage scale is shifted ~ 0.07 ML to the right, indicating that the probable cause of the discrepancy is some preadsorbed contamination. This was anticipated, as a significant problem with this design of pyroelectric calorimeter was extreme sensitivity to changes in ambient or sample temperature. It was necessary to wait ~ 1 hr after heating or cooling the sample before the temperature was sufficiently stable to allow operation of the calorimeter, compared to ~ 25 min or less using the conventional technique; temperature changes of more than ~ $5 \infty 10^{-3}$ K s^{-1} would saturate the amplifier. This is one of the problems that should be solved by the use of a two-element compensating system. This contamination from background gas in the UHV chamber, as well as the relatively poor signal-to-noise, should be borne in mind when considering the other results shown here.

Figure 4 shows the coverage-dependent adsorption heat for all three temperatures up to one monolayer coverage. Immediate differences are apparent between the three curves: the initial adsorption heat drops as a function of temperature, falling from 490 kJ mol^{-1} at 410 K through 470 kJ mol^{-1} at 300 K to 440 kJ mol^{-1} at 90 K. This trend becomes stronger with increasing coverage: at 0.2 ML the heats are 510, 405,

and 350 kJ mol^{-1} respectively, so that the heat at the highest temperature has *increased* with coverage while at lower temperature it has decreased sharply. However, all three curves become approximately coincident at 0.3 ML and about 300 kJ mol^{-1}, after which the opposite trend is seen: at 0.4 ML, the heats are 160, 240 and 260 kJ mol^{-1} respectively, so the highest heat is now seen for the lower temperature data. After about 0.5 ML, all three curves are approximately coincident once more.

To understand these trends, we must recall from Chapter 6 that the oxygen-oxygen interaction on Ni{100} is weakly attractive at the third-nearest neighbour (3nn) separation, such that the formation of p(2 ∞ 2) islands is preferred up to the ideal saturation coverage for that structure of 0.25 ML, but at the second-nearest neighbour (2nn) distance which becomes occupied in the following c(2 ∞ 2) structure the interaction is strongly repulsive by an estimated ω_2 = 40 kJ mol^{-1}. We might then expect a slight increase in adsorption heat up to the completion of the p(2 ∞ 2) phase at 0.25 ML, followed by a preciptious drop as the c(2 ∞ 2) is filled up to 0.5 ML, and this is exactly what we *do* see at 410 K. The two lower-temperature curves resemble what we might expect at much *higher* temperatures, with entropic disorder introducing 2nn pairs at coverages < 0.25 ML.

For the 90 and 300 K data however, the adlayer is not in thermodynamic equilibrium, but kinetically disordered. At 300 K, the spontaneous hopping frequency for an oxygen adatom is only ~ 1 hr^{-1} as estimated[6] from STM experiments, and so at 90 K we can be sure that the adatoms, assuming dissociative chemisorption occurs at all, have negligible mobility. Furthermore the p(2 ∞ 2) LEED pattern is invisible[7] by eye for 300 K adsorption, but appears at 400 K or higher. We can thus understand the initially lower adsorption heat at lower temperature as being due to kinetic disorder "frozen" into the adlayer, with adatoms forming unfavourable 2nn pairs at low coverages and unable to move to more favourable sites. At coverages greater than 0.25 ML the differential adsorption heat will be lowest for the higher temperature, thermally equilibrated case, as each atom added

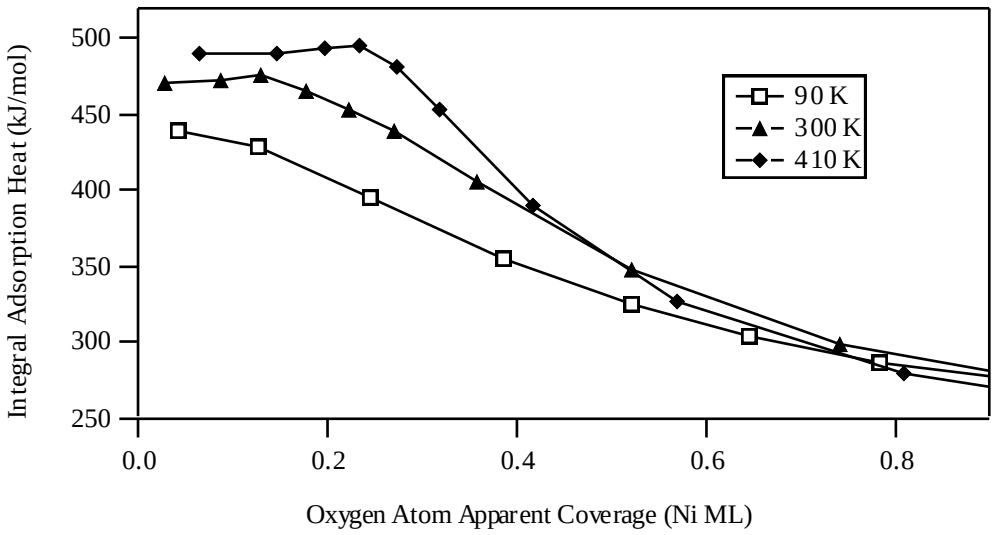

Figure 5. Integral adsorption heat versus coverage for oxygen on nickel at 90, 300 and 410 K in the low-coverage regime.

to the surface will produce close to the ideal four 2nn interactions by filling in the "holes" in the p(2 ∞ 2) structure, while at lower temperatures, some of that energy cost will have already been paid and so the differential adsorption heat will be higher, just as we see in the experimental data.

Figure 5 shows the *integral* rather than differential adsorption heat; that is, at some coverage θ the heat shown is the average amount obtained per mole of oxygen to achieve that total coverage. We still see that at low coverages, the adsorption heat correlates inversely with temperature, but now the *integral* heat at all coverages is greatest for the mobile 410 K adlayer. Just as we would expect, however, the three curves become (and remain) coincident at about 0.5 ML, where the c(2 ∞ 2) structure is completed. We might also note that the heat at 90 K is lower than that at 410 K by about 50 kJ mol^{-1}, close to our estimated value for ω_2, suggesting that each oxygen molecule suffers one 2nn interaction even at the lowest coverages. This is consistent with each molecule dissociating into neighbouring 2nn sites and *remaining* there as an adjacent pair, despite the great energy that we might expect the adatoms to initially possess from dissociation (q.v. Chapter 4, in which "hot" adatoms are discussed in the oxygen/CO reaction on Pt{110}, and also an STM study[8] of oxygen

on Al{111} in which transient mobility following dissociation was indicated). This should be quite clear in STM if sufficient resolution could be obtained. Finally the equality of the integral heats by 0.5 ML indicates that in all cases the same final state is reached by that coverage, implying that even at 90 K, dissociative rather than molecular chemisorption takes place.

We can now resolve an unanswered question of Chapter 6 regarding the oxygen-oxygen interaction on Ni{100}. Using the room-temperature data alone we could not distinguish between the strong repulsive interaction being due to a direct, local repulsion between 2nn pairs, or some nonlocal interaction due to (say) depletion of the charge available for bonding from some surface state. The data with coadsorbed potassium perhaps indicated the latter, in fact. However, the temperature-dependent data here cannot be explained that way; if the effect were "global", then the adsorption heat would drop similarly with coverage whatever the state of order on the surface. Instead we see large differences which correlate perfectly to the expected differences in local configurations, ruling out the long-range explanation at the very least for coverages less than 0.25 ML.

4.2 Monte Carlo Simulation of Heat Data

In order to quantify these 2nn and 3nn interactions a suitable Monte Carlo simulation program was written and applied similar to the classic simulation by Metropolis[9] and applied before to this system by Brundle[10], using a simple pairwise potential truncated to zero for distances greater than the 3nn separation. The model surface was an idealised square "checkerboard" array of identical sites with an infinitely periodic boundary condition. Families of simulated integral heat curves were generated to compare to the 410 K experimental data, which are shown in Figures 6 and 7. These curves were generated using just a 20 ∞ 20 array, but were indistinguishable from curves generated from a 50 ∞ 50 array with much lower coverage resolution. The agreement for such a simple model is remarkably good, especially as the sharp (at 410 K) turning-point at 0.25 ML is bound to be washed out

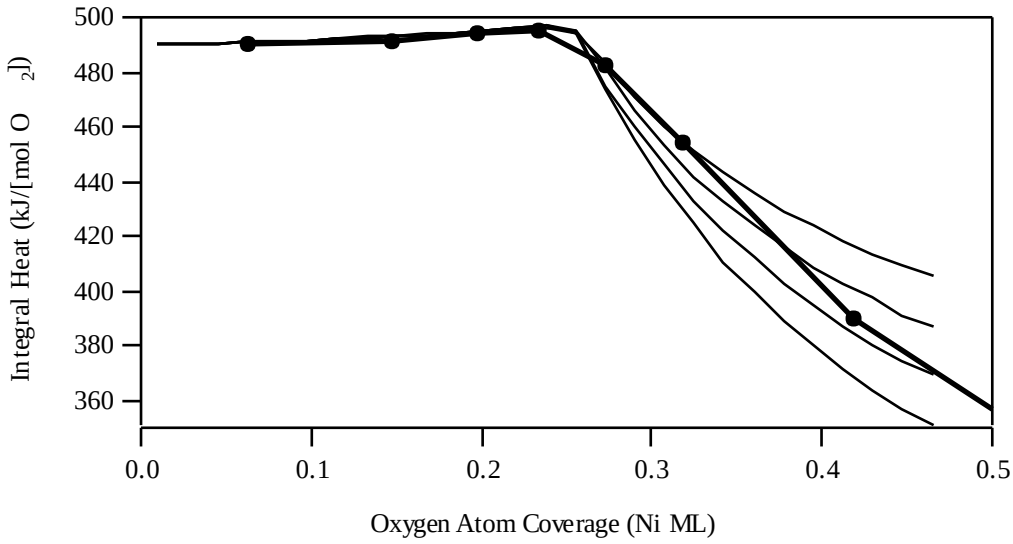

Figure 6. Integral heat of adsorption at 410 K and curves generated by Monte Carlo simulation with ω_2 = 25, 30, 35 and 40 kJ mol^{-1} and ω_3 = –2 kJ mol^{-1}. ΔH_0 = 490 kJ mol^{-1} in each case. (More positive valaues of ω_2 give lower adsorption heats.)

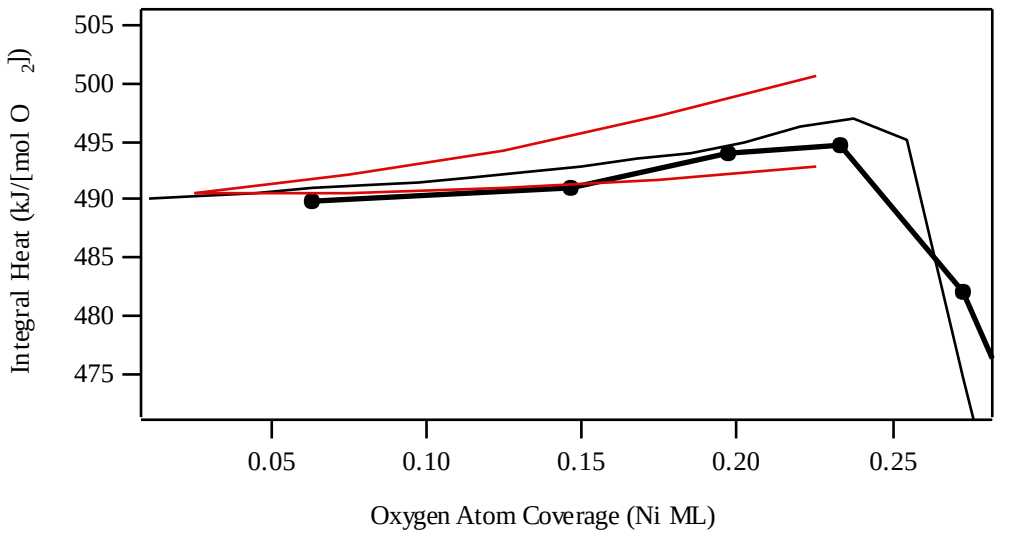

Figure 7. Integral heat of adsorption at 410 K and curves generated by Monte Carlo simulation with ω_2 = +35 kJ mol^{-1} and ω_3 = –3, –2 and –1 kJ mol^{-1}. ΔH_0 = 490 kJ mol^{-1} in each case. (More negative valaues of ω_3 give higher adsorption heats.)

slightly with the finite coverage resolution of the experimental data, and suggests 2nn and 3nn interaction energies of ω_2 = +30 ± 5 kJ mol^{-1} and ω_3 = –1.5 ± 0.5 kJ mol^{-1} respectively.

The lower temperature data could not be reasonably fit in the same way using any combination of interaction parameters, as we would expect considering the equilibrated model and the kinetically disordered adlayer for 300 K and below. The interaction parameters obtained here are in rather good agreement with those estimated by Gallagher and Haydock[11] of a Van der Waals attraction ω_3 ~ – 1.5 kJ mol^{-1} and a closed-shell repulsion ω_2 which they first estimate at +33 kJ mol^{-1} but then scale up to +49 kJ mol^{-1} in order for their potential to show a minimum exactly at the 3nn distance, these figures being quoted to within a confidence factor of 3. The experimental curve is higher than the simulated curve at coverages around 0.3 ML, where the first 2nn pairs should be formed; one explanation for this disagreement is the oversimplification implicit in the model pairwise potential; in reality, adatoms suffering only one or two 2nn interactions may relax away from those near neighbours, giving a higher binding energy than expected.

4.3 Sticking Probability Data

The sticking probability measurements corresponding to the adsorption heat data described are shown in Figures 8 and 9. Sticking data are shown for a temperature also of 180 K, where corresponding heat data are not present due to difficulties in thermally stabilising the sample sufficiently, at this temperature intermediate between liquid nitrogen and ambient, to avoid saturation of the amplifier.

Within the scatter of the data, the sticking curves at 300 and 400 K coincide for low coverages, though the 410 K curve perhaps shows a steeper gradient, which may reflect the unavailability of large arrays of empty sites[10] for dissociation in the more perfectly ordered adlayer. Both show a rapid decline to a coverage of roughly 0.5 ML. The 300 K data then show a slight increase as oxidation proceeds, whereas this is not seen distinctly at 410 K. By contrast, in the 90 K curve the sticking probability remains constant to within experimental error at 0.55 for the first monolayer of adsorption. The 180 K data shows nicely intermediate behaviour,

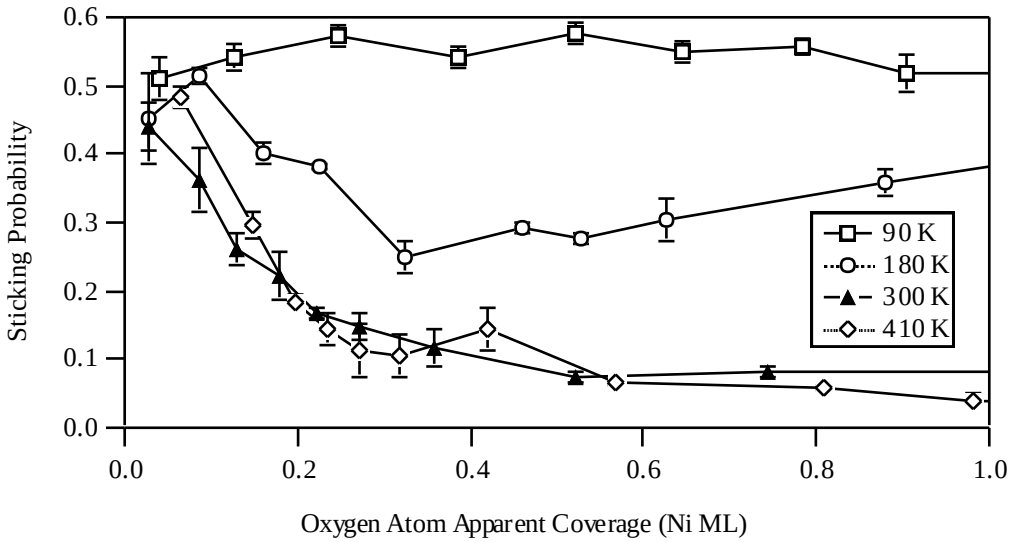

Figure 8. Oxygen sticking probability as a function of coverage for various temperatures on Ni{100} in the chemisorption and early oxidation regions.

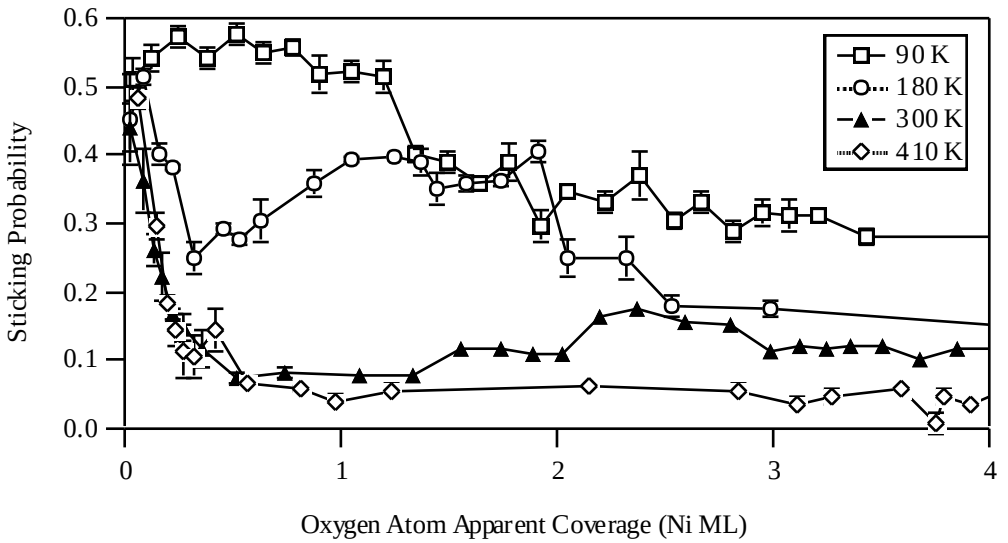

Figure 9. Oxygen sticking probability as a function of coverage for various temperatures on Ni{100} including the oxidation region.

declining slowly to a broad minimum before rising dramatically as oxidation proceeds with little delay.

These results are in qualitative agreement with Holloway and Hudon[12] who find initially coincident sticking curves for 300, 370 and 420 K adsorption but a sticking "bump" corresponding to oxidation which becomes smaller with increasing temperature, reaching maximum of 0.04 at 300 K but less than 0.02 at 420 K. The

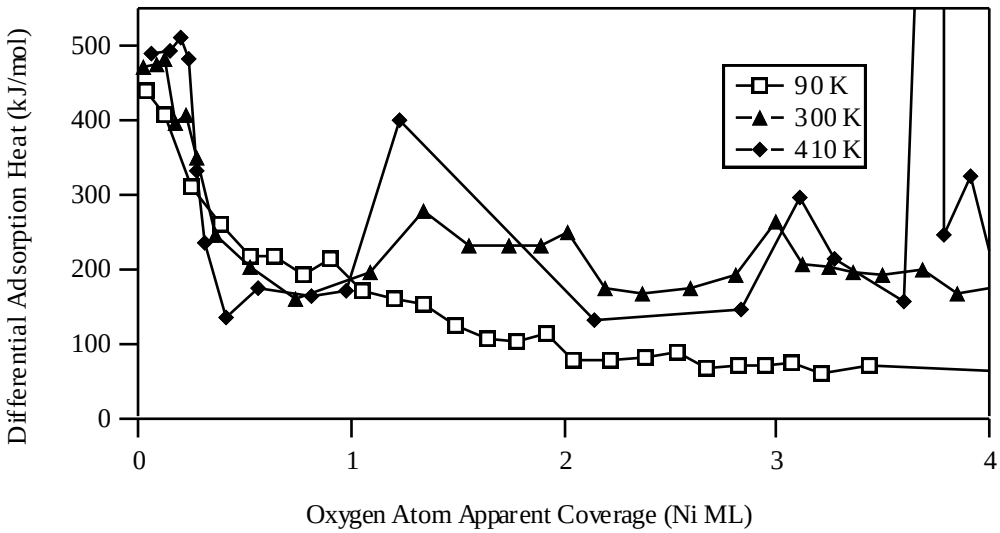

Figure 10. Differential heat of adsorption for oxygen on Ni{100} at 90, 300 and 410 K including the oxidation regime.

latter rise could not be distinguished above our noise level at the time these experiments were performed. At 147 K they report a drop in sticking from unity to 0.5 at a coverage well after the position of the sticking minima present at higher temperatures, then remaining constant in the oxidation region before dropping to meet the other curves at saturation. Scaling their results down to match our initial sticking probability, such behaviour is similar to our 90 K data, whereas at 180 K a low-coverage sticking minimum appears in common with the room temperature data.

The steady-state sticking probability at saturation coverage correlates with temperature, though the explanation is not obvious as the reversibly adsorbed species must be a relatively strongly bound molecule at 410 K and rather weakly bound at 90 K in order to achieve a quasi-equilibrium between adsorption and desorption.

4.4 High-Coverage Adsorption Heat Data

Finally the oxidation regime heat data are presented in Figure 10. It is immediately apparent that the 410 K data are extremely noisy at high coverages; this reflects the

large relative error in the rather small sticking probability in this region, which appears in the denominator of the expression to obtain the molar heat, and also the greater relative noise in the smaller pyroelectric heat signals obtained due also to the small sticking probability (and hence small adsorbed amount of gas per pulse that liberates heat). The data are not obviously different from those of 300 K, however, which in turn are somwhat noisier than those obtained using the IR emission technique (Figure 3 and Chapter 6).

The 90 K data fall to a steady-state value at a notably smaller coverage than the 300 K results, at around 2 ML rather than 4 ML, as does the sticking in Figure 9. No heat "bump" is seen, but rather a continuous decline; if oxidation is occurring at all, then we might imagine that at such low temperatures the gross movement of metal atoms will be strongly hindered kinetically leading to a highly disordered oxide, producing the low heat and early saturation in sticking. Brundle[13] reports that Ni^{2+} is still detected by XPS at 77 K (indicating oxide formation) at coverages as low as in the case of room temperature adsorption but that no ordered LEED pattern is seen, consistent with this picture.

The "reversible" heat of 70 kJ mol^{-1} seen at 90 K is too high for a spontaneously desorbing species at such temperatures, but this heat might be explained by the adsorption of small quantities of oxygen *outside* the sample spot, with the high heat and sticking probability of the chemisorption region. The transient pressure rise due to the molecular beam as measured by the system ion gauge is, at less than 10^{-10} mbar, too low to account for this, but the *local* pressure rise near the sample spot could be considerably greater. This problem never arose with the infrared emission technique as the optics in that case collected light only from the sample spot, whereas this prototype pyroelectric detector was sensitive to a considerably wider area (which represents another area for improvement in future designs). It must be stressed that this error will become signifcant only when the product of the adsorption heat and sticking probability in the dosing spot area is very much smaller than the surface around it. For the higher temperature data, where a large

exposure is required to oxidise the surface layer, the surrounding surface will also receive a sufficient exposure to passivate it to some extent, so negating the error.

5 Conclusions

The prototype pyroelectric calorimeter, despite some limitations in terms of signal-to-noise and thermal stability, yielded data of fundamental interest concerning oxygen chemisorption on Ni{100}, amply demonstrating that this method is viable for single crystal adsorption microcalorimetry. A good agreement was seen between the results obtained with this new detector and those obtained using our "traditional" collection of blackbody radiation from the back of the crystal at room temperature.

The change in the adsorption heat curve with temperature, particularly the behaviour at high temperature where the adlayer is reasonably mobile, indicated that the strong oxygen-oxygen interaction is a *local* effect due to second-nearest neighbour repulsions rather than a long-range electronic effect. The 2nn and 3nn interaction energies were estimated as $\omega_2 = +30 \pm 5$ kJ mol^{-1} and $\omega_3 = -1.5 \pm 0.5$ kJ mol^{-1} respectively by Monte Carlo simulation of the experimental adsorption heat *versus* coverage dependence at 410 K.

Finally the main problems encountered in this prototype—the sensitivity to mechanical vibrations, and to thermal drift—should both be considerably eased by using a compensating system, in which two matched pyroelectric elements arranged in opposition will give a cancellation for any shared vibrations or thermal fluctuations, but a net signal for any heat deposited in only one element. Such work is underway[14] presently and holds great promise for more generally applicable calorimetric studies.

References

[1]St.J. Dixon-Warren, M. Kovar, C.E. Wartnaby and D.A. King, Surf. Sci. **307** 1994) 16.

[2]M. Kovar, L. Dvorak and S. Cerny, Appl. Surf. Sci. **74** (1994) 51.

[3]L. Dvorak, M. Kovar and S. Cerny, Thermochimica Acta **245** (1994) 163.

[4]S.G. Porter, Ferroelectrics **33** (1981) 193.

[5]Crystal mounting performed by Jacques Chevallier of the Institute of Physics and Astronomy, Aarhus University, Denmark.

[6]E. Kopatzki and R.J. Behm, Surf. Sci. **245** (1991) 255.

[7]W.-D. Wang, N.J. Wu and P.A. Thiel, J. Chem. Phys. **92** (1990) 2025.

[8]H. Brune, J. Wintterlin, R.J. Behm and G. Ertl, Phys. Rev. Lett. **68** (1992) 624.

[9]N. Metropolis, A.W. Rosenbluth, M.N. Rosenbluth and A.H. Teller, J. Chem. Phys. **21** (1953) 1087.

[10]C.R. Brundle, J. Behm and J.A. Barker, J. Vac. Sci. Technol. A **2** (1984) 1038.

[11]J.M. Gallagher and R. Haydock, Surf. Sci. **83** (1979) 117.

[12]P.H. Holloway and J.B. Hudson, Surf. Sci. **43** (1974) 123.

[13]C.R. Brundle and J.Q. Broughton in *The Chemical Physics of Solid Surfaces and Heterogenous Catalysis*, Volume 3a, edited by D.A. King and D.P. Woodruff (Elsevier, Amsterdam, 1990).

[14]Y.Y. Yeo and D.A. King, work in progress.

Chapter Eight

CO and Potassium Coadsorption on Ni{110}

1 Abstract

Simultaneously measured sticking probability and heat of adsorption data are presented for the initial reaction of CO with potassium-precovered Ni{110}. Two distinct regimes are observed which correspond with the potassium-affected structure of the surface: for less than 0.35 ML of potassium, the nickel substrate undergoes a missing-row reconstruction, while above this coverage the reconstruction is lifted. On the missing-row structure, the CO sticking probability remains high and the heat of adsorption is increased by only 40 kJ mol^{-1} compared with the clean surface value, to 170 kJ mol^{-1}. On the high potassium coverage structure, the CO sticking probability is dramatically reduced but the CO heat of adsorption is further increased to 250 kJ mol^{-1}.

2 Introduction

2.1 Motivation

Alkali metal additives have been used as promoters in industrial catalysts in the Fischer-Tropsch and Haber processes for some considerable time. Nickel in particular is used to synthesize methane from synthesis gas, a mixure of CO and H_2. Surface science studies of the coadsorption of the reacting species in these reactions must lead to a more thorough understanding of the interactions between them on metal surfaces, and hence to an understanding of their behaviour under catalytic conditions, so holding the hope of designing better catalysts in the future. Calorimetry uniquely provides a direct measure of the energetics of the interactions between the adsorbed species and the substrate under conditions in which no desorption need occur.

2.2 Results from {100} Surface

In similar studies on the Ni{100}[1][2] surface to those presented here, we have obtained the following results. The CO heat of adsorption on a surface predosed with moderate (0.2 ML) potassium coverages was found to increase to 310 kJ mol^{-1}, compared to 125 kJ mol^{-1} on the potassium-free surface. This large increase could be decomposed into three possible contributions: firstly, CO accepts charge from the substrate into the $2\pi^*$ orbital giving a stronger nickel-CO bond, though at the expense of a weakened C–O bond, because proximity to the positively charged potassium ion lowers the molecular orbital energies with respect to the Fermi level. Secondly, CO molecules screen potassium atoms from one another, allowing repolarization of the potassium atoms towards the fully ionized state and strengthening the average Ni-potassium bond; and thirdly, the $CO^{\delta-}$ and K^+ species may cluster together through Coulombic attractions to form islands of a two-dimensional "salt", with a strongly favourable Madelung stabilization energy. The heat of adsorption data were modelled by Christensen and Nørskov[3] utilising a simple scheme in which both CO molecules and K adatoms were represented by polarisable dipoles on a lattice, suggesting that the CO and potassium do indeed cluster together to form such a salt and showed that the heat data observed could be largely explained by electrostatics alone.

The sticking probability of CO on the Ni{100} surface was found to be markedly reduced by potassium deposition. Repulsive K-K interactions combined with a high room-temperature mobility ensure that the alkali metal is initially evenly distributed across the surface. The CO sticking probability *increases* with CO coverage, which can be explained partly because the K atoms are progressively reionised towards smaller K^+ ions, reducing the cross-section to incoming CO, and perhaps more importantly by the possible formation of tightly bound ($CO^{\delta-}$, K^+) islands, creating more free Ni surface available for adsorption.

2.3 Previous Work on {110}

Potassium is now well known to reconstruct the Ni{110} surface to give missing row structures of first (1 ∞ 3) and then (1 ∞ 2) periodicities with increasing K coverage, as determined by LEED[4][5] and ion scattering[6][7]. We might therefore anticipate different behaviour on this substrate to that seen on the less corrugated Ni planes. In their pioneering study Gerlach and Rhodin[8] presented the coverage-dependent desorption energy for sodium on the three low-index planes of Ni. The {110} surface showed markedly different behaviour to the other two surfaces, with an almost constant binding energy for Na up to 0.2 ML, compared with a rapid decrease from the outset on the other two surfaces; assuming analagous behaviour for potassium, we would again expect to find different energetics for CO adsorption on the {110} plane as a function of potassium precoverage.

A detailed study of the CO/K/Ni{110} system was performed by Whitman and Ho[9] using LEED, TDS and HREELS at potassium precoverages of 0.1 and 0.2 ML. They found evidence for potassium-perturbed CO, exhibiting an increased desorption temperature and reduced C–O stretching frequency in a stoichiometric CO:K ratio of approximately 2:1, coexisting at higher CO coverages with unperturbed CO. However, their structural conclusions were based on a bulk-truncated substrate rather than the missing-row reconstructed structures elucidated later. Their TDS results were later modelled by a Monte Carlo simulation[10] to obtain nearest-neighbour K–K and K–CO interaction energies of +0.38 and –0.25 eV respectively, though again not taking account of the reconstruction. Wesner *et al*[11] performed an X-ray photoelectron diffraction (XPD) study which showed that coadsorbed potassium gave rise to tilted CO at an angle of 32°, falling to 27° at a potassium coverage of 0.35 ML with an accompanying abrupt drop in the CO sticking probability. More recently Statiris *et al*[7] reported ion-scattering results suggesting that in the sharp c(2 ∞ 4) structure seen in this system CO molecules are bound to the second layer of Ni atoms on alternate sides of the missing row microfacets and interspersed with potassium atoms, consistent with the XPD results;

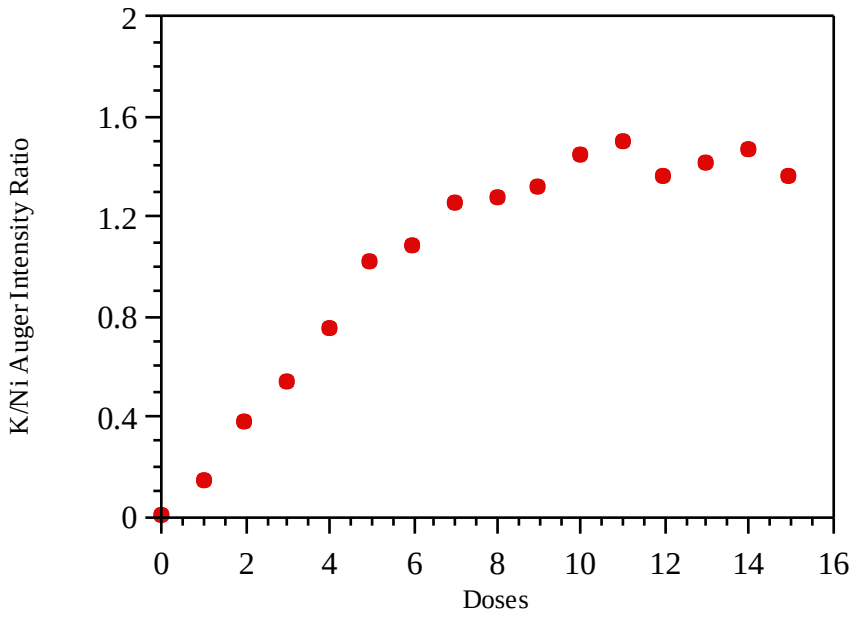

Figure 1. Potassium/nickel Auger intensity ratio as a function of the number of small equal doses, equivalent to coverage assuming constant sticking probability.

this model was previously discussed by Wesner *et al*[11][12]. One would anticipate that such one-dimensional K-CO islands would have a lower stability than the two-dimensional islands possible on the flatter crystal planes, and so a smaller heat of CO adsorption would be expected.

3 Results

3.1 Potassium Dosing and Calibration

Potassium metal was deposited onto the crystal using a commercial SAES getter source placed approximately 5 cm from the sample and normal to its centre. This was thoroughly degassed prior to use such that the chamber pressure increased by no more than $1 \infty 10^{-10}$ mbar during deposition. Following Wesner[11] and Behm[4], the ratio of potassium and nickel Auger peak heights was used as a relative measure of potassium coverage. In a separate experiment to the calorimetry a series of equal doses of potassium were added to the initially clean surface and the K (252 eV)/Ni

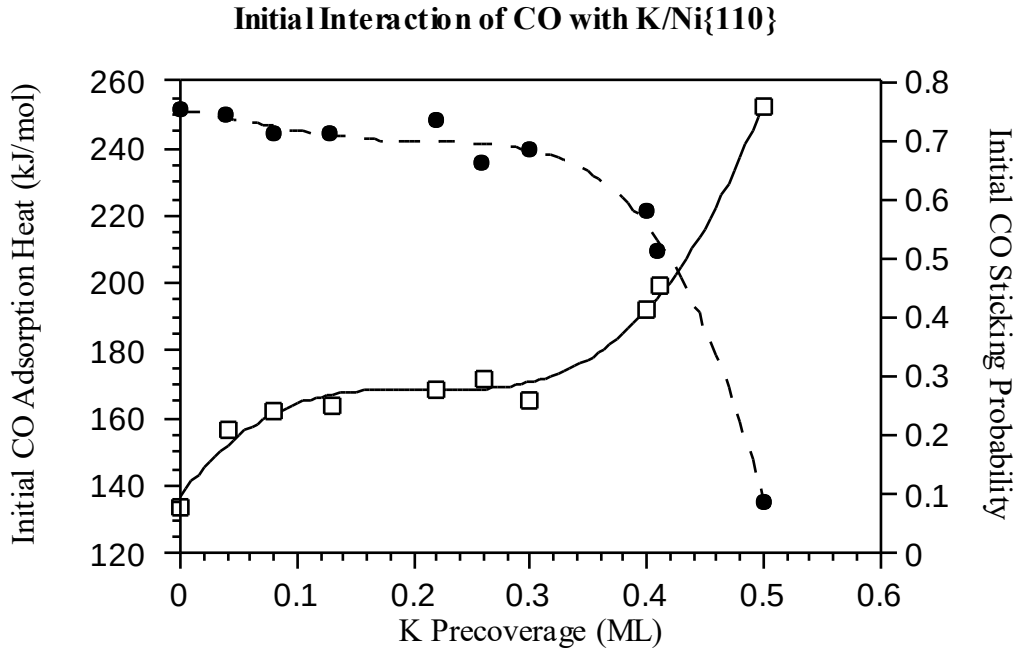

Figure 2. Initial adsorption heat (open squares) and sticking probability (filled circles) for CO on Ni{110} as a function of potassium precoverage.

(848 eV) peak height ratio plotted as a funtion of the number of doses, shown in Figure 1. After each dose the crystal was heated to approximately 450 K in order to prevent multilayer adsorption, and so the curve levels off when monolayer saturation is obtained. The curve is seen to be approximately linear until close to saturation, justifying the use of this ratio as a relative measure of potassium coverage assuming constant sticking probability. From LEED structures the same coverage has been previously estimated[8][4] to be 0.48 or 0.53; here it is assumed to be 0.5 ML.

3.2 Calorimetry Results

Both the heat of adsorption and sticking probability data for CO on the Ni{110} surface showed two distinct behavioural regimes: one above and one below a critical value of approximately 0.4 ML of preadsorbed potassium. The results from those different regimes are discussed separately below.

3.2.1 Low and Moderate Potassium Coverage

From Figure 2 it can be seen that the initial adsorption heat of CO is increased progressively from 133 on the potassium-free surface (taken from Ref. [13]) to first 160 and eventually 200 kJ mol^{-1} for potassium coverages up to 0.4 ML.

The adsorption heat is shown as a function of cumulative CO coverage in Figure 3. The confidence limits shown are discussed in Section 3.2.3 below. It can be seen that for a potassium coverage of 0.04 ML, a possible promoting effect is seen only for the first data point corresponding to just the first 0.05 ML of CO adsorbed, though the magnitude of the effect is similar to that of the expected error. With 0.26 ML of pre-adsorbed potassium however, the CO adsorption heat remains higher than the clean-surface value up to a CO coverage of 0.25 ML. In general, the adsorption heat remains high up to some CO coverage which increases with potassium precoverage, perhaps confirming the presence of some stoichiometric short-range interaction between the two species. At apparent CO coverages in excess of 1 ML, at which point the surface is saturated with CO, the heat of adsorption on the potassium-promoted surface is seen to be *lower* than the clean-surface value. This is discussed below in Section 4.3.

At these potassium coverages the initial sticking probability of CO decreases only slightly with increasing potassium coverage from 0.78 on the potassium-free surface to 0.6 with 0.4 ML potassium, as seen in Figure 2. The CO coverage dependence of the CO sticking probability is shown in Figure 4, and it can be seen that in addition to the reduction in the initial sticking probability, the sticking probability falls more rapidly with CO coverage towards a steady-state value, indicating a reduction in the saturation CO coverage. In the saturation regime, the sticking probability during the 50 ms pulse is progressively reduced from the potassium-free surface value of 0.22 to a value of just 0.03 with 0.4 ML of potassium present.

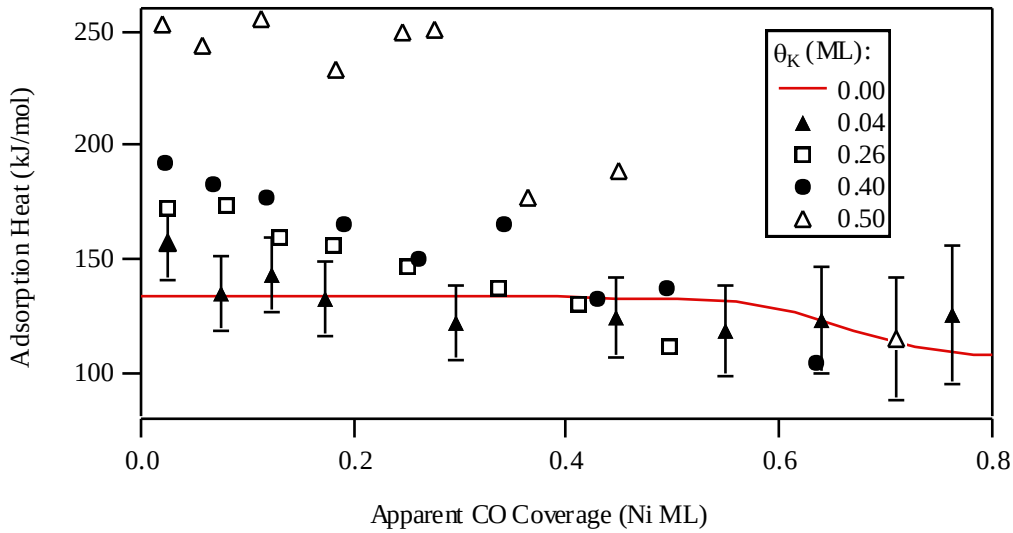

Figure 3. CO adsorption heat as a function of CO coverage for different potassium precoverages.

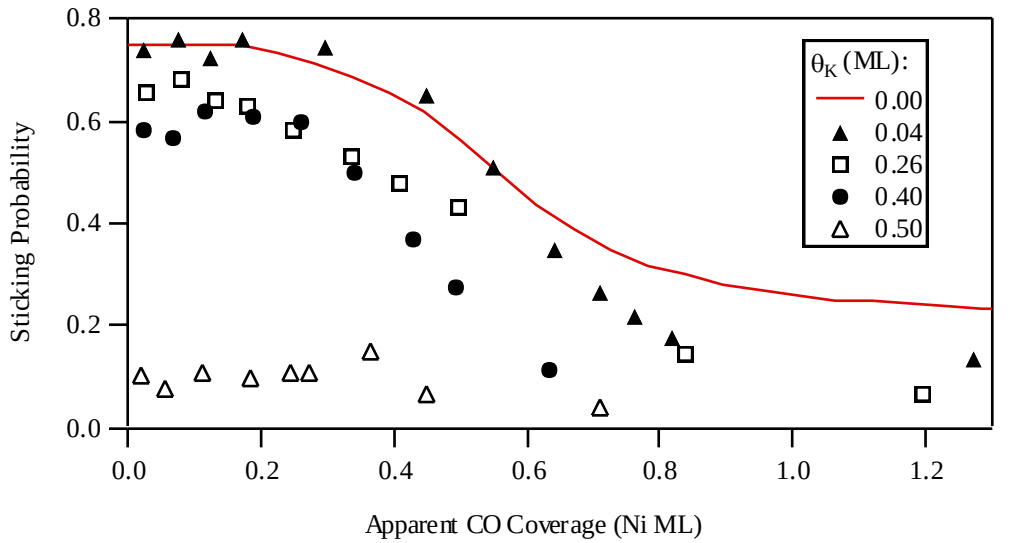

Figure 4. CO sticking probability as a function of CO coverage for different potassium precoverages.

3.2.2 High Potassium Coverage

From Figure 2 it is clear that a dramatic change occurs in both the kinetics and energetics of the CO adsorption process between potassium coverages of 0.4 and 0.5 ML. The CO adsorption heat is further increased from 200 to 250 kJ mol^{-1}, while the

initial sticking probability falls from 0.6 to just under 0.1, in going from 0.4 to 0.5 ML of potassium.

The CO coverage dependent results presented in Figure 4 for 0.5 ML of potassium show that the sticking probability increases slightly with coverage up to 0.35 ML of CO, from 0.1 to 0.15, before dropping abruptly to a value of just 0.03 in the steady-state regime. Within the scatter of the experimental points the CO heat of adsorption remains constant at 250 kJ mol^{-1} during the increase in sticking probability, as seen from Figure 3.

3.2.3 Statistical Error in Heats of Adsorption

To properly interpret features in the results presented it is necessary to be aware of the extent of statistical scatter in the data. Scatter from one heat of adsorption point to the next in a given experiment can be caused by noise in both the infra-red and pressure signals, though the latter is of greater importance. Random experimental errors in the calibrations of calorimeter sensitivity (*via* the laser pulsing technique) and molecular beam strength (using the accumulation tube) will incur proportionate errors between otherwise identical experiments and apply to all data points in one run.

Empirically the point to point scatter in a heat of adsorption curve can be estimated by choosing some portion of the data that appear to be level, and calculating the standard deviation between points. The confidence limits shown on Figure 3 represent two such standard deviations, and become larger with coverage mainly because of the greater error incurred in measuring small sticking probabilities.

4 Discussion

The kinetics and energetics of the adsorption of CO on K-promoted Ni{110} are strongly influenced by the potassium-induced missing row reconstruction of the substrate; this corrugated surface gives rise to quite different behaviour to that seen on the atomically flatter {100} surface until the reconstruction is lifted at high potassium coverages.

4.1 Low and Moderate Potassium Coverage

For the reconstructed surface, the CO sticking probability remains high as substrate atoms are still exposed along the ridges, in contrast to the behaviour seen on the {100} surface where potassium strongly inhibits CO sticking. The heat of adsorption is increased from the unpromoted surface value of 133 kJ mol^{-1} to 170 kJ mol^{-1}, but this is low compared with the 300 kJ mol^{-1} seen on the {100} surface at potassium coverages of only 0.2 ML. This is partly because the formation of close-packed two-dimensional ionic islands of ($CO^{\delta-}$, K^{+}) is prevented by the corrugated nature of the nickel substrate in the missing row configuration, and partly because the potassium atoms are more strongly bound prior to CO adsorption, and so gain less binding energy when the CO is added.

4.2 High Potassium Coverage

As the potassium coverage on the Ni{110} surface exceeds 0.35 ML the missing row reconstruction is lifted, and from Figure 2 it is seen that approximately this coverage marks a turning point in the measured kinetics and energetics of the interaction of CO with the surface. After the lifting of the reconstruction the {110} surface behaves similarly to the {100} plane; the initial heat of CO adsorption is increased to 250 kJ mol^{-1} and the sticking probability drops greatly. The decreased sticking probability suggests that less exposed Ni is seen by the impinging or physisorbed CO molecules, while the increased heat of adsorption can be due to two effects: the strengthening of the potassium-nickel binding due to K-K screening by CO and the possible formation of two-dimensional close-packed islands of ($CO^{\delta-}$, K^{+}) on the flatter surface. Structural studies of the high potassium coverage structure on Ni{110} with and without coadsorbed CO would help to elucidate a precise explanation of the experimental data measured here.

4.3 Steady State Regime

A steady state situation is eventually achieved in the calorimetry experiment at which point the rate of adsorption from the molecular beam pulses is precisely

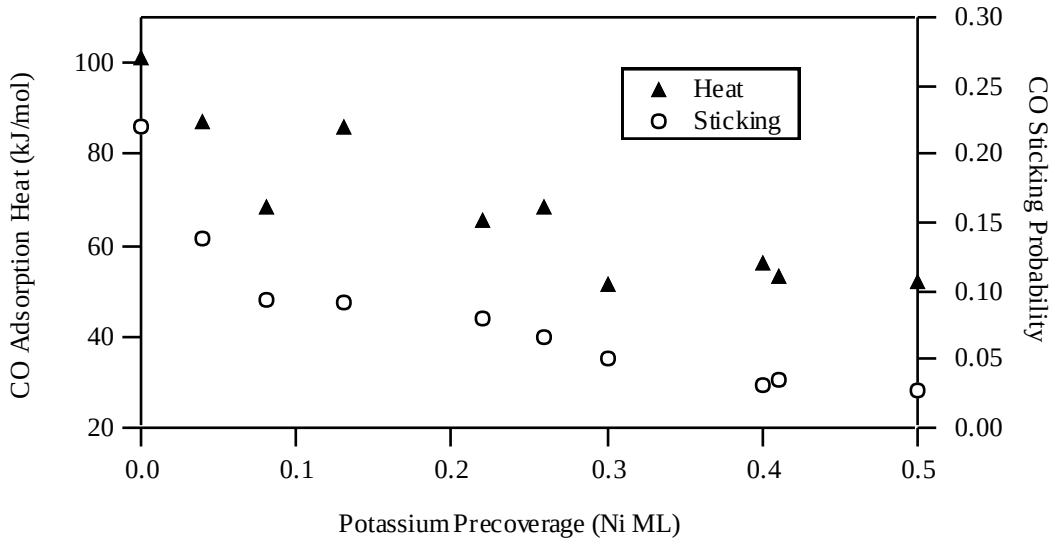

Figure 5. Adsorption heat and sticking probability of CO in the reversible steady-state regime, as a function of potassium precoverage.

matched by the rate of desorption between pulses, as explained in previous chapters. Under these quasi-equilibrium conditions this experiment allows the adsorption (and hence desorption) rates to be determined simultaneously with the adsorption heat, allowing us to determine the Arrhenius pre-exponential factor assuming that this situation approximates to equilibrium (see also Chapter 3). Figure 5 shows the measured steady state sticking probability and adsorption heat for CO as a function of potassium precoverage, obtained by averaging several points at apparent CO coverages of 1.5 ML or more. The adsorption heat is seen to decline progressively from 101 kJ mol^{-1} on the potassium-free surface to just 50 kJ mol^{-1} at the saturation potassium coverage of 0.5 ML, while the sticking probability drops from 0.22 to 0.028 over the same range.

The molecular impingement rate during dosing is known from the calibrated molecular beam flux and known repitition rate and sample surface area. For a typical molecular beam strength of $3 \infty 10^{12}$ molec $pulse^{-1}$, a repitition rate of 2 s and a sample area of $3.3 \infty 10^{-6}$ m^2 the average impingement rate, *I*, is $4.6 \infty 10^{17}$ m^{-2} s^{-1}, equivalent to an ambient pressure of $1.6 \infty 10^{-5}$ Pa. We can attempt to calculate the Arrhenius frequency factor for desorption by equating the calorimetric adsorption

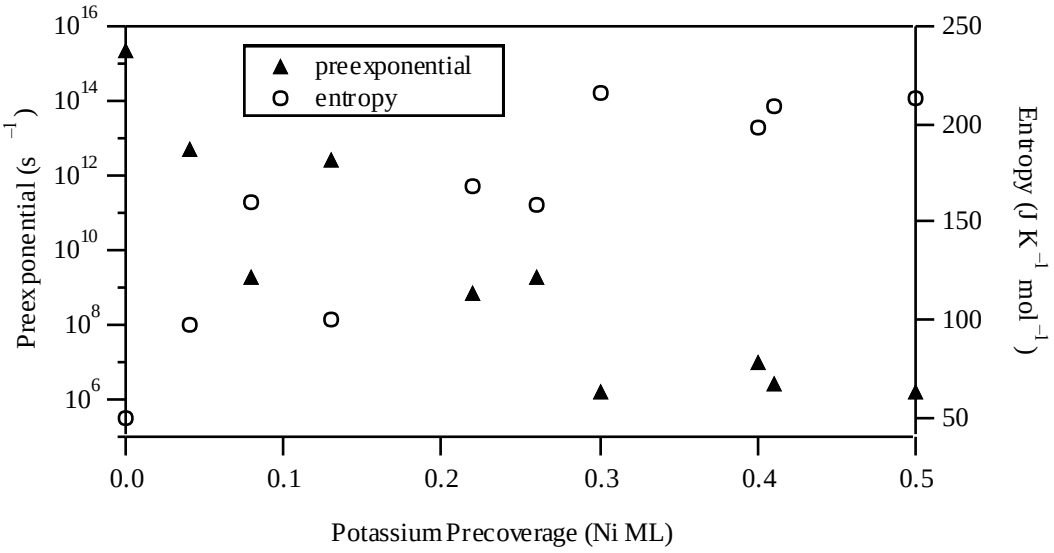

Figure 6. Arrhenius preexponential factor for desorption and adsorbate differential entropy as a function of potassium precoverage, calculated from the steady-state data.

heat with the desorption energy, and the measured adsorption rate with the desorption rate:

$$\nu = \frac{I\sigma}{\theta e^{-q/RT}} \qquad (1)$$

where ν is the frequency factor, σ the sticking probability and θ and q the saturation values of the CO coverage and adsorption heat. Considering the saturation CO coverage, on the clean surface at this effective pressure this is estimated[13] to be 0.95 ML. The order of magnitude of the frequency factor is insensitive to small changes in the saturation coverage used, and here a linear interpolation between 0.95 at zero potassium coverage and 0.5 at saturation, a value estimated from our sticking probability and heat data, is assumed.

From Figure 6 we can see that this calculation for the frequency factor gives a reasonable value of $3 \infty 10^{15}$ s^{-1} for the potassium-free surface but decreases rapidly over many orders of magnitude to just 10^6 to 10^7 s^{-1} for potassium precoverages above 0.3 ML, just before the point at which the missing row reconstruction is lifted. This might in part be explained by a reduction in the coverage θ actually

participating in the adsorption-desorption cycle with increasing potassium coverage, as increasingly more may be "locked" into islands, and it is possible that adsorption might become activated, contributing also to the drop in sticking. However, these effects cannot account for the sheer magnitude of the drop in frequency factor. To help understand this huge change, we shall extract more information from this data. As we have achieved equilibrium, the Gibbs free energy change for adsorption should be zero. Knowing the enthalpy change ΔH (= –q, where q is the calorimetric adsorption heat) we can then infer the entropy change ΔS:

$$\Delta G = \Delta H - T\Delta S = 0 \qquad (2)$$

$$\Delta S = \Delta H / T \qquad (3)$$

The standard entropy of CO (at 1 atm and 298 K) is 198 J K mol^{-1}, and assuming perfect gas behaviour then we can calculate S at our effective average pressure of ~ 10^{-5} Pa for the gaseous starting material:

$$S = S^0 - R \ln (p / p^0) \qquad (4)$$

giving typical values of $S_{(g)}$ = 400 J K mol^{-1}. Knowing this and the entropy change of adsorption, ΔS, we can then quote a value for the differential entropy of the adsorbed species by combining equations (3) and (4):

$$S_{(a)} = S^0 - R \ln (p / p^0) - q / T \qquad (5)$$

which is shown as a function of potassium precoverage, along with the desorption preexponetial constant, in Figure 6. From the graph it is apparent that the two quantities (ln ν and $S_{(a)}$) are in near-perfect anticorrelation, which is a necessary consequence of the algebra above, in which both vary linearly with q (ignoring the much smaller variation of ν with the sticking probability). However, the

interdependence follows also from a statistical mechanical treatment[14] of the desorption rate:

$$\nu = \kappa\, kT/h \exp(\Delta S^{\ddagger} / R) \qquad (6)$$

where κ is some "transmission probability" and $\Delta S^{\ddagger}$ the entropy change in going from the adsorbed to the transition state. If we *assume* that the transition state remains identical with changing potassium coverage, with some fixed entropy $S^{\ddagger}$, which will be lower than that of the gas phase by some fixed amount (and with the degree of freedom along the reaction coordinate factored out), then the entropy change in going from the adsorbed state to the transition state $\Delta S^{\ddagger} = S^{\ddagger} - S_{(a)}$ and so

$$\nu = \kappa\, kT/\, h \exp(\Delta S^{\ddagger} / R) \exp(-S_{(a)} / R) \qquad (7)$$

with all terms constant apart from $S_{(a)}$, which we have seen rises dramatically with potassium precoverage, giving a concomitant exponential drop in the frequency factor. Physically this trend would imply that, with increasing potassium coverage, the species populated in the steady-state regime would change in character from a strongly-bound, well-ordered species to a weakly-bound, gas-like species.

The magnitude of the entropy of the adsorbed state, at up to 220 J K^{-1} mol^{-1}, seems large, but we must bear in mind that it is the *differential* entropy, and so reflects[14] the rate of increase in average entropy with added CO coverage in these conditions. Early work on the adsorption of hydrogen on nickel[15] showed that the differential entropy of the adsorbate (125 J K^{-1} mol^{-1}) can become much larger even than the average entropy for a completely mobile 2D gas of the same coverage (65 J K^{-1} mol^{-1}) as the adlayer becomes mobile at high coverage, although in our case the CO closely associated with potassium probably remains immobile.

Finally we should note that an alternative explanation for a low frequency factor, namely precursor-mediated desorption, was described in Chapter 3 for CO/Pt{110}, and as adsorption here too is precursor-mediated, so the same mechanism may come into play.

5 Conclusions

At high potassium coverages, the adsorption behaviour of CO on Ni{110} is similar to that seen[1][2] on Ni{100}, and can be understood in similar terms: the adsorption heat is increased greatly compared with the potassium-free situation which we attribute to stronger Ni–CO bonding, a repolarisation of the potassium giving stronger Ni–K bonding, and the highly favourable formation of two-dimensional islands of $CO^{\delta-}$ and K^{+} with a large attractive Coulomb energy. Simultaneously the sticking probability is much reduced on the potassium-covered surface. However, before ~ 0.35 ML potassium coverage, the surface is missing-row reconstructed and shows quite different CO adsorption behaviour: only a small amount of CO shows a promoted heat of adsorption, and to only ~ 160 kJ mol^{-1}, though with increasing potassium coverage more CO shows the higher adsorption heat. The sticking probability also remains high, for now Ni is always exposed along the "ridges" of the reconstructed surface, providing adsorption sites for CO even with considerable potassium coverages.

It can thus be seen that changes in the measured sticking probability and adsorption heat of CO on potassium-predosed Ni{110} are largely held in check by the reconstruction induced by the alkali metal. Only at high potassium coverages, where the reconstruction is lifted, are large perturbations to the kinetics and energetics of adsorption seen.

References

[1]N. Al-Sarraf, J.T. Stuckless and D.A. King, Nature **360** (1992) 243.

[2]N. Al-Sarraf, J.T. Stuckless, C.E. Wartnaby and D.A. King, Surf. Sci. **283** (1993) 427.

[3]O.B. Christensen and J.K. Nørskov, Chem. Phys. Lett. **214** (1993) 443.

[4]R.J. Behm, D.K. Flynn, K.D. Jamison, G. Ertl and P.A. Thiel, Phys. Rev. B **36** (1987) 9267.

[5]D.K. Flynn, K.D. Jamison, P.A. Thiel, G. Ertl and R.J. Behm, J. Vac. Sci. Technol. **5** (1987) 794.

[6]Q.T. Jiang, P. Statiris, T. Gustafsson, P.T. Häberle and D.M. Zehner, J. Vac. Sci. Technol. A **10** (1992) 2197.

[7]P. Statiris, P.T. Häberle and T. Gustafsson, Phys. Rev. B **47** (1993) 16513.

[8]R.L. Gerlach and T.N. Rhodin, Surf. Sci. **19** (1970) 403.

[9]L.J. Whitman and W. Ho, J. Chem. Phys. **83** (1985) 4808.

[10]A.R. Cuesta and G. Zgrablich, Surf. Sci. Lett. **275** (1992) L636.

[11]D.A. Wesner, F.P. Coenen and H.P. Bonzel, Phys. Rev. B **39** (1989) 10770.

[12]D.A. Wesner, F.P. Coenen and H.P. Bonzel in *Physics and Chemistry of Alkali Metal Adsorption*, edited by H.P. Bonzel, A.M. Bradshaw and G. Ertl (Elsevier, Amsterdam, 1989).

[14]In *Chemisorption* by D.O. Hayward and B.M.W. Trapnell (2nd ed., Butterworths, London, 1964).

[13]J.T. Stuckless, N. Al-Sarraf, C. Wartnaby and D.A. King, J. Chem. Phys. **99** (1993) 2202.

[15]E. Rideal and F. Sweett, Proc. Roy. Soc. A **257** (1960) 291.